The Cortaderas Zone, Pirquitas Mine, NW Argentina:
An Example of Miocene Epithermal Ag-Zn-Pb-Sn Mineralization in the Andean Tin Belt

by

Evan Thomas Slater

A thesis submitted in partial fulfillment
of the requirements for the degree of
Master of Science (MSc) in Geology

The Faculty of Graduate Studies
Laurentian University
Sudbury, Ontario, Canada

THESIS DEFENCE COMMITTEE/COMITÉ DE SOUTENANCE DE THÈSE
Laurentian Université/Université Laurentienne
Faculty of Graduate Studies/Faculté des études supérieures

Title of Thesis Titre de la thèse	The Cortaderas Zone, Pirquitas Mine, NW Argentina: An Example of Miocene Epithermal Ag-Zn-Pb-Sn Mineralization in the AnActing Dean Tin Belt
Name of Candidate Nom du candidat	Slater, Evan
Degree Diplôme	Master of Science
Department/Program Département/Programme	Geology
Date of Defence Date de la soutenance	September 7, 2016

APPROVED/APPROUVÉ

Thesis Examiners/Examinateurs de thèse:

Dr. Daniel Kontak
(Supervisor/Directeur(trice) de thèse)

Dr. Andy McDonald
(Co-supervisor/Co-directeur(trice) de thèse)

Dr. Michael Schindler
(Committee member/Membre du comité)

Dr. Marcos Zentilli
(External Examiner/Examinateur externe)

Approved for the Faculty of Graduate Studies
Approuvé pour la Faculté des études supérieures
Dr. Shelley Watson
Madame Shelley Watson
Acting Dean, Faculty of Graduate Studies
Doyenne intérimaire, Faculté des études supérieures

ACCESSIBILITY CLAUSE AND PERMISSION TO USE

Abstract

The Pirquitas mine, located in the highly elevated Puna plateau region of NW Argentina hosts Ag-rich polymetallic mineralization that defines the southern limit of the prolific Andean Tin Belt. Approximately 500 m north of its currently active open pit is the Cortaderas Zone which hosts the large Ag-Zn-rich Cortaderas Breccia whose nature and origin were previously unknown. This thesis serves as the first academic study of the Cortaderas Zone that incorporates data pertaining to its geological setting, metal distributions, breccia bodies, mineralogy, ore textures, alteration and fluid inclusions to interpret the origin of its mineralization. The results of this study suggest that the Cortaderas Zone represents the high-level and distal expression of the richly endowed hydrothermal system once present at the Pirquitas mine. Its mineralization formed in a dynamic intermediate-sulfidation epithermal system where ore formation was facilitated by transient fluctuations in confining pressure that were caused by cyclical opening and closing of the system. These insights into the formation of the Cortaderas Zone have implications for understanding the formation and subsequent modification of ores in epithermal settings globally.

Key Words: Pirquitas mine, Andean Tin Belt, Puna plateau, epithermal ore deposits, fluid inclusions, colloform textures, dendritic textures, sulfosalts, hydrothermal breccias

Co-Authorship Statement

This thesis consists of two manuscripts (Chapters 1 and 2) co-authored by the candidate, Dr. Daniel Kontak and Dr. Andrew McDonald. The candidate performed the following tasks: drill core descriptions, sampling, photographing, ore petrography, fluid inclusion petrography and thermobarometry, spatial treatment of whole rock geochemical data in three dimensions, SEM analysis and interpretation, EMPA and LA-ICP-MS data interpretation, and powdered XRD analysis and interpretation. The two thesis supervisors contributed geological ideas related to their respective specialties through conversations with the candidate and through written comments and edits.

Acknowledgments

I am grateful to my supervisors Dr. Daniel Kontak and Dr. Andrew McDonald for providing their support and encouragement throughout the study. I thank the staff of Silver Standard Resources Inc. for providing transport, accommodation and resources while accessing the mine site. The exploration team at the Pirquitas Mine have a vast wealth of geological knowledge that was passed on through discussions with the authors. The exploration team included, but was not limited to Carl Edmunds, Nicholas Larcher, Juan Terrazas, Javier Ceballos, Angus Innes, Carlos Juarez and Jorge Peralta. This work was funded in part by Silver Standard Resources Inc., a Goodman School of Mines graduate scholarship and a Society of Economic Geologists Canada Foundation research grant. The LA-ICP-MS was operated by Dr. Joe Petrus of Laurentian University, the SEM was managed by Dr. William Zhe of Laurentian University's Central Analytical Facility and the EMP was operated by Dr. Kirk. Ross.

Table of Contents

Abstract…….....iii
Co-Authorship Statement……...iv
Acknowledgements…….....iv
Table of Contents……...….v
List of Figures…… ….vii
List of Tables……..…….viii

Chapter 1

Abstract 2
1.0 Introduction 3
2.0 Background 3
2.1 Epithermal Deposits 3
2.2 The Andean Tin Belt 5
2.3 Regional Geology 7
2.4 Mine Geology 11
3.0 Methods 13
3.1 Sample Collection and Preparation 13
3.2 Whole Rock Geochemistry and Geochemical Modelling 14
3.3 Electron Microprobe (EMP) 15
3.3 Powdered X-ray Diffraction (XRD) 15
3.4 Fluid Inclusion Analysis 15
4.0 Results 16
4.1 General Characteristics 16
4.2 Metal Distributions 16
4.3 Breccia Descriptions 21
4.4 Mineralization and Alteration 24
Paragenesis 28
Stage I 28
Stage II 29
Stage III 31
Stage IV 31
Stage V 32
Stage VI 32
Stage VII 32
Stage VIII 33
4.5 Fluid Inclusions 33
5.0 Discussion 38
5.1 Fluid Inclusions 39
5.2 Breccia Bodies 41
5.3 Colloform Textures 43

5.4 Dendritic Textures 43
5.5 Sulfosalts 44
5.6 Gangue Minerals and Alteration 45
5.7 Metal Zoning 46
5.8 Deposit Classification 47
5.9 Genetic Model 48
6.0 Conclusions 50
References 52

Chapter 2

Abstract 59
Introduction 61
Geological Setting 62
Mine Geology and Mineralization 65
Sampling Methodology and Analytical Techniques 69
Results 71
Texture and Composition of Ore Minerals 71
Sphalerite 72
Pyrite 78
Proustite and Galena 82
Jordanite, Galena and Boulangerite 82
Silver-Bearing Tetrahedrite, Miargyrite, Pyrargyrite and Kesterite 83
Pirquitasite-Hocartite and Stannite 84
Canfieldite and Te-bearing Canfieldite 84
Pavonite 84
Sulfosalt Geothermometry 85
Discussion 87
Sulfide-Mineral Chemistry 87
Sphalerite 87
Pyrite 93
Sulfosalt Textures and P-T-X Considerations 95
Implications for the Formation of Ores 103
6.0 Conclusions 105
References 108

List of Figures

Chapter 1

Figure 1: Summary of some important mineral occurrences in the ATB. 6
Figure 2: Geological Setting. 9
Figure 3: Mine Geology. 12
Figure 4: Cross-seciton. 17
Figure 5: Longitudinal Sections 19
Figure 6: Examples of breccias in diamond drill core 20
Figure 7: Petrography of a pebble-dyke breccia. 21
Figure 8: Morphology and petrography of the Potosi Breccia North 23
Figure 9*:* Backscattered electron images of mineralization from several paragenetic stages..... 31
Figure 10: Petrographic and SEM images of gangue and alteration minerals. 27
Figure 11: Paragenetic sequence. 28
Figure 12: Examples of colloform, dendritic and massive textures in drill core and thinsections. 30
Figure 13: High-grade Ag-mineralization. 31
Figure 14: Petrography of fluid inclusions 36
Figure 15: Homogenization temperature and salinity ranges 38
Figure 16*:* Fluid inclusion assemblage data and interpretation 41
Figure 17: Epithermal classification diagram based on sulfidation state. 48
Figure 18: Formational model schematic. 49

Chapter 2

Figure 1: The geological setting of the Pirquitas mine.. 64
Figure 2: Schematic cross-section for the CZ. 67
Figure 3: Paragenetic sequence 69
Figure 4: Example of the colloform texture and rhythmic colour banding 73
Figure 5: Laser ablation-ICPMS traverses and spot analyses 75
Figure 6: Raw LA-ICP-MS count data (counts per second) for spot analyses. 78
Figure 7: Compositional maps (based on LA-ICP-MS data) of a concentrically zoned pyrite grain 80
Figure 8: Raw LA-ICP-MS data for spot analyses 81
Figure 9: Backscattered-electron images of sulfosalt assemblages 81
Figure 10: Backscattered-electron images of galena-jordanite veins 83
Figure 11: Composition of Ag-bearing tetrahedrite 86
Figure 12: Bivariate plots of Ag *vs.* Cu from LA-ICP-MS spot analyses 91
Figure 13: Biavariate plots for LA-ICP-MS data. 93
Figure 14: Reflected-light images of emulsion-like textures 96
Figure 15: Formational model for Ag minerals 100
Figure 16: Equilibrium assemblages in the Ag_2S-Cu_2S-Sb_2S_3 system that is saturated with sphalerite. 101

List of Tables

Chapter 1

Table 1: Descriptions of breccia types. 22
Table 2: Representative chemical analyses for sulfosalts by EMPA. 25
Table 3: Fluid inclusion assemblage microthermometric data summary. 35
Table 4: Ore zone characteristics 55

Chapter 2

Table 1: Electron microprobe analyses of sulfosalts 72
Table 2: Single spot analyses by LA-ICP-MS for sphalerite and pyrite 74
Table 3: Analyses for Ag-bearing tetrahedrite by EMPA. 85

Chapter 1:

Geology and Origin of Multi-staged Epithermal Ag-Zn-Pb-Sn Mineralization in the Cortaderas Zone, Pirquitas Mine, NW Argentina

E.T. Slater, D.J. Kontak, A.M. McDonald

Laurentian University, Department of Earth Sciences and Mineral Exploration Research Centre,

Sudbury ON.

Abstract

The Pirquitas mine located in the Puna plateau of NW Argentina, contains Miocene Ag-Zn-Sn-Pb mineralization at the southern limit of the richly mineralized Andean Tin Belt. Half a kilometer to the North of its currently active open pit is the Cortaderas Zone (CZ) that contains a steeply dipping Ag-Zn-rich breccia vein whose character and origin were unknown. Samples of drill core from the CZ were studied through petrographic, SEM-EDS and EMPA techniques, whole rock geochemistry and fluid inclusion (FI) microthermometry to describe the ore zone and interpret its origin. The CZ was the product of an intermediate-sulfidation epithermal system that formed during a protracted paragenesis that includes a rock preparation/alteration stage, six ore stages, and a waning stage. Its mineralization consists of pyrite, marcasite, sphalerite, arsenopyrite, galena, cassiterite, quartz, dickite ± kaolinite, siderite, hydrous phosphate minerals and various sulfosalts of Ag, Sb, As, Sn, Fe, Zn, Cu, Pb, and Bi that occur with massive, colloform, dendritic and cockade textures. Silver principally occurs in Ag-bearing tetrahedrite, pyrargyrite and miargyrite, however, sulfosalts with Sn, such as minerals of the pirquitasite-hocartite series and canfieldite are also important hosts of Ag. The ore-forming fluids were principally magmatic in origin but became progressively diluted due to mixing with meteoric water. The system episodically dilated and brecciated causing the fluids to flash and boil producing colloform- and dendritic-textured sulfides as well as depositing Ag-bearing minerals. Fluid inclusion data suggests that flashing occurred at temperatures above 320 °C whereas boiling occurred at ~280 °C. Barometric interpretation of FIs indicate the paleo-water table was approximately 250 m above the current erosion surface which is consistent with the mineralization having been of epithermal origin. The deposition of minerals sealed the system enabling the temperatures and pressures to rise resulting in overprinting of the Ag-Sb-rich mineralization by higher temperature Ag-Sn mineralization.

1.0 Introduction

The Pirquitas mine, located ~4,250 m above sea level in the Puna plateau region, Jujuy province, NW Argentina, defines the southern limit of the richly mineralized Andean Tin Belt (ATB). The mine area contains mineralogically diverse and texturally complex Ag-Zn-Sn-Pb mineralization hosted in veins and breccia bodies. The mine area has a long history of mining activity commencing with its initial discovery in 1930 (Rosas & Avila, 2013). Historical records indicate that it had produced ~777,600 kg of Ag, along with ~18,200 t of Sn, prior to modern open pit mining operations by Silver Standard Resources Inc. that began in 2009 (Board et al., 2011). Despite being a long standing mining camp and being the most southern mine in the ATB, there is little published work characterizing its geology and mineralization (e.g., Malvicini, 1978; Idoyaga, 1992; Paar et al., 2001).

In 2010, Silver Standard Resource Inc. discovered the Ag-Zn-rich Cortaderas Breccia in the Cortaderas Zone (CZ) located ~500 m north of the currently active open pit. This article, which serves as the first comprehensive description of the CZ, collectively examines data pertaining to its geological setting, breccia bodies, mineralogy, alteration and fluid inclusions to better define its nature and origin. In addition, grab samples from the Potosi Breccia North, a large breccia body in the open pit are characterized. The result is a paragenesis and fornational model for the newly interpreted ore zone.

2.0 Background

2.1 Epithermal Deposits

Comprehensive reviews of the characteristics of epithermal precious and base metal deposits include Simmons et al. (2005) and Hedenquist et al. (2000). Many deposits in the ATB, particularly those in Bolivia and Argentina, may be classified as a Sn-bearing subclass of

epithermal deposits. Various examples are described in Kelly and Turneaure (1970), Turneaure (1971) and Sillitoe et al. (1975).

Epithermal deposits are hydrothermal mineral deposits that formed at shallow levels in the crust in convergent plate settings. Magmas generated by the melting of the asthenosphere or lower crustal rocks during subduction are emplaced at varying levels in the crust. The heat, fluids, metals and ligands released from these magmatic intrusions are thought to have given rise to mineralization. A diverse range of ore-forming processes have been proposed for epithermal deposits in the ATB including boiling, fluid mixing, depressurization and cooling (Kelly & Turneaure, 1970; Heinrich, 1990; Kontak & Clark, 2002; Wagner, 2009). Fluid mixing is shown to be amongst the most efficient of ways to generate high-grade Sn mineralization (Heinrich, 1990). However, boiling has been documented in many deposits in the ATB and is likely an important process as well (Kelly & Turneaure, 1970). Outside of the ATB, in regions such as Mexico and Peru, boiling has been shown to be an important process in the formation of epithermal deposits that are rich in precious metals (e.g., Moncada et al., 2012; Gamarra-Urrunaga, 2013).

Epithermal deposits are classified as high-, low-, or intermediate-sulfidation types based on the characteristics of the ore-forming fluid(s) (Hedenquist et al., 2000; Simmons et al., 2005). High-sulfidation deposits formed from principally magmatic fluids that were hot, acidic, reduced and moderately saline. Low-sulfidation deposits formed from principally meteoric or ground waters that were relatively cool, had near neutral pH, were oxidized and dilute. Deposits that formed from a combination of meteoric water and magmatic fluids fall in the category of the intermediate-sulfidation.

The sulfidation state of a hydrothermal system is a function of fS_2 and temperature, both of which are influenced by the relative input of magmatic and meteoric fluids as well as reactions

with wall rocks. A more precise definition for sulfidation state is given by Einaudi et al. (2003) where the authors distinguish between very high-, high-, intermediate-, low-, and very low-sulfidation based on sulfidation reactions among minerals in the Cu-Fe-As-S system. These suflidation reactions provide only broad constraints on fS_2 and temperature. Additional reactions between minerals of the enargite-famatinite series and the tennantite-tetrahedrite series as well as reactions between argentite and native silver can be used to further constrain the sulfidation state (e.g., Gamarra-Urrunaga et al., 2013).

2.2 The Andean Tin Belt

The central Andes region hosts precious and base metal occurrences that are arranged in trench-parallel metallogenic belts (Petersen, 1970). The major belts include the Andean Iron Belt with Fe-Cu-Mo-Au mineralization in the Western Cordillera (Sillitoe, 2003), the Andean Copper Belt with Cu-Zn-Ag-Au-Mo mineralization in the Altiplano (Sillitoe & Perello, 2005) and the ATB with Sn-W-Bi-Sb-Ag-Au mineralization in the Eastern Cordillera and Puna plateau (Lehmann et al., 1990). The ATB stretches ~900 km from southern Peru to northern Argentina (Fig. 1). It formed over two metallogenic episodes: a late Triassic to early Jurassic episode and a more richly-mineralized late Oligocene to middle Miocene episode. Both of these metallogenic episodes have been linked to magmatic flare-ups corresponding to discrete collisional periods between the South American Plate and the Nazca Plate (Mlynarczyk & William-Jones, 2005). As a general trend, the northern deposits are Sn- and W-rich (e.g., San Rafael: Kontak & Clark, 2002; Wagner et al., 2009), whereas the southern deposits are Sn- and Ag-rich (e.g., Cerro Rico de Potosi: Turneaure, 1960a,b; Cunningham et al., 1996).

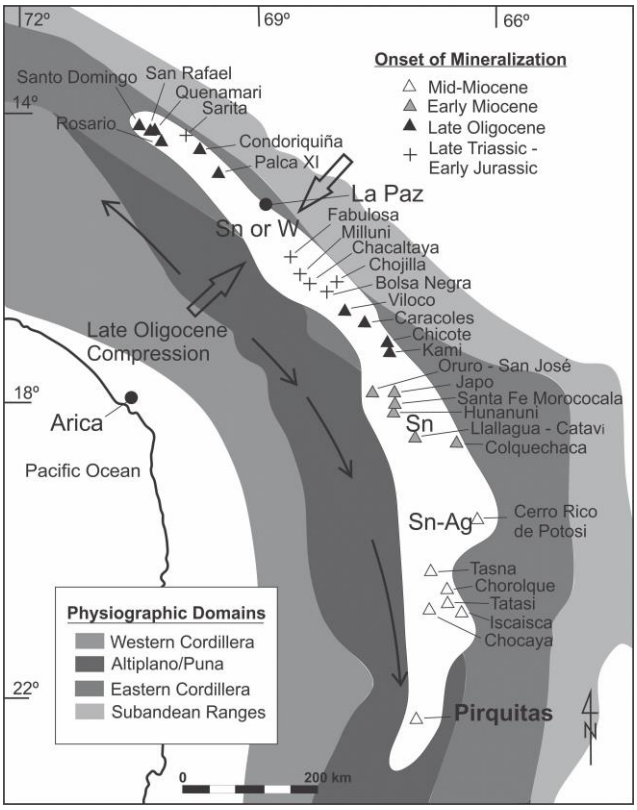

Figure 1: Summary of some important mineral occurrences in the ATB (white region) along with the Andean physiographic domains (grey regions) modified from Mlynarczyk and William-Jones (2005). The Physiographic regions from East to West are the Western Cordillera, Altiplano/Puna, Eastern Cordillera and Subandean Ranges. The curved arrows show the average northward and southward migration of the magmatic front through time. The age of the onset of mineralization at each major occurrence is indicated. The Pirquitas mine is the southernmost primary Sn occurrence in the Andes and thus defines the southern limit of the ATB. From north to south the metal content of these deposits becomes less W-rich and more Ag-rich.

The ATB hosts some of the most valuable hydrothermal ore deposits on Earth, including San Rafael for Sn and Cerro Rico de Potosi for Ag. Despite considerable efforts over the past several decades, controversy remains regarding the origin of this Sn mineralization. For example, it has been suggested that the Sn was inherited from a Sn-rich basement reservoir (Schuiling, 1967; Kittl, 1972; Clark et al., 1976; Schneider & Lehmann, 1977) or was extracted preferentially from a specific zone along a shallowly subducting slab beneath a thickened crust (Sillitoe, 1972; Kay et al., 2001). Regarding the inheritance model, Lehmann et al. (1988) studied the Ordovician-Silurian

sedimentary basement rocks and found no underlying Sn anomaly. Therefore, these authors excluded Sn-inheritance from basement rocks as a likely model for the formation of Sn deposits in the ATB. Subsequent geochemical studies conducted by Lehmann et al. (1990) indicated a systematic Sn enrichment in Bolivian granites which parallels increasing Rb/Sr ratios and thereby suggests that the Sn became enriched in magmas due to fractional crystallization. The authors also demonstrated that the progenitor granites considered to have formed the Sn-rich deposits in the ATB were not derived from a Sn-rich source, but instead formed from magmatic intrusions that have undergone high degrees of fractionation. In all Sn belts globally, Sn and W mineralization is generally associated with ilmenite series granites that developed under low fO_2 conditions during their formation and ascent through the crust (Ishihara, 1981). In the same context, there may be an important interplay between the regional sedimentary host rocks and the formation of Sn deposits, including those developed in the ATB. Reduced carbonaceous sedimentary host rocks may have provided the chemical conditions necessary to keep magmas sufficiently reduced as to allow for the process of fractionation to concentrate Sn (Zentilli et al., 1995).

2.3 Regional Geology

The Pirquitas mine is located in the physiographic region known as the Puna plateau, which is the second largest plateau on Earth after the Tibetan plateau (Allmendinger et al., 1997). The region was uplifted passively and through crustal shortening to elevations averaging 3,700 m above sea level during convergence between the South American Plate and the Nazca Plate (Kay & Mpodozis, 2001). The Puna experienced two stages of deformation in the late Cenozoic (Cladouhos et al., 1994; and Marrett et al., 1994). The first stage, from ~13 to 9 Ma, was characterized by reverse faulting with an average shortening direction of 120 ° ± 20 ° which differs from the average convergence direction of 82 ± 4 ° during that time. The difference is attributed

to reactivation of Cretaceous normal and strike-slip faults (Cladouhos et al., 1994). The second stage, from 9 Ma to recent, was characterized by diverse strain orientations but an average shortening direction of ENE-WSW. The ENE-WSW shortening was accommodated by strike-slip and to a lesser extent, normal faulting as the Puna destabilized during uplift. From ~2 Ma to present, drainage basins developed which incised deep valleys and roughed the Puna's topography (Cladouhos et al., 1994).

The stratigraphic units of northwestern Argentina are described by Turner (1964a, 1964b, 1978, 1982), Coira (1979) and Coira et al., (2004). Ordovician metasedimentary rocks of the Santa Victoria Group dominate the area. The uppermost member of this group is the Acoite Formation, which is the only member of the Santa Victoria Group exposed in the Puna and is form the host rocks for ore at the Pirquitas mine (Fig. 2). Originally described by Harrington (1957), the Acoite Formation was re-interpreted by Bahlburg (1990) to be lithified clastic to volcano-clastic deep-water turbidite sequences deposited on a slope within a back-arc basin. In the Pirquitas mine area, these rocks comprise intercalated layers of quartzites, metapelites and carbonaceous shales. Elsewhere, these metasedimentary rocks are interbedded with sparse metavolcanic rocks, including dacitic tuffs and dacitic to basaltic volcanic flows (Coira et al., 2004). The closure of the back-arc basin during the Late-Ordovician Ocloyic Orogeny, resulted in tight folding, crustal thickening and lower greenschist facies metamorphism (Turner & Mendez, 1979; Bahlburg, 1990).

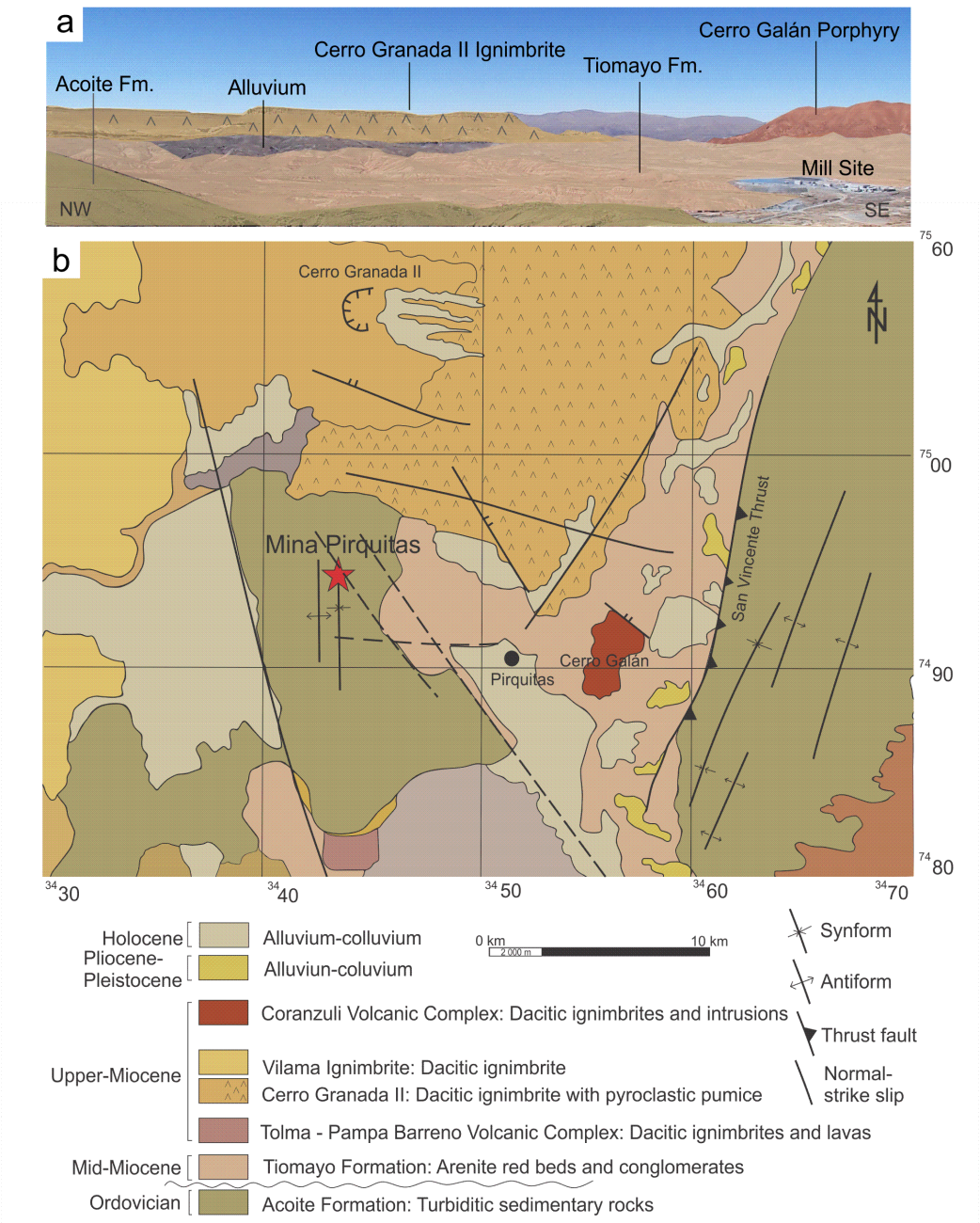

Figure 2: (a) Annotated field photograph from on top of an uplifted block of the Acoite Formation looking northeast. (b) Geological map of the Pirquitas mine area modified from the 1:250,000 map by the Argentinian national mapping program (Programa Nacional de Cartas Geológicas de la República Argentina) produced in 2004 (Coira et al., 2004). The red star indicates the location of the Pirquitas mine.

Foreland basins that formed during the Pehuenche tectonic phase from ~20 to 17 Ma were later filled by the fluvio-lacustrine sediments and intercalated volcanics that compose Tiomayo Formation (Coira et al., 2004). Originally included in the Peña Colorada Formation by Turner

(1978), this formation was redefined by Seggiaro and Aniel (1989) to sit conformably above it. The formation comprises arenites, conglomerates, siltstones, tuffs and ignimbrites and is up to 202 m in total thickness but with great lateral variation. In the mine area, the formation contains a basal conglomerate several tens of meters thick that discordantly overlies rocks of the Acoite Formation and grades upwards into weakly consolidated arenites and mudstones. The strata are weakly deformed with wide homoclines and are locally affected by normal faults and landslides. The age of the Tiomayo Formation is well constrained between ~16 to 10 Ma by K/Ar dating of volcanic material above, below and interbedded with the strata (Coira et al., 2004). For example, the ignimbrites of the Cerro Chuj Chuj lie below the base of the formation and yielded a K/Ar age of 15.7 ± 0.6 Ma. At Pirquitas, a gray ignimbrite intercalated with the reddish lower levels of the Tiomayo Formation yielded a K/Ar age of 14.9 ± 0.5 Ma. At Pan de Azucar, lavas and pyroclastics of the Laguna de Pozuelos volcanic complex in the middle levels of the formation yielded a K/Ar age of 12 ± 2 Ma. Lastly, at Abra Laguna, the ignimbrite of the Orosmayo complex at the top of the formation gave a K/Ar age of 10.3 ± 0.5 Ma (Coira et al., 2004).

The eruption of the Cerro Granada II ignimbrite at 9.8 Ma marked the onset of caldera-type volcanism in the region (Caffe et al., 2008). The unit is a high-K peraluminous dacitic ignimbrite with an areal extent of 630 km^2 centered ~12 km to the North of the mine. Recent estimates of its volume are ~100 km^3, much smaller than ignimbrites that erupted 2 to 6 Ma later (Caffe et al., 2008). The large-volume Vilama Caldera that is centered to the NW of the Pirquitas mine was active at 8.4 Ma and is estimated to have released ~1800 to 1200 km^3 of ejecta material (Soler et al., 2007). The Coranzuli Volcanic Complex, centered to the SE of the Pirquitas mine includes the Coranzuli Caldera that was active ~6.6 Ma and the Cerro Galán intrusion (Caffe et al., 2002).

2.4 Mine Geology

Mineralization at the Pirquitas mine is hosted in an uplifted and exhumed block of the Acoite Formation (Fig 2.). Its veins and breccia bodies are steeply dipping and discordant to the folded strata, although they locally have been focussed along bedding contacts, fold hinges, and Ordovician orogenic quartz veins. There is an apparent association between the location of fold hinges and mineralization, as can be seen in a map of the mineralization (Fig. 3). Several N-S trending faults are present in the open pit that are traced at least as far north as the CZ. A prominent fault is the Mirador Fault that occurs parallel to bedding within the limb of an anticline and has exploited graphitic layers. The age of mineralization has not been determined, however, it is observed to cut the basal remnants of the overlying Tiomayo Formation. Therefore, the mineralization must be younger than ~16 Ma, which, as described above, is the maximum age of the formation.

The most significant mineralized zones in the mine area are the San Miguel Zone, the Oploca Zone, the CZ, and the Huanuni Zone (Fig. 3). The San Miguel Zone, located in the core of the open pit, contains narrow sheeted veins and several large veins. The large veins include the Potosi vein that has a known strike length of ~500 m and maximum thickness of 3 m as well as the Chocaya, Crucero, and Blanca veins that have strike lengths of 50 to 150 m and are narrower. South of the San Miguel Zone are the two Oploca veins that are narrow but contain very high precious metal concentrations. Approximately 500 m north of the San Miguel Zone is the CZ that contains a sulfide-rich breccia vein up to 20 m wide that grades outwards into a broad zone of crackle breccias and smaller apophyses. To the NW of the CZ is the Huanuni Zone which contains several parallel and steeply dipping breccia veins with sulfide-rich mineralization.

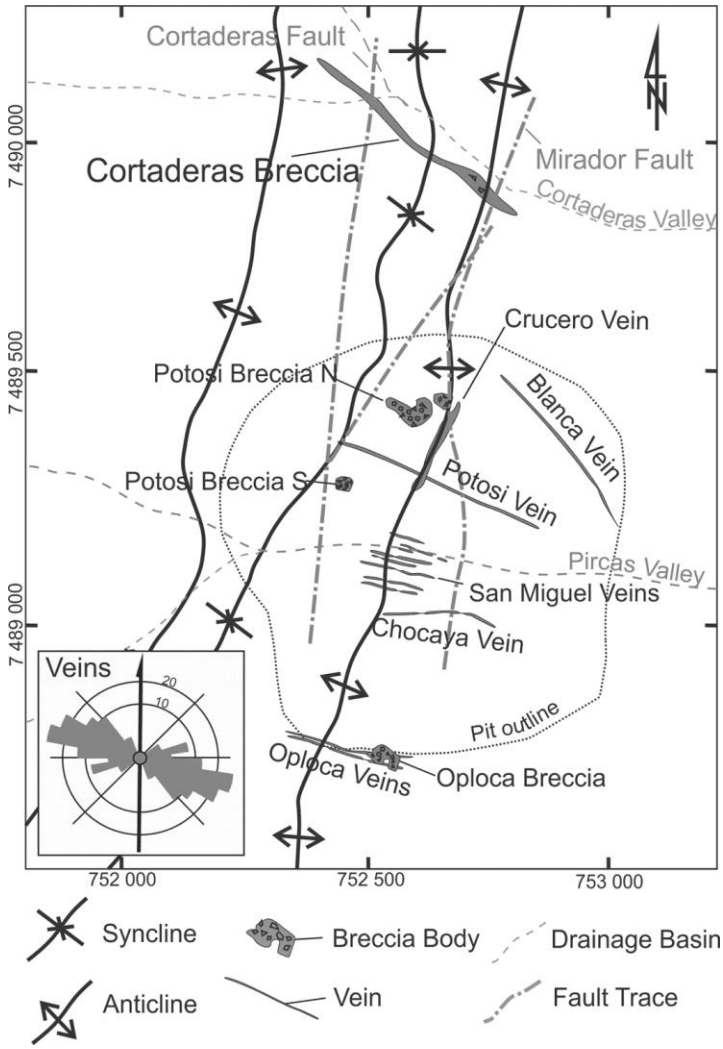

Figure 3: Map of some major veins and breccia bodies within the mine area. The dotted black line outlines the shape of the open pit as of 2013. The sheeted San Miguel veins form the center of the open pit area. Other large veins include Chocaya, Blanca, Potosi, the Oplocas, and Crucero. Important breccia bodies include the Potosi North, Potosi South and Oploca. Almost directly north of the pit center is the Cortaderas Breccia that has both characteristics of a vein and of a breccia. A rose diagram depicting vein orientations is included and was modified from Idoyaga (1992).

Veins at the Pirquitas mine are described by Malvicini (1978) who divided them into two groups: 1) Potosi, Blanca, Colquechaca, Oploca, Llallagua, Chicharron and Colquiri, and 2) San Pedro, Chocaya and San Miguel. The first group is characterized by early and late vein stages. The early vein stages consists of quartz, pyrite, pyrrhotite, arsenopyrite, cassiterite and chalcedony. The late-vein stages are vertically zoned and consists of sphalerite-wurzite, galena and stannite group minerals in the lower levels, sphalerite-wurtzite, boulangerite, semseyite and fizelyite in the

upper levels and argentopyrite, teallite, frankeite, pyrargyrite, miargyrite, argentite and polybasite in near-surface levels (Malvicini, 1978). The second group is characterized by veins that are telescoped and extend to greater depths than those of the first group. Their mineralogy consists of quartz, cassiterite, pyrite, arsenopyrite, chlorite, chalcopyrite, sphalerite-wurtzite, stannodite, canfieldite, kesterite, freibergite, schimerite, schapbachite, alaskaite, bournonite, pyrargyrite, miargyrite, polybasite, stephanite and native silver. Locally vugs contain barite, antimonite, kaolinite and alunite (Malvicini, 1978).

Malvicini (1978) also described the paragenetic sequence of mineralization that consists of three stages: 1) host rock alteration, 2) early sulfide mineralization progressing into sulfosalt mineralization and 3) a second period of sulfosalt mineralization. By comparison with other deposits Malvicini (1978) estimated that the early sulfide mineralization of the second stage was deposited from hydrothermal fluids at 400 °C whereas the later sulfosalt mineralization of the second stage was deposited from hydrothermal fluids at 150 ºC to 300 °C.

3.0 Methods

3.1 Sample Collection and Preparation

Prior to beginning this study, 2.5 months were spent at the Pirquitas mine conducting field work, and reviewing exploration diamond drill core (15 holes) and historical data. Detailed logs of drill core through three cross-section of the CZ provided the basis for sampling. Additional review of drill core in the Huanuni Zone and San Miguel Zone was conducted. Representative samples of drill core were collected from the CZ (112), Huanuni (24) and from below the San Miguel Zone (4). In addition, grab specimens of veins and breccias were collected from the open pit that include a suite of five specimens from the Potosi Breccia North.

Sections of drill core were slabbed and polished to enhance mineral textures. Polished thin and thick petrographic sections were created for examination by transmitted and reflected light microscopy and SEM-energy dispersive spectroscopy (EDS). Clays were collected and concentrated from six areas within the CZ for later analysis by powdered X-ray diffraction (XRD).

3.2 Whole Rock Geochemistry and Geochemical Modelling

Whole rock geochemical data and diamond drill core logs were provided by Silver Standard Resources Inc., including metal concentration values by inductively coupled plasma atomic emission spectroscopy (ICP-AES) methods as outlined in Board et al. (2011). The quality of the data was assured by assessment of standards and blanks, detection limits and visual review of drill core. The geochemical data were modeled spatially using geochemical and geological modeling software where interpolation was done by dual kriging and inverse distance weighting (IDW) geostatistical methods. Using these methods, grade shells for the metals Ag, Zn, Sn, and Pb were created for the CZ, which incorporated independent interpolations within structurally bound domains. The grade shells were then used to produce longitudinal sections through the CZ.

3.3 Ore petrography and SEM-EDS

Polished thin and thick sections of mineralization were examined by transmitted and reflected light using an Olympus™ BX51 microscope. The mineralogy and textures were further assessed using a JEOL JSM-6400 scanning electron microscope (SEM) equipped with an Oxford Instruments™ INCA energy dispersive spectrometer (EDS) at Laurentian University, Sudbury. Analyses were performed with a beam current of ~1 nA, an accelerating voltage of 20 kV and varying live times between 5 and 30 s. The K-series X-ray lines were used for S, Fe, Cu and Zn, the L-series X-ray lines were used for As, Ag, Cd, In and Sn and the M-series X-ray lines were

used for Pb and Bi. Spot analyses were performed to determine mineralogy, including sulfosalts where possible.

3.4 Electron Microprobe (EMP)

The compositions of sulfosalts were determined quantitatively using a SX-50 Cameca electron microprobe (EMP) in the Central Analytical Facility of Laurentian University, Sudbury. The operating conditions were 20 kV and 20 nÅ with 10 s on the peak and 5 s on the background. The beam diameter was 5 μm. The standards were chalcopyrite (Fe, Cu, S), sphalerite (Zn), PtAs (As), Ag metal (Ag), Sn metal (Sn), RhSb (Sb) and PbTe (Pb).

3.5 Powdered X-ray Diffraction (XRD)

Pore-bound clays from six areas were manually concentrated into six samples and crushed in silica crucibles. The concentrates were analyzed by a Philips™ PW-1710 powder X-ray diffractometer (XRD) at the Central Analytical Facility of Laurentian University, Sudbury using CoKalpha radiation, a scan rate of 5 - 75 °2Θ, a step size of 0.02 °2Θ and a count time of 2 s/step. Spectra interpretation and mineral identification were performed using Pan Analytical™ HighScore Plus software.

3.6 Fluid Inclusion Analysis

Following reconnaissance for suitable material for fluid inclusion (FI) studies, two double-polished, 100 μm thick chips were made from sphalerite-rich samples whose mineralogy and chemistry had been characterized by petrography and SEM-EDS. Freezing and heating measurements were performed at the fluid inclusions laboratory of Laurentian University, Sudbury using a Linkam FTIR 600 heating-cooling stage coupled to an Olympus™ BX51 microscope. Calibration was carried out using synthetic FI standards containing pure H_2O (melting at 0 °C and critical behavior at 374.1 °C) and CO_2 (Tm -56.6 ºC). The methodology of FI assemblages (FIAs,

as defined by Goldstein & Reynolds, 1994) was used to characterize inclusions and guide thermometric data collection. However, due to the scarcity of fluid inclusions, in rare cases single FIs have been treated as FIAs where groups of FIs could not be measured. Single FIs are listed only where they are consistent with other FIA data and show no petrographic evidence for post-entrapment modification (i.e., necked shapes).

4.0 Results

4.1 General Characteristics

The CZ consists of an outer halo of mineralized crackle breccias and breccia veins that grade into a steeply dipping ESE-striking central breccia vein (Fig. 4). The central breccia vein is locally over 20 m wide, has a strike length of over 500 m and contains sulfide mineralization with open space filling textures. The margins of the central breccia vein are commonly flanked by weakly mineralized fault breccias. The central breccia vein contains massive-, colloform-, dendritic- and cockade-textured mineralization. Several syn- and post-mineral breccias are present with heterolithic clasts including fragments of mineralization supported in a rock flour matrix.

The mineralization is dissected by several N-S trending faults including the Cortaderas Fault and the Mirador Fault. The Cortaderas Fault has offset the central breccia vein with apparent right-lateral displacement of ~10 to 20 m. Displacement of the central breccia vein along the Mirador Fault is not apparent. The vertical extent of the central breccia vein is at least 400 m but remains open at depth.

4.2 Metal Distributions

Modelling of whole rock lithogeochemical trends shows distinct metal zonations on the scale of the mine area. The SMZ in the core of the open pit is enriched in Ag and Sn whereas

mineralization that is peripheral is more Zn-rich but contains less Ag and Sn. The CZ, being ~500 m from the SMZ, is very Zn-rich but depleted in Sn and Ag relative to other mineralized zones in the mine area. This same zonation is apparent vertically as well with deeper portions of the SMZ being the most enriched in Sn and Ag and upper portions being more enriched in Zn.

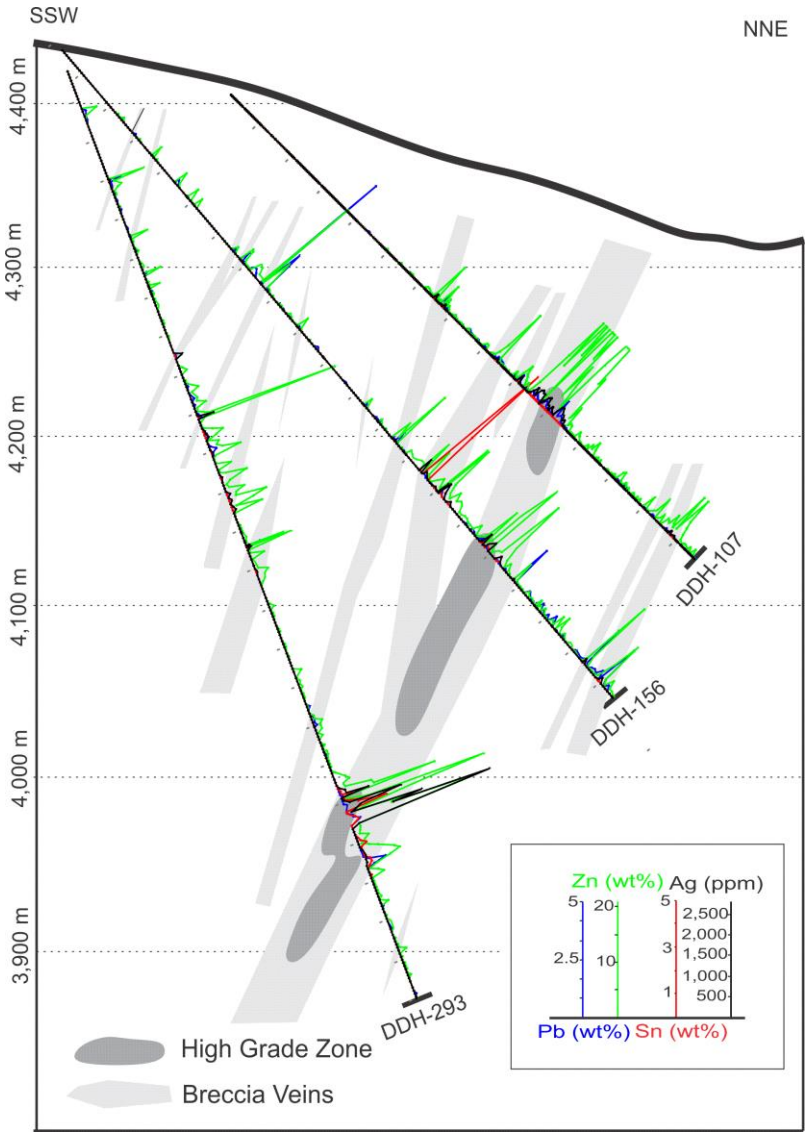

Figure 4: Schematic cross-section through the center of the CZ. The high-grade ore zone is indicated with the dark grey polygon. Inferred mineralized breccia veins are shown in light grey, as interpreted between drill holes based on geochemistry and observations of drill core. Metal concentrations are shown for Ag, Sn, Zn and Pb with equal scaling between holes.

The central breccia vein in the CZ extends approximately 500 m along strike and is locally over 20 m wide. It is apparent that at least two structures have restricted the distribution of metals; these are the Cortaderas Fault and the hinge of an anticlinal fold. The Mirador Fault does not appear to have had as strong an effect on the distribution of metals. In longitudinal section, it is apparent that the highest Ag, Sn, and Zn grades occur within these two structures and are restricted to depths below the 4,200 m level (Fig. 5). Overall, there is a special coupling between the four metals suggesting that the mineralization which hosts them is genetically or structural related.

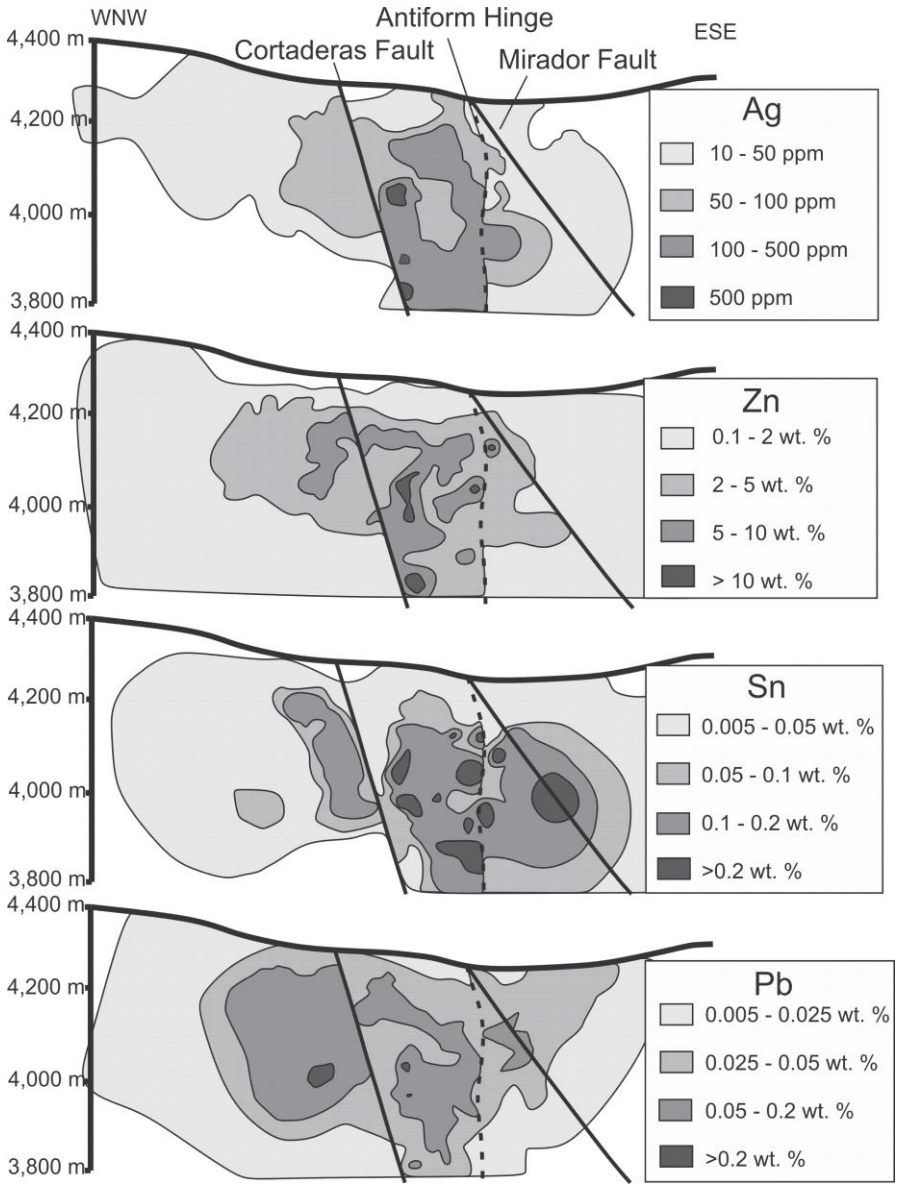

Figure 5: Longitudinal composite sections through the main breccia vein displaying interpolated grade shells for Ag, Zn, Sn and Pb.

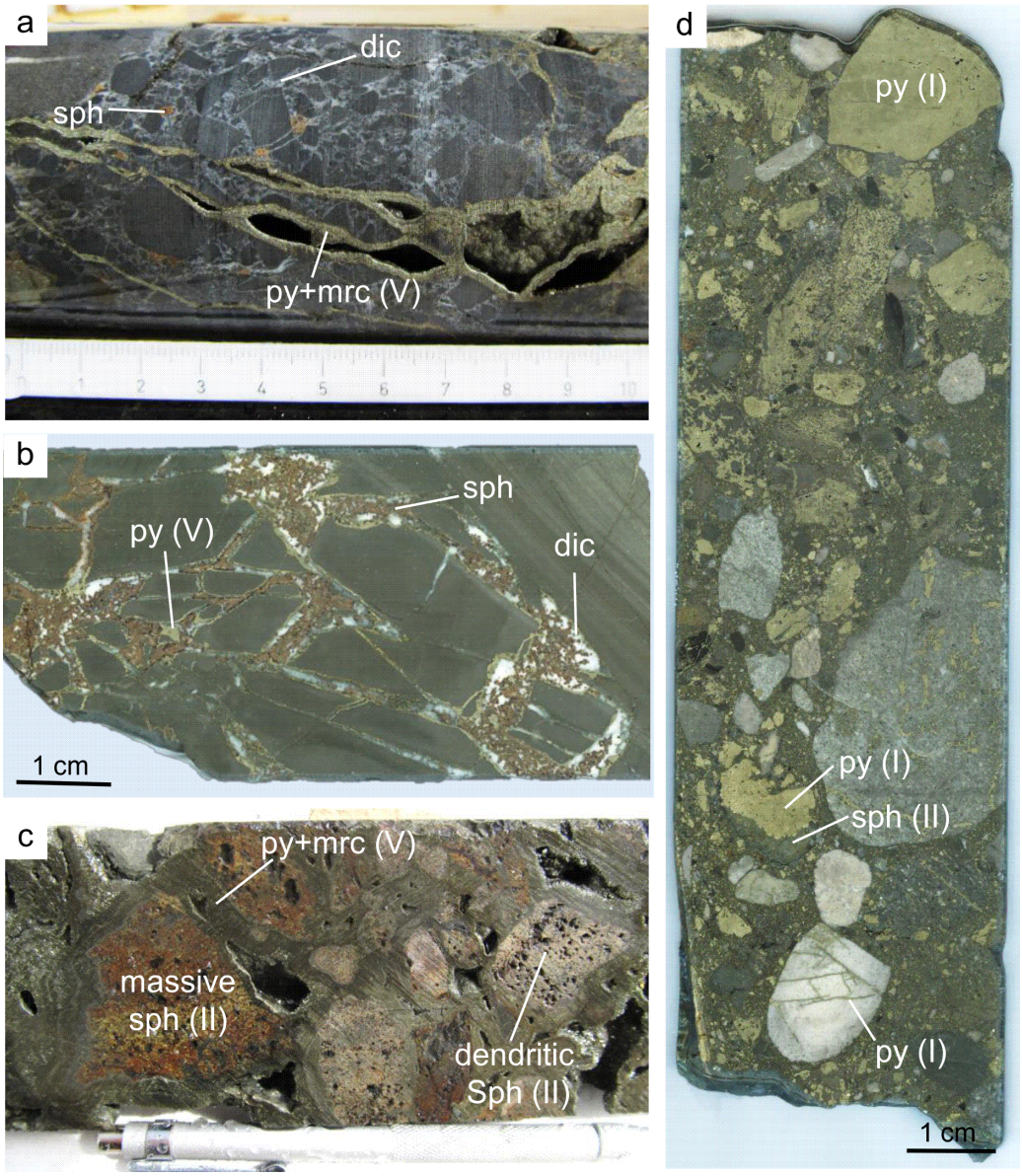

Figure 6: Examples of breccias in diamond drill core. (a) Fault breccia with a weakly clay-altered rock flour matrix. The principal clay mineral here is dickite (dic). Late colloform pyrite (py) and marcasite (mrc) coat fractures that cross-cut the breccia. (b) Crackle breccia with dickite, sphalerite and pyrite in the matrix. Alteration selvages exist locally. (c) Heterolithic breccia with clasts of massive and dendritic sphalerite (sph). The matrix is composed of colloform pyrite and marcasite. (d) Polylithic breccia resembling a phreatic breccia with clasts of mineralization, and variably altered wall rock of sedimentary and probable igneous origins.

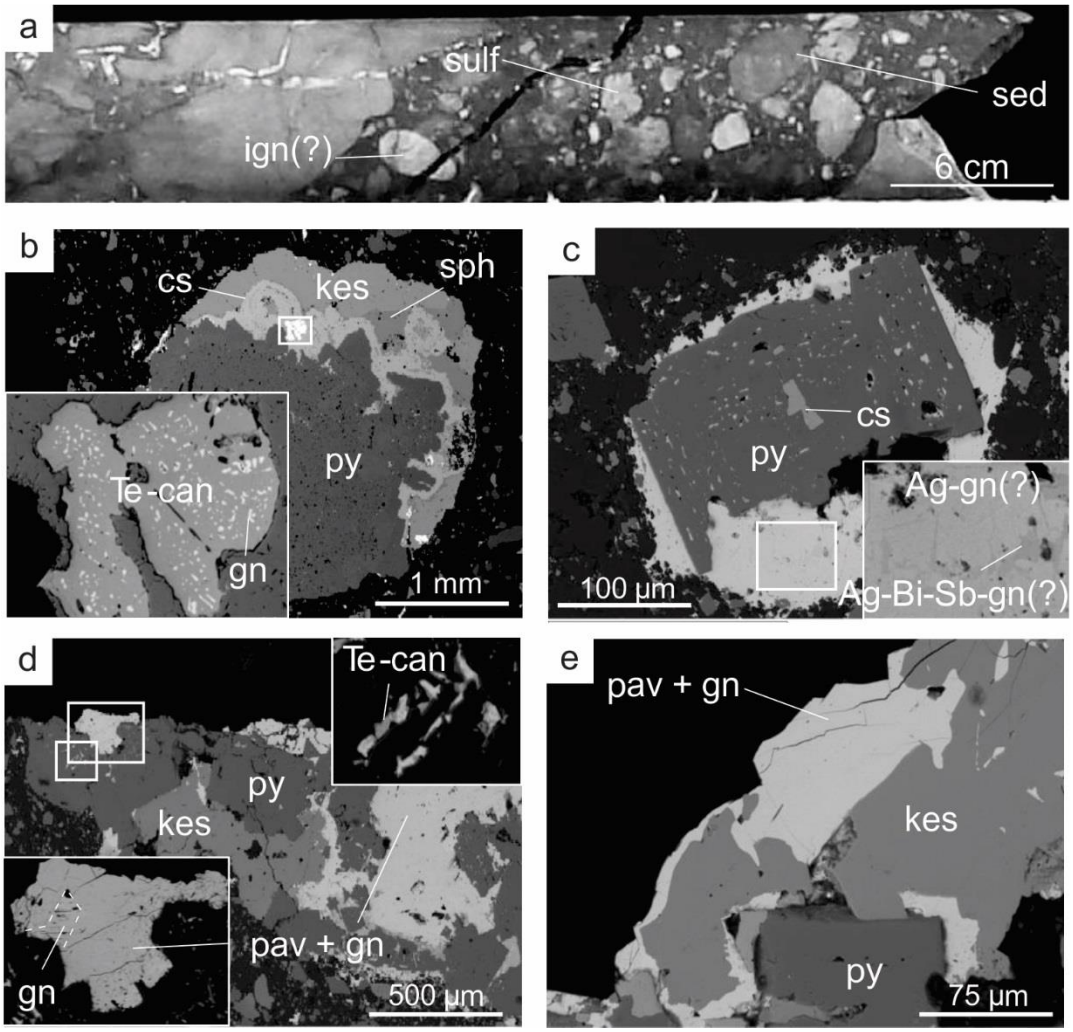

Figure 7: Petrography of a pebble-dyke breccia cross-cutting mineralization. (a) Image of the pebble-dyke breccia in diamond drill core that contains rounded heterolithic fragments including highly altered igneous rocks(?) (ign?), metasedimentary wall rock (sed), and sulfide-rich fragments (sulf). (b) Rounded clast with massive pyrite (py), colloform cassiterite (cs), clots of Te-bearing canfieldite (Te-can) that contain blebby inclusions of galena (gn). (c) Rounded clasts with an inclusion-rich pyrite core surrounded by an intergrowth of two minerals that chemically resemble Ag-bearing galena (Ag-gn(?)) and Ag-Bi-Sb-bearing galena (Ag-Bi-Sb-gn(?)). (d) Clast with pavonite (pav), galena, pyrite, kesterite (kes) and minor amounts of Te-bearing canfieldite. (e) Clast with pavonite with galena inclusions, kesterite and pyrite.

4.3 Breccia Descriptions

A variety of breccia types are identified that include fault breccias, crackle breccias, phreatic breccias and pebble-dyke breccias (Figs. 6, 7, Table 1). Fault breccias are matrix- to clast-supported and comprise rotated clasts of unmineralized wall rock in matrices of altered rock flour

(Fig. 6a). The matrices of fault breccias contain minor amounts of disseminated sulfide mineralization and are clay-altered. Crackle breccias are fracture arrays cemented by hydrothermal minerals such as sphalerite, dickite, quartz, pyrite and marcasite that support unrotated clasts of wall rock (Fig. 6b). In the central breccia vein, several episodes of mineralization and brecciation resulted in cockade textures with clasts of mineralization being supported by sulfide matrices (Fig. 6c). Phreatic breccias are pipe- or vein-shaped bodies with rock flour matrices that support rounded, heterolithic clasts of variably altered wall rock, as well as sulfide minerals (Fig. 6d). Pebble-dyke breccias are similar to the phreatic breccias but have a higher clast to matrix ratio (Fig. 7).

Table 1: Descriptions of breccia types.

Breccia Type	Internal organization	Clast shape and type	Matrix	Alteration and mineralization
Fault breccia	Clasts rotated, matrix supported	Shape: Rounded to subangular Type: Sandstone, siltstone, black shale, qtz veins	Rock flour, mud- to sand-sized fragments	Minor clays, disseminated py and sph
Crackle breccia	Clasts not rotated to locally rotated, clast supported	Shape: Angular Type: Sandstone, siltstone, shale, qtz vein	py, sph, clay, qtz	Qtz, clay, py alteration
Phreatic breccia	Clasts rotated, matrix- to clast-supported	Shape: Rounded to subangular Type: Sandstone, siltstone, quartz eyes, igneous(?)	Rock flour; mud- to sand-sized fragments	Clays, py, sph, gn,
Pebble-dyke breccia	Clasts rotated, matrix supported	Shape: Rounded Type: Sandstone, siltstone, shale, sulfide, intrusive	Rock flour, mud- to sand-sized fragments	Qtz, clays, py, sph

qtz - quartz, py - pyrite, sph - sphalerite

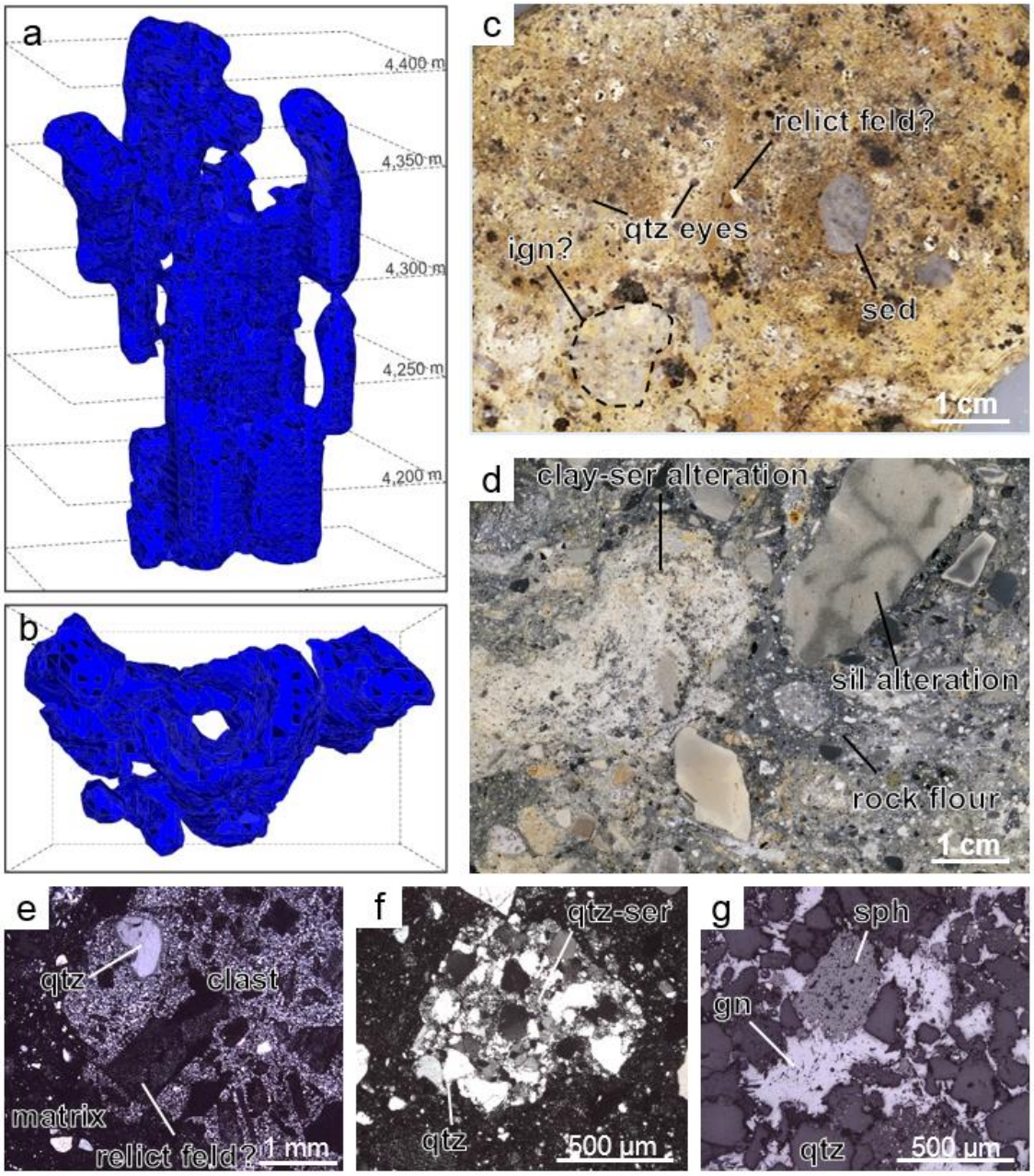

Figure 8: Morphology and petrography of the Potosi Breccia North, the largest breccia body on the property. (a, b) Section and plan view of the breccia pipe morphology provided by Silver Standard Resources Inc. (c) Cut grab sample of altered breccia with clasts of sedimentary rocks (sed) as well as some of probable igneous (ign?) origin. Quartz (qtz) eyes are abundant along with clots of clay and sulfide minerals. (d) Cut grab sample of more weakly altered breccia. Clasts of sedimentary rocks have silica alteration halos and selvages. The matrix is dominantly grey rock flour. (e, f) Thinsection micrographs under cross-polarized transmitted light of clasts. (e) Rounded quartz eyes and tabular altered crystals, possibly relict feldspars (feld?) in a clast. (f) Seriate-textured quartz-rich clast with minor sericite (ser). (g) Polished thin section photomicrograph under reflected light of a breccia sample with sphalerite (sph) and galena (gn) composing the cement.

The Potosi Breccia North is the largest breccia body in the mine area (Fig. 8). It is roughly cylindrical in shape, over 100 m wide, and has a known vertical extent of at least 250 m. A suite of grab samples were studied from this breccia body for comparison to breccia bodies in the CZ. The breccia is heterolithic, with clasts of altered metasedimentary rocks, quartz eyes, and rocks of probable igneous origin. The matrix consists of rock flour with locally fluidal-like textures and sphalerite, galena and pyrite occurring locally as cement. Sericite and clay alteration are pervasive in clasts of probable igneous origin and locally strong in the matrix. Some strongly altered portions of the matrix could be of igneous origin or contain an igneous component. Some clasts have porphyritic textures with relict feldspar phenocrysts and quartz eyes. The breccia has formed over several stages evidenced by the appearance clasts of previously cemented breccia.

4.4 Mineralization and Alteration

The mineralization consists principally of sphalerite, pyrite, marcasite, arsenopyrite, cassiterite, galena and various Ag-, Sn-, As-, Sb-, Pb-, Cu- and Bi-bearing sulfosalts, as determined by SEM analyses and their optical properties (Table 2). In general, gangue minerals are subordinate to ore minerals in the studied samples and include quartz, clays and siderite as well as minor amounts of goyazite and unidentified REE-bearing hydrous phosphates (Fig. 10). Wall rock alteration is minor, generally occurring as selvages several millimeters to tens of centimeters wide that include clay alteration, sericitization, chloritization, and silicification. The powdered XRD spectra for six clay samples revealed dickite to be the dominant clay mineral with kaolinite being present in one of the samples. Sphalerite, pyrite, and marcasite are also present.

Breccia bodies, such as the pebble-dyke breccia shown in Figure 7, locally contain clasts of mineralization whose mineralogy differs from that which is typical for the ore zone. One clast contains massive pyrite that is coated with a band of colloform cassiterite that contains clots of Te-

bearing canfieldite (Fig 7b). The Te-bearing canfieldite has fine-grained blebby inclusions of galena disseminated throughout. Other may be Pb-Ag-Bi-Sb-bearing minerals, some of which may be impure galena and others may be sulfosalts such as pavonite (Fig. 9c, d, e). Kesterite also occurs intergrown with these Pb-Ag-Bi-Sb-bearing phases.

Table 2: Representative chemical analyses for sulfosalts by EMPA. The formula for Te-bearing canfieldite was calculated assuming S + Te + Se = 6. The formula for pavonite was calculated assuming all Pb was present as PbS inclusions.

Mineral	Te-Canfieldite	Pavonite(?) + Galena(?)	Proustite	Miargyrite	Pyrargyrite	Boulangerite	Kesterite	Tetrahedrite	Jordanite	Hocartite
Stage	?	?	II	III	III	III	III	III	III	VII
n =	3	4	1	3	1	1	2	19	4	1
Wt. % (avg.)										
Ag	62.31	10.96	65.32	35.70	59.45	0.09	0.79	24.22	0.09	41.12
Cu	0.00	0.00	0.01	0.01	0.00	0.00	28.92	19.16	0.00	0.05
Fe	0.01	0.37	0.02	0.00	0.02	0.00	3.50	2.91	0.00	9.27
Sb	0.00	0.66	0.73	40.52	20.69	24.75	0.00	24.45	4.73	0.00
Sn	8.73	0.34	0.05	0.22	0.08	0.12	27.23	0.21	0.12	23.15
As	0.00	0.00	13.54	1.03	1.68	1.07	0.00	1.81	7.93	0.00
Zn	0.00	0.01	0.00	0.00	0.00	0.00	10.66	3.20	0.03	1.31
Pb	1.17	6.54	0.00	0.00	0.00	55.21	0.00	n.a.	68.95	0.00
Te	18.14	0.33	0.00	0.00	0.00	0.00	0.00	n.a.	0.00	0.00
Se	0.09	0.01	0.00	0.02	0.16	0.00	0.00	n.a.	0.00	0.08
Bi	0.00	62.85	0.00	0.74	0.00	0.00	0.00	n.a.	0.00	0.00
S	9.34	17.44	18.90	20.91	17.68	18.25	29.14	23.60	17.94	24.11
Total	99.79	99.51	98.58	99.16	99.76	99.48	100.25	99.56	99.78	99.10
APFU calculated to S =	6.00	5.00	3.00	2.00	3.00	11.00	4.00	13.00	23.00	4.00
Notes:	(+ Te + Se)	(PbS removed)								
Ag	7.59	0.37	3.08	1.02	3.00	0.02	0.03	3.97	0.03	2.03
Cu	0.00	0.00	0.00	0.00	0.00	0.00	2.00	5.33	0.00	0.00
Fe	0.00	0.02	0.00	0.00	0.00	0.00	0.28	0.92	0.00	0.88
Sb	0.00	0.02	0.03	1.02	0.92	3.93	0.00	3.55	1.60	0.00
Sn	0.97	0.01	0.00	0.01	0.00	0.02	1.01	0.03	0.04	1.04
As	0.00	0.00	0.92	0.04	0.12	0.28	0.00	0.43	4.35	0.00
Zn	0.00	0.00	0.00	0.00	0.00	0.00	0.72	0.87	0.02	0.11
Pb	0.07	0.12	0.00	0.00	0.00	5.15	0.00	0.00	13.68	0.00
Te	1.87	0.01	0.00	0.00	0.00	0.00	0.00	0.00	n.a.	0.00
Se	0.02	0.00	0.00	0.00	0.01	0.00	0.00	0.00	n.a.	0.01
Bi	0.00	1.11	0.00	0.01	0.00	0.00	0.00	0.00	n.a.	0.00
S	3.83	2.00	3.00	2.00	3.00	11.00	4.00	13.00	23.00	4.00

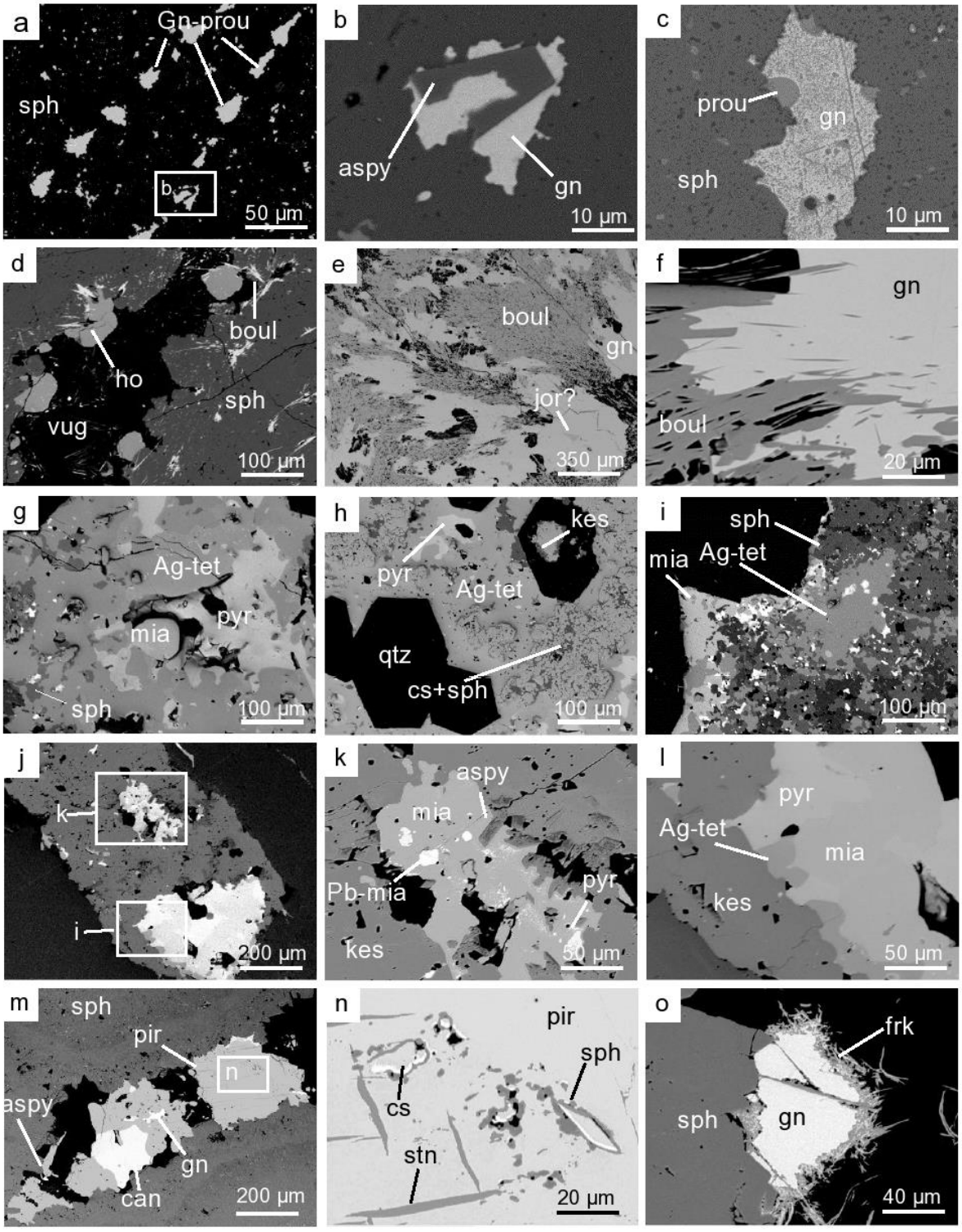

Figure 9*:* Backscattered electron images of mineralization from several paragenetic stages (II, III, VI and VII). (a, b, c) Polymetallic inclusions in colloform sphalerite (sph) of stage II mineralization. Galena (gn) is the main phase and it locally contains blebby inclusions of proustite (prou). In rare cases these inclusions also contain arsenopyrite (aspy). (d, e, f) Lead and Sb mineralization in veins of stage III with galena that contains inclusions of jordanite(?) (jor?). This

galena is overgrown by fibrous boulangerite (boul). Sphalerite and hocartite of stage VII overgrows the boulangerite and exists in vugs. (g, h, i) Polymetallic mineralization of stage III occurring as a 1-2 cm thick crust on a clast of massive stage I pyrite. The main phases include Ag-bearing tetrahedrite (Ag-tet), pyrargyrite (pyr), miargyrite (mia), cassiterite (cs) and sphalerite. Minor Pb-Bi-Ag clots are present locally and appear white in this SEM image. Euhedral quartz (qtz) often hosts inclusions of cassiterite but predates most other minerals of this stage. (j, k, l) Polymetallic mineralization of stage VI occurring as fine veinlets in fractures. The main phases include kesterite (kes), pyrargyrite, miargyrite, and Ag-bearing tetrahedrite. Some Pb-Sb-bearing mineral inclusions in miargyrite are present and appear as white spots. (m, n, o) Polymetallic mineralization of stage VII occupying pores in colloform sphalerite. Pyrite, arsenopyrite, sphalerite, cassiterite, canfieldite (can) and galena formed first in this stage and have been overgrown by pirquitasite-hocartite (pir-ho) and minor frankeite (frk). Pirquitasite contains abundant exsolution lamellae of stannite (stn) and locally contains inclusions of cassiterite and sphalerite. Galena is locally coated by fibrous frankeite as is seen in image "o".

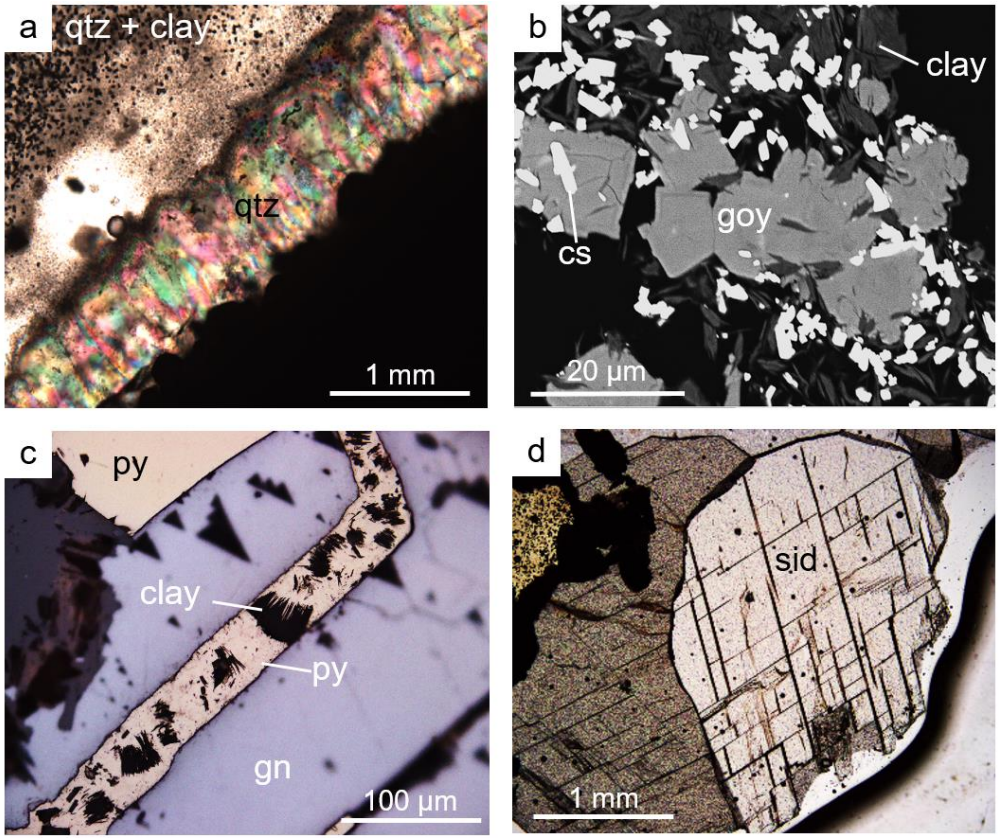

Figure 10: Petrographic and backscattered electron images of gangue and alteration minerals. (a) Comb-textured quartz (qtz) of stage I and massive amorphous quartz with clays of stage V in the matrix of a crackle breccia. (b) Cassiterite (cs), clays and goyazite (goy) of stage V disseminated throughout an altered clasts. (c) Book-like clusters of clays from stage V occurring as intergrowths in pyrite (py) of the same stage. The pyrite and clays are in a fracture that cross-cuts galena (gn) from stage II. (d) Siderite from stage V occurring in the matrix of a crackle breccia.

Paragenesis

The CZ formed during a protracted paragenesis with many stages of brecciation, crystallization, remobilization and alteration. On the basis of observed layering, cross-cutting relationships and replacement of minerals, eight paragenetic stages are documented and summarized in Figure 11. No single observed sample contained all of the stages however, the sample in Figure 13 contains several of them. The distinguishing features of each stage are described below. These stages are referred to in figures as well as in subsequent sections of this article.

		Pyritization (I)	Sph (II)	Ag (III)	Sph (IV)	Massive Sulfide (V)	Ag (VI)	Ag-Sn (VII)	Waning (VIII)
Gangue	Quartz	X	X	X		XX			X
	Sericite	X							X
	Clays					X			XXX
	Goyazite					X			X
	Siderite					X			X
Sulfides	Pyrite	XXX	X	XX	X	XXX	X	X	X
	Sphalerite		XXX	XX	XX	XX	X	X	
	Marcasite					XX			X
	Arsenopyrite		XX	XX			X	X	
	Galena		XX	XX				XX	
	Cassiterite			X		X		X	
Sulfosalts	Proustite-Pyrargyrite		X	X			X		
	Jordanite			X					
	Kesterite-Stannite			X		X	XXX	X	
	Smithite-Miargyrite			X			X		
	Ag-bearing Tetrahedrite			XX			X		
	Boulangerite			X					
	Frankeite							X	
	Canfieldite							XX	
	Pirquitasite-Hocartite							XX	

– – – – – – – – Brecciation **XXX** - Very Abundant **XX** - Abundant **X** - Present

Figure 11: Paragenetic sequence showing the relative abundances of minerals deposited during each stage. All stages with the exception of stages IV and VII were preceded by a brecciation event at indicated by the dashed lines.

Stage I

This stage is characterized by the mechanical preparation and alteration of the host rocks. Dilation along a pre-existing fault accompanied by hydraulic fracturing enabled hydrothermal fluids to penetrate and alter the wall rocks. Pyrite replaced the wall rock to form zones of massive

pyrite in the area of the central breccia structure (Figs. 12a, 13a). The shapes of relict clasts of wall rock are preserved in these massive pyrite replacement zones. Quartz and pyrite were precipitated into fractures resulting in a stockwork of veinlets, some of these are preserved in clasts (Fig. 6d). In addition, fracture-controlled and disseminated sericite and chlorite alteration occurred locally during this stage.

Stage II

This is the principal stage of Zn mineralization and also marks the onset of Ag mineralization. Sphalerite is the dominant mineral along with lesser amounts of galena, arsenopyrite and pyrite and minor amounts of proustite. It was initiated following dilation and local brecciation that permitted the formation of open-space-filling textures including colloform, crustiform, dendritic, and massive (Fig. 12). The textures of sphalerite vary with depth such that it occurs with massive, coarsely banded crustiform, textures in the upper levels whereas it occurs with finely laminated colloform as well as dendritic and feathery textures in the deeper levels. Colloform sphalerite occurs as botryoidal shaped masses composed of fine layers that exhibit rhythmic color banding whereby it transitions from dark brown sphalerite to light tan sphalerite within each depositional cycle (Fig. 12a). Sphalerite is intergrowth with arsenopyrite and galena which contains fine-grained blebby inclusions and larger globules of the proustite (Fig. 9a, b, c). The proustite inclusions in galena are most abundant in deeper levels where sphalerite has well-developed colloform textures. Dendritic sphalerite occurs as branching aggregates of fine spherules occurring with colloform sphalerite (Fig. 12b, c, e). As a general trend, dendritic sphalerite grades into colloform sphalerite.

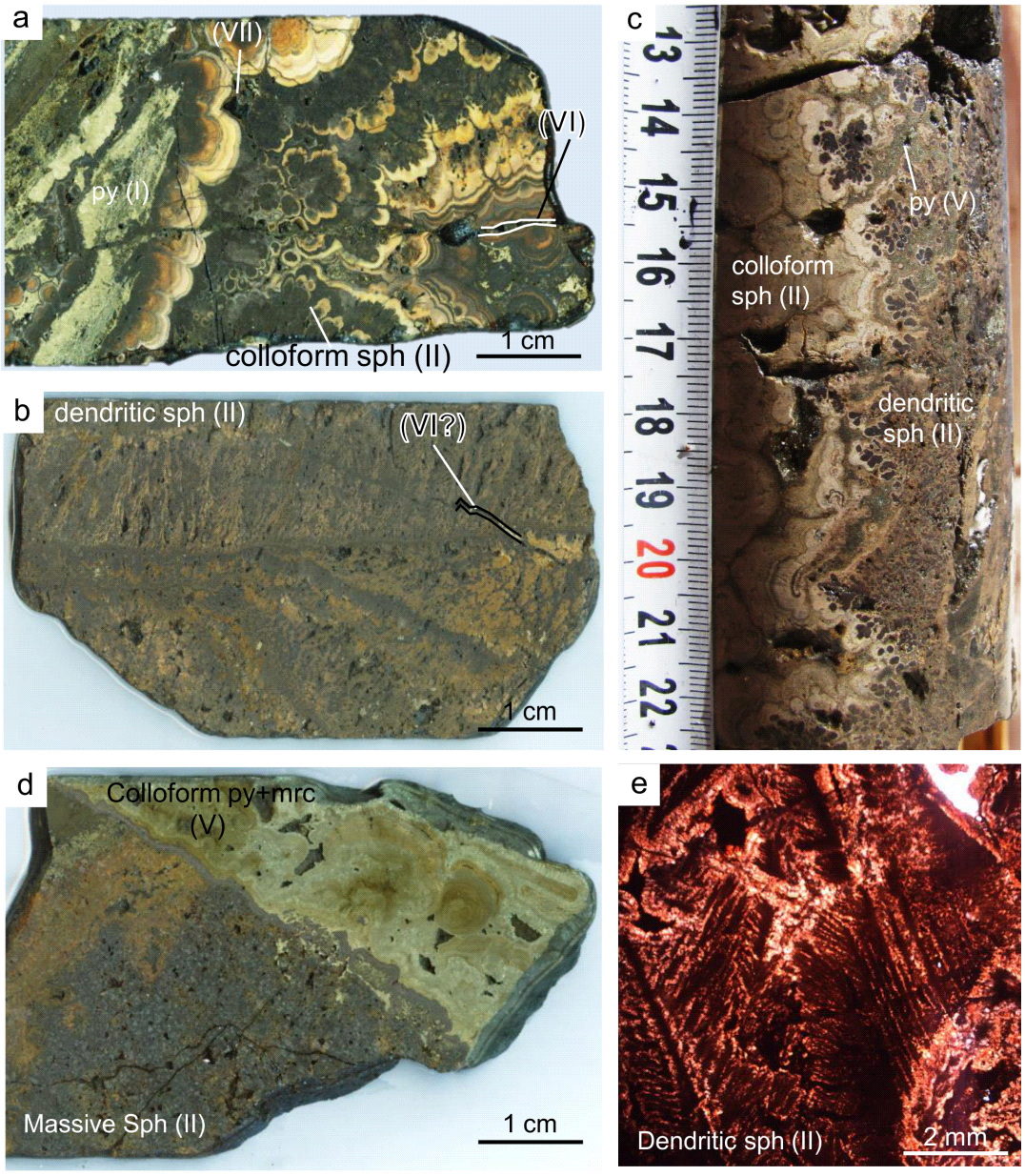

Figure 12: Examples of colloform, dendritic and massive textures in drill core and thin sections. (a) Well-formed colloform-textured sphalerite (sph) from stage II that formed during several depositional cycles. It formed on a clast of stage I pyrite. (b) Dendritic sphalerite from stage II that also formed in several cycles. (c) Dendritic dark brown sphalerite that transitions into colloform tan sphalerite. (d) Colloform pyrite (py) and marcasite (mrc) from stage V that are interlayered and occur coating massive sphalerite from stage II. (e) Thinsection micrograph displaying dendritic/feathery sphalerite from stage II.

Stage III

This is the main stage of Ag mineralization and is characterized by mineralization that is vertically zoned. It followed a brecciation event that is evidenced by its occurrence as crusts on clasts and breccia walls. In deep levels (i.e., below 4150 m ASL), clasts of sulfide minerals and pyrite-altered wall rock are encrusted with dark sulfosalt-rich bands that contain sphalerite, Ag-bearing tetrahedrite, pyrargyrite, miargyrite, an unidentified Ag-Sb-Pb-sulfosalt, pyrite, cassiterite, lesser amounts of kesterite and minor amounts galena and unclassified Bi-Pb-bearing minerals (Fig. 9g, h, i). In the upper levels of the ore zone, the stage is characterized by narrow (<10 cm wide) Pb-Sb-As-rich veins with galena, boulangerite, and jordanite where galena and jordanite are intergrown (Fig. 9d, e, f). The relationship between boulangerite and galena is not clear. Where the two minerals are present, the galena is anhedral and highly porous with boulangerite filling the pores.

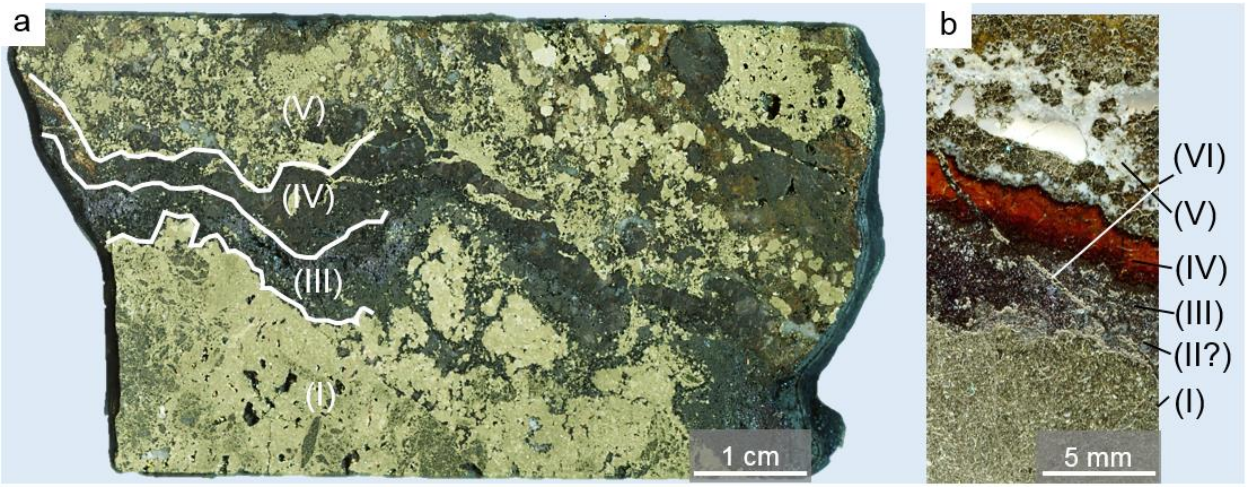

Figure 13: Image drillcore (a) and a polished thick section (b) with high-grade Ag-mineralization. Mineralization from paragenetic stages I to VI are labelled.

Stage IV

This stage consists a 0.2-1 cm thick band of weakly colloform to crustiform sphalerite (Fig. 13). It appears to be concordant with mineralization of stage III and, therefore, may not have

precipitated immediately following a brecciation event. The sphalerite has oscillatory color banding. As a general trend, the early-formed layers of this sphalerite are light orange in color and the late-forming layers are dark brown in color but this trend is locally reversed.

Stage V

This stage consists of abundant massive sulfide accompanied by gangue minerals. The dominant minerals are pyrite, marcasite, quartz, cassiterite, clays and siderite. Pyrite occurs as colloform interlayerings with marcasite (Figs. 6a, 6c, 12d) and as individual grains or aggregates of grains that are concentrically zoned. The cores of pyrite grains are inclusions free whereas the growth zones often contain mineral inclusions. Quartz of this stage is euhedral and contains rare inclusions of cassiterite. Fibrous and feather-like orange sphalerite fills the interstitial space accompanied by aggregates of acicular cassiterite. Siderite formed during this stage, predominantly in the upper levels of the ore zone in areas peripheral to the central breccia vein.

Stage VI

This stage is characterized by narrow veinlets (~1 mm wide) containing abundant kesterite and pyrite and minor amounts of sphalerite, arsenopyrite, Ag-bearing tetrahedrite, miargyrite, pyrargyrite and an Ag-Sb-Pb-bearing phase whose composition resembles Pb-bearing miargyrite but may be a different mineral. The Ag-bearing tetrahedrite, miargyrite and pyrargyrite occur intergrown together (Figs. 9j, k, l, 13b). The Ag-Sb-Pb-bearing phase is found as rounded inclusions in miargyrite with diffuse boundaries. In this stage, kesterite is the dominant sulfosalt whereas Ag-tetrahedrite is only a minor phase.

Stage VII

This stage is characterized by an abundance of Sn-bearing sulfosalts and scarcity of Ag-Sb-bearing sulfosalts. The minerals pyrite, sphalerite, arsenopyrite, galena, canfieldite,

pirquitasite-hocartite, cassiterite, stannite and frankeite occur in vugs and pores within earlier mineralization (Fig. 9m, n, o). Unlike stage III, which is vertically zoned, this stage is evenly dispersed throughout the ore zone. The stage can be further broken into substages. Sphalerite, pyrite, cassiterite, arsenopyrite, galena and canfieldite formed first. The arsenopyrite occurs as elongate euhedral crystals with rare inclusions of cassiterite. Galena and canfieldite share grain boundaries and locally occur as blebby or globular inclusions within each other. These minerals which formed first in this stage have been overgrown by minerals of the pirquitasite-hocartite series. The Zn-rich grains of pirquitasite-hocartite (i.e., pirquitasite) contain exsolution lamellae of stannite (Fig. 9n), whereas Fe-rich grains (i.e., hocartite) do not (Fig. 9d). Fibrous frankeite has coated the surfaces and fracture planes of some galena grains (Fig. 9o).

Stage VIII

This stage contains mineralization and alteration that signifies the waning of the hydrothermal system. Clays, mostly dickite, along with minor amounts of siderite, quartz, and hydrous phosphates such as goyazite were deposited in vugs and as alteration selvages in the immediate wall rock. The siderite of this stage is anhedral and contains abundant clay inclusions.

4.5 Fluid Inclusions

A petrographic and microthermometric study of sphalerite-hosted fluid inclusions (FIs) was performed to determine the nature of the hydrothermal fluids and to identify ore-forming processes. Heating and freezing measurements were performed on 123 FIs in 21 fluid inclusion assemblages (FIAs). A summary of the microthermometric data is given in

Table 3, representative images of FIs and their host crystals are shown in Figure 14 and bar graphs displaying the mean, range and sample size are shown in Figure 15.

Coarse crystals of sphalerite within colloform sphalerite from stage II (Fig. 14a) contain at least two types of FIs. Type-I FIs are irregular in shape, vapor-rich and generally occur along primary growth zones (Fig. 14d, e, f). Although they are locally abundant, only two FIs of this type were suitable for Th determination and yielded Th values of 322 ± 0.2 °C and 340 ± 10 °C. The first of these FIs was suitably necked as to allow for precise measurement of the Th (measurement error of ±0.2 °C) (Fig 14e) whereas the second had an elongated shape which did not allow for precise measurement of the Th (measurement error of ±10 °C) (Fig. 14f). It was not possible to determine the Tmice for either of these inclusions. Due to the low amount of liquid present and challenging optics, one cannot rule out that they have experienced post-entrapment modification (e.g., Bodnar, 2003). Type-II FIs are more abundant, liquid-rich and appear to mostly cross-cut primary growth zones and thus are interpreted as being of secondary or pseudosecondary origin (Fig. 14b, c). The FIAs of type-II have average $Tm_{(ice)}$ between -0.1 °C and -2.9 °C which equates to 0.2-4.8 wt. % NaCl equivalent and Th values between 207 °C and 227 °C. There is no correlation between Th and $Tm_{(ice)}$, as the average Ths do not significantly vary between FIAs. Based on the observed eutectic temperatures (Te) between -30 °C and -24 °C, the fluid chemistry is considered to be best approximated by the H_2O-NaCl system (Te of -21.1 °C) with a small amount of undetermined divalent cations (e.g., Ce, Fe, Mg).

Table 3: Fluid inclusion assemblage (FIA) microthermometric data summary.

Stage	FIA	No. of inclusions measured	Type	V:L (Visual)	Long axis (µm)	TF (°C)	Te (°C)	Tm Ice (°C)	Th (°C)	Salinity (wt. % NaCl equiv.)
Sample DDH-230C										
II	1	10	S/PS	0.15	22	-44.5		-2.8	209.1	4.68
II	2	3	S/PS	0.15	42			-2.8	212.3	4.65
II	3	6	S/PS	0.1	22	-50	-30	-2.7	213.7	4.54
II	4	4	S/PS	0.1	26		-24.3	-2.8	211.4	4.65
II	5	4	S/PS	0.13	28				211.6	
II	6	6	S/PS	0.15	15			-2.9	213.8	4.8
II	7	14	S/PS	0.1	18			-2.7	213.3	4.48
II	8	5	S/PS	0.1	32		-24.5	-1.4	208	2.37
II	9	1	S/PS	0.1	30		-25	-2.7	223.3	4.49
II	10	6	S/PS	0.1	29			-2.7	214.7	4.53
II	11	12	S/PS	0.15	21			-1.8	214.6	3.06
II	12	14	S/PS	0.1	16			-0.8	207.4	1.46
II	13	12	S/PS	0.15	37		-23.1	-0.5	214.2	0.88
II	14	5	S/PS	0.15	40			-1.1	207.7	1.91
II	15	1	S/PS	0.2	53			-0.1	227	0.18
II	N/A	1	P	0.95	50				322	
II	N/A	1	p	0.9	19				340	
Sample DDH-230I										
IV	16	4	S	0.2	15			-1.4	259.4	2.41
IV	17	3	S	0.2	15			-1.4	255.7	2.41
IV	18	3	P	0.2	7			-2.4	235.3	4.03
IV	19	1	P	0.2	20			-4.5	278.5	7.17
IV	20	2	P	0.2	35			-3	256.6	4.88
IV	21	5	P	0.2	20			-1.3	282.1	4.18

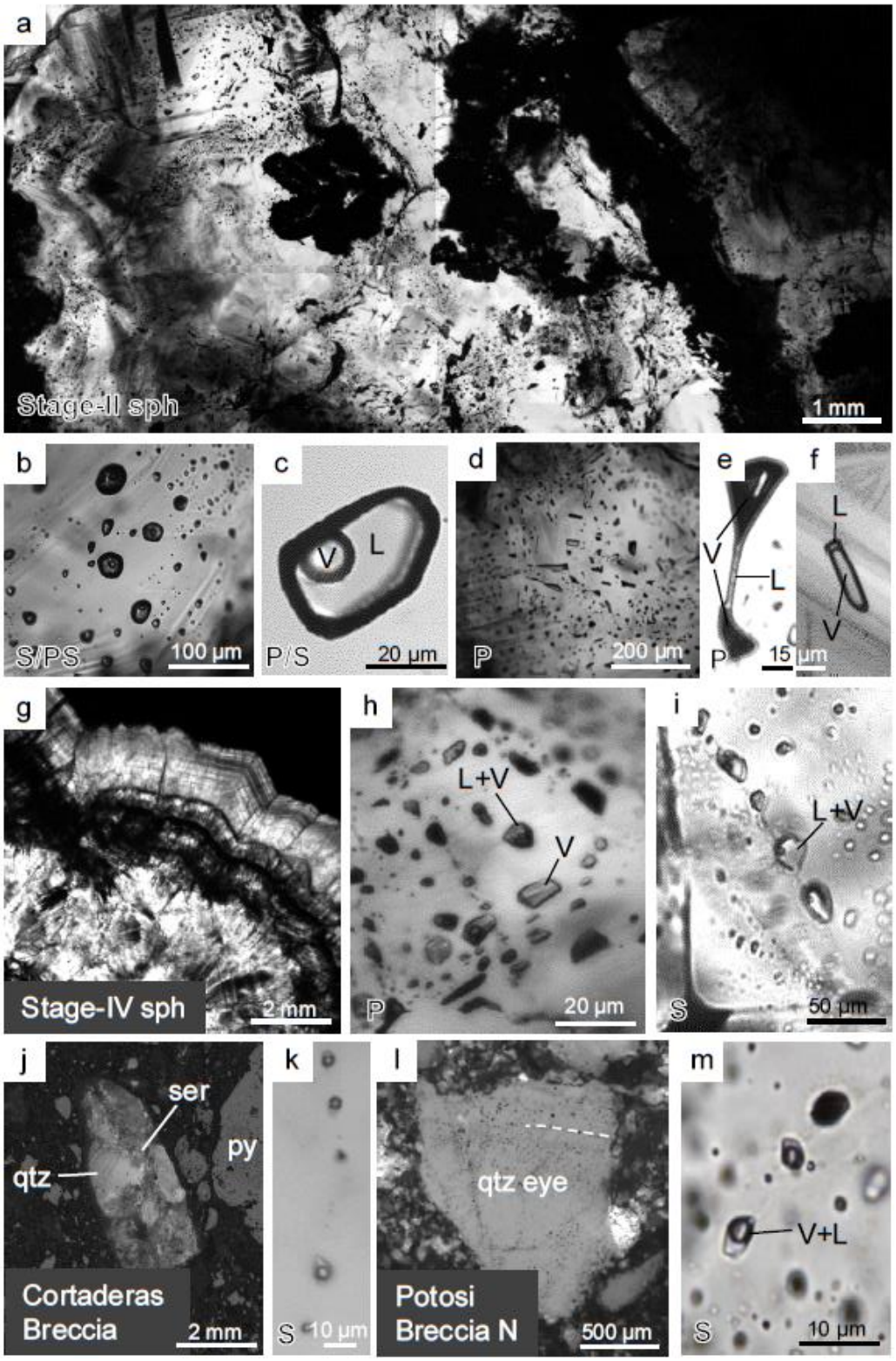

Figure 14: Petrography of fluid inclusions (FIs) in sphalerite (sph) and breccia-hosted quartz fragments. Fluid inclusion photomicrographs were taken with short wave infrared transmitted light. (a) Colloform sphalerite of stage II with alternating bands of dark and light sphalerite. (b, c)

Secondary or pseudosecondary (S/PS) liquid (L)-rich FIs in stage II sphalerite. (d, e, f) Primary (P) vapor (V)-rich FIs in stage II sphalerite, two of which were suitable for microthermometry. (g) Colloform sphalerite of stage IV. (h) Primary FIs in stage IV sphalerite containing vapor and liquid in variable proportions that likely formed from heterogeneous entrapment of a boiling fluid. (i) Secondary liquid-rich FIs in stage IV sphalerite that formed along annealed fractures. (j) Quartz-rich clast of unknown provenance in a pebble-dyke breccia. (k) Secondary FIs with roughly equal proportions of liquid and vapor in an annealed fracture cutting quartz from image "k". (l) Quartz eye of unknown provenance in the Potosi Breccia North. (m) Secondary FIs with roughly equal liquid-to-vapor ratios in an annealed fracture cutting quartz from image "l".

Banded to colloform sphalerite of stage IV mineralization contains two types of FIAs (Fig. 14g). Type-I FIAs appear along primary growth zones and are of primary origin. Some inclusions in the FIAs have mixed vapor-to-liquid ratios suggesting heterogeneous entrapment of a boiling fluid (Fig. 14h). These FIAs yielded $Tm_{(ice)}$ between -1.3 °C to -4.5 °C and Th values between 257 °C and 282 °C. Type-II FIAs occur along annealed fractures that extend to the grain boundaries and are, therefore, of secondary origin. The type-II FIs have consistent vapor-to-liquid ratios and two FIAs of this type yielded average $Tm_{(ices)}$ of -1.4 °C (2.4 wt. % NaCl equivalent) and Th values of 256 °C and 259 °C (Fig. 14i).

Although only two samples of sphalerite were studied by microthermometry a more extensive petrographic study of numerous samples, including those with quartz-hosted FIs, was conducted. Sparse fluid inclusions in quartz are liquid-rich (~80 to 90 % liquid) and similar to the type-II secondary/pseudosecondary FIAs observed in sphalerite of both stages II and IV. In some exotic quartz fragments (i.e., broken quartz veins, quartz eyes) within a pebble-dyke breccia in the CZ and in the Potosi Breccia North, secondary FIAs are present that have high vapor-to-liquid ratios (i.e., estimated visually at 0.4-0.6) and locally display heterogeneous entrapment. These FIAs represent the trapping of relatively high-temperature fluids that exhibited near-critical behavior and in some cases may have been boiling (Fig. 14j, k, l, m).

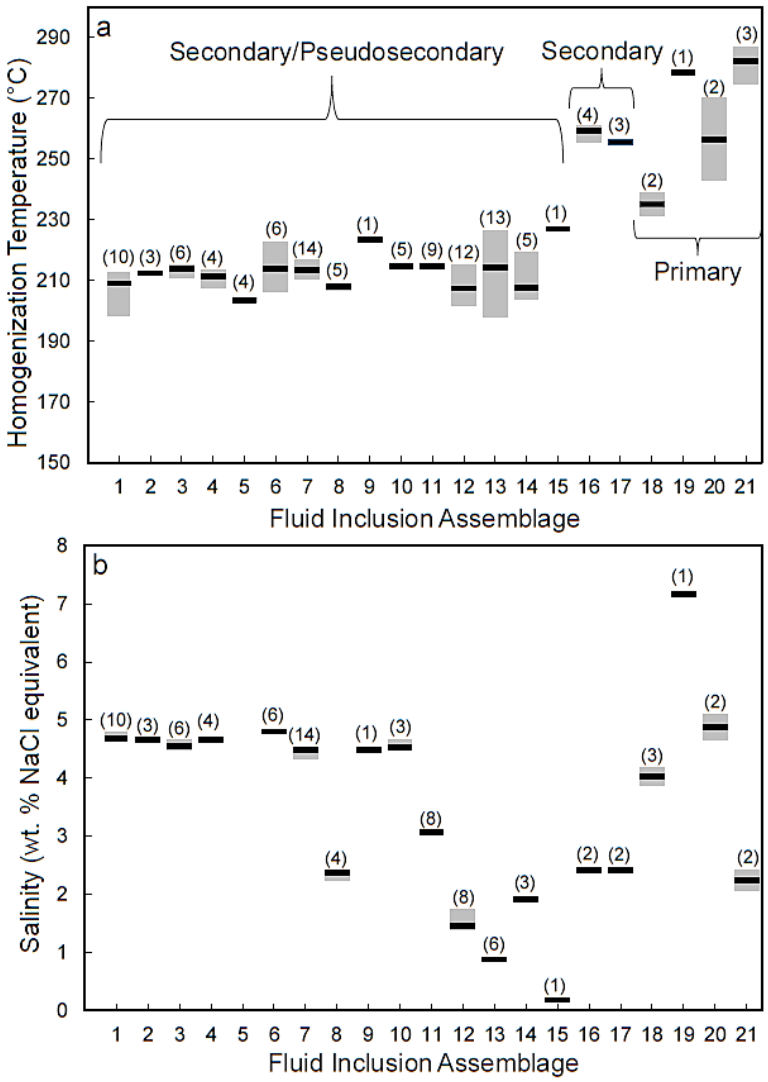

Figure 15: Homogenization temperature (a) and salinity (b) ranges (grey bars) and mean values (black lines) for each FIA. The number of FIs measured for each FIA is shown in parentheses above. The provenance of FIAs is listed as being secondary/psuedosecondary, secondary, or primary. The FIAs 1 to 15 are from stage II sphalerite, whereas the FIAs 16 to 21 are from stage IV sphalerite.

5.0 Discussion

The CZ is a mineralogically and texturally complex ore zone that formed during a protracted paragenesis in an evolving and dynamic hydrothermal system. Integration of data on FIs, breccias, mineralogy, textures and geochemistry are used to generate a formational model for the zone. Furthermore, these data are compared to other studies on the mineralization at the Pirquitas mine and deposits throughout the ATB.

5.1 Fluid Inclusions

The observation of near-critical fluids in quartz-hosted FIs (Fig. 14k, m) may indicate that temperatures were relatively high during the early stages of mineralization and is consistent with a fluid that was exsolved from a magmatic source that cooled slightly. Early vein stages in Bolivian Sn-Ag deposits have been interpreted to have formed at temperatures up to 530 °C and similar temperatures are documented for the initial stages of the San Rafael deposit in Peru (Kelly & Turneaure, 1970; Kontak & Clark, 2002; Wagner, 2009).

The temperatures of the ore fluid during stages II and IV are interpreted using sphalerite-hosted FIs. As noted above, data for V-rich inclusions in stage II sphalerite indicate a flashing system (i.e., trapped in the V-only field; Fig. 16b) at temperatures greater than 320 °C, however, some caution is applied to this temperature estimate. The interpretation that flashing, not boiling occurred during this stage is corroborated by the absence of a residual saline brine as would have been recorded in FIs. In stage IV sphalerite, primary FIAs have Th values between 235 °C and 282 °C with a singular FIA recording heterogeneous entrapment at 282 °C. Thus, temperatures of approximately >320 °C and 280 °C are assigned to stages II and IV, respectively. Boiling is commonly documented in the early vein stages of Bolivian Sn-Ag deposits (Kelly & Turneaure, 1970). Evidence for flashing in the CZ suggests that fluctuations in confining pressure were severe (e.g., Moncada et al., 2012). These pressure fluctuations are interpreted to have occurred by cyclical opening and closing of the hydrothermal system through brecciation and precipitation; this formational model is similar to the “fault valve” model proposed by Sibson et al. (1988).

The primary FIA in stage IV with heterogeneous entrapment provides the best data to determine paleodepth of mineralization. It gave a Th value of ~280 °C and salinity of 4.2 wt. % NaCl equivalent indicating that the trapping pressure was ~65 bar. Assuming a purely hydrostatic

pressure gradient, this equates to ~650 m below paleo-water table. The sample containing these inclusions was collected from ~400 m below the current base of the Cortaderas Valley. Therefore, the top of the paleo-water table is estimated to have been ~250 m above the current erosion surface during stage IV. This depth is consistent with mineralization having formed after or during the late stages of the deposition of the Tiomayo Formation, the top of which having been deposited less than 12 ± 2 Ma (Coira et al., 2004).

The FI data are consistent with a dilute magmatic fluid having been the dominant ore-forming fluid. Salinity data from secondary/pseudosecondary FIAs in stages II sphalerite show a mixing trend between a moderately saline fluid (4.5 to 5.0 wt. % NaCl equivalent) and meteoric water (Fig. 16a). Both of these endmembers yielded Th values between ~200 °C and ~230 °C which is consistent with the mixing of a magmatic fluid with heated meteoric water. The FIAs from stage IV sphalerite have up to 7 wt. % NaCl equivalent which is also consistent with a magmatic origin. The FIAs in stage IV sphalerite may also show a mixing trend with heated meteoric water (Fig. 16a). In Bolivian Sn-Ag deposits, the temperatures and salinities of the ore fluids have been shown to progressively decrease in the late stages of mineralization which has been attributed to dilution by meteoric water (Kelly & Turneaure, 1970).

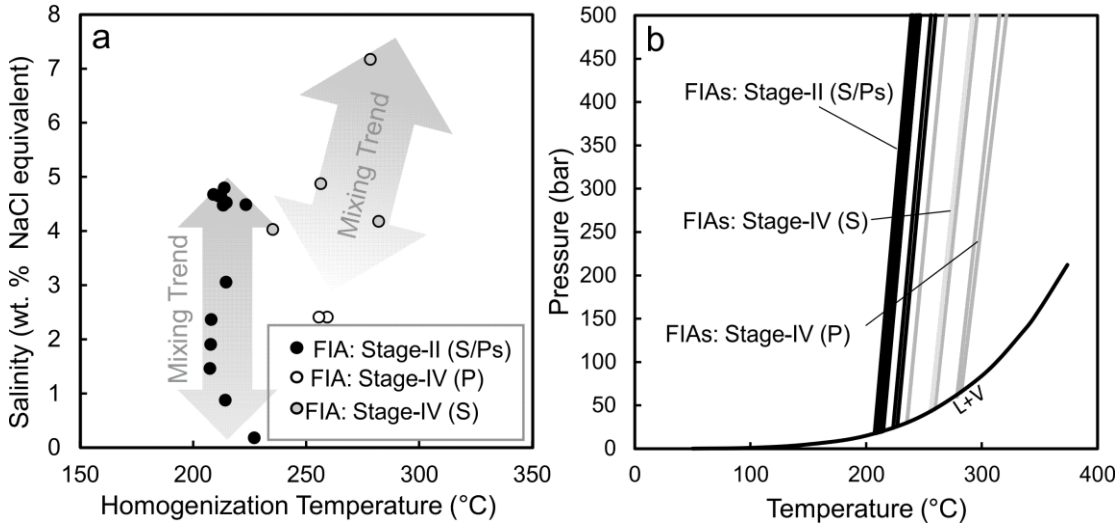

Figure 16*:* Fluid inclusion assemblage (FIA) data and interpretation. (a) Average salinity versus homogenization temperature of each FIA. Secondary or pseudosecondary (S/PS) FIAs in stage II sphalerite show a clear mixing trend between a moderately saline fluid (~4.5 wt. % NaCl equivalent) and pure water. There is a possible second mixing trend recorded by primary (P) and secondary FIAs from stage IV sphalerite. (b) Isochores for each FIA from stage IV and II sphalerite. The boiling curve (i.e., L-V curve) for a 4.5 wt. % NaCl fluid is shown as a curved black line.

5.2 Breccia Bodies

The fault breccias observed in drill core adjacent to the central breccia vein are interpreted to predate the ore-forming system and may have formed by reactivation of Cretaceous faults (e.g., Cladouhos et al., 1994). Fault breccias of this nature have been documented in many ore deposits globally (Sillitoe, 1985). In this case, a pre-existing fault breccia likely acted as a plane of weakness which focussed the dilation required to accommodate the large quantities of mineralized breccia. The fault breccias are not strongly mineralized suggesting that they were relatively impermeable. Idoyaga (1995) demonstrated that various veins in the open pit formed in fault jogs produced by strike-slip displacement. In the CZ, built up fluid pressure could have facilitated the reactivation of the pre-existing fault in a strike-slip manner, which could have produced dilation along bends in the structure.

Crackle, phreatic and pebble-dyke breccias are interpreted to have genetic relationships with the ore-forming system. Crackle breccias, which are common features in many types of hydrothermal systems, form due to changes in fluid pressure (Jébrak, 1997). In the CZ, their formation likely arose due to depressurization after the initial brecciation/dilation of the central structure. Generally, phreatic and pebble-dyke breccias form due to the sudden release of built-up fluid pressure triggered by events including the emplacement of intrusions but also by seismically induced faulting (Sillitoe, 1985). In the CZ, emplacement of new intrusive stocks or rupturing of the outer carapace of a fractionating magma chamber could have released fluids and triggered the explosive emplacement of these breccias bodies at several stages in the paragenesis.

The presence of igneous clasts in phreatic and pebble-dyke breccias could have been caused by two processes: 1) the descent of volcanic rock fragments from overlying Miocene ignimbrite deposits, or 2) the ascent of fine-grained intrusive rock fragments from a buried Miocene intrusion. Here, the latter process is favored. The petrographic observation that quartz in clasts contains secondary FIs with near-critical fluids suggests that these fluids were trapped at relatively high temperatures and pressures, probably below the ore zone. Also, pebble-dyke breccias in the CZ contain mineralization in rounded clasts which are interpreted to have been transported from depth.

The Potosi Breccia North has many characteristics of an intrusion breccia described by Sillitoe (1985). The large breccia body contains igneous clasts that are interpreted to have been derived from below based on near-critical secondary FIs and subvolcanic igneous textures (i.e., porphyritic). It is likely that the Potosi Breccia North is rooted in an intrusion at depth. Furthermore, the matrix which is mostly rock flour, may contain a significant igneous component,

particularly where it is strongly clay- and sericite-altered. Sillitoe (1985) describes similar breccias that often contain igneous components at the Oruro deposit in Bolivia.

5.3 Colloform Textures

Many articles on the growth of colloform sphalerite present evidence that fluid mixing was the dominant process responsible for its formation with the focus of this research having been conducted on sediment-hosted Pb-Zn deposits (e.g., Barrie et al., 2009; Gagnevin et al., 2014). Occurrences of colloform cassiterite, such those in at San Rafael, closely resemble the colloform textures in the CZ and have also been attributed to fluid mixing (e.g., Kontak & Clark, 2002). However, colloform textures are commonly related to boiling in epithermal systems such as those in Mexico (e.g., Moncada et al., 2012). In the CZ, data for primary FIs in colloform sphalerite demonstrate that flashing and boiling were occurring during its formation. Based on this evidence, coupled with general observations on the distribution of the texture, flashing and boiling are interpreted as the processes that formed colloform sphalerite.

Data on the origin of colloform pyrite and marcasite is limited as fluid inclusion studies were not possible for these minerals. Franchini et al. (2015) argue that colloform pyrite and marcasite in the Agua Rica deposit, Catamarca, Argentina, formed due to undercooling that was facilitated by boiling. The colloform pyrite and marcasite in the CZ could have been formed by boiling or flashing in a similar fashion. Alternatively, the fluid mixing that was documented in secondary/pseudosecondary FIs (a) could have produced the undercooling that gave rise to colloform pyrite and marcasite.

5.4 Dendritic Textures

Dendritic-textured sulfide minerals in hydrothermal systems are not well documented in the literature but have been described in association with colloform textures, such as those in

sediment-hosted Pb-Zn deposits (Paradis et al., 1988). Dendritic textures are, however, well documented in silicate systems such as pegmatites (e.g., spodumene; London, 2008) and ultra-mafic rocks (e.g., spinifex; Faure et al., 2006; Welsch et al., 2012) which might provide useful analogs to interpret its origin. For example, in ultra-mafic magmas it is shown that dendritic olivine forms due to undercooling and rapid crystal growth (e.g., Welsch et al., 2012). The spatial association between colloform- and dendritic-textured sphalerite in the CZ suggests that they formed by similar processes (e.g., Fig. 12c). No fluid inclusion data were obtained for dendritic sphalerite due to its fine-grained nature and thus, the process that formed it can only be speculated. Based on the association of dendritic with colloform sphalerite, for which boiling and flashing are the preferred ore forming process, dendritic sphalerite is interpreted to have formed in a similar manner.

5.5 Sulfosalts

With the exception of a minor amount of Ag-bearing galena, sulfosalts are the only minerals that host wt. % levels of Ag in the CZ. Silver-bearing sulfosalts occur in four of the eight paragenetic stages (II, III, VI, and VII). Stage II mineralization hosts Ag as blebby inclusions of proustite within galena. This stage likely only accounts for minor Ag as it is diluted by abundant co-genetic sphalerite and pyrite. Stage III mineralization that consists of Ag-bearing tetrahedrite, pyrargyrite, miargyrite and minor unidentified phases accounts for the majority of Ag where it is present. Stage VI mineralization, which is similar to stage III, is volumetrically minor and thus does not account for significant Ag. Stage VII mineralization, the principal Sn-sulfosalt-bearing stage, likely accounts for a dispersal halo of low-grade Ag mineralization.

The mineral assemblage that composes stage III mineralization is typical for deposits in the southern portion of the ATB, such as Cerro Rico de Potosi, which also has Ag-Sb-bearing

sulfosalts (Turneaure, 1960). This bonanza-grade Ag stage is interpreted to have formed from a boiling or flashing fluid in which sphalerite precipitation was mostly supressed or restricted to other areas. The occurrence of this stage immediately after a brecciation event is consistent with its formation by boiling or flashing.

The mineral assemblage that composes stage VII mineralization differs from those of previous stages in that sulfosalts, not cassiterite, host the majority of Sn. It is also distinct in that it does not appear to have followed immediately after a brecciation event. Its mineralogy resembles that of other zones at the Pirquitas Mine, such as the Oploca Veins with abundant minerals of the pirquitasite-hocartite series, as well as frankeite (Malvicini, 1978; Slater (unpublished data)). The stage is interpreted to have formed at relatively high temperatures during a period of quiescence, possibly while the hydrothermal system was sealed. A sealed system would have caused temperature gradients to rise while the confining pressure supressed boiling.

5.6 Gangue Minerals and Alteration

Although gangue minerals compose only minor components of mineralization at the CZ, they add some important information about the conditions of mineralization. Generally, dickite forms at temperatures below 250 °C in hydrothermal systems (Hedenquist et al., 2000). The documentation of dickite being the dominant clay species, common in stages V and VIII, provides rough upper constraints on temperature for these stages. In Bolivian Sn-Ag deposits, siderite is commonly documented to have formed in the late stages of mineralization as an alteration product of Fe-sulfides such as pyrrhotite (Kelly & Turneaure, 1970). Fluid inclusions studies of siderite in these deposits constrain its formation temperature to between 200 °C to 260 °C (Kelly & Turneaure, 1970). The occurrence of siderite and dickite in stages V and VIII suggest formation temperatures between 200 °C to 250 °C for these stages. These relatively low temperatures indicate

that the system was waning. Hydrous phosphates have been documented in the late stages of Bolivia Sn-Ag deposit formation and are either hypogene or supergene in origin (Kelly & Turneaure, 1970). Goyazite and REE-bearing hydrous phosphates in the CZ are shown to be hypogene due to their intergrowth with minerals such as cassiterite. Their occurrence may signify that the hydrothermal fluids were becoming neutralized with the addition of meteoric water.

5.7 Metal Zoning

Zoned distributions of metals are common in Sn deposits (Turneaure, 1971; Taylor, 1979) and other deposit types such as volcanogenic massive sulfide deposits (Hannington, 2014). In Sn deposits, it is frequently observed that Sn-Cu mineralization gives way to Zn-Pb-Ag mineralization outwards (Turneaure, 1971; Taylor, 1979). In volcanogenic massive sulfide deposits, Cu mineralization gives way to Zn-Pb(-Ag) mineralization outwards (Hannington, 2014). In both cases, the temperature dependence of metal solubility may contribute to the zoned distribution of these metals.

Consistent with the above studies, Ag and Sn are enriched in the core of the SMZ, whereas other peripheral zones are more enriched in Zn(-Pb). The zoned distribution of these metals, on the scale of the mine area is consistent with a telethermal model with the San Miguel Zone having formed at the highest temperature whereas zones such as the CZ formed at lower temperature. Therefore, the CZ may represent the distal lower temperature expression of the larger hydrothermal system that formed ores at the Pirquitas mine.

At the scale of the CZ, it appears that metals do not show a zoned distribution. Silver, Zn, Sn and Pb are concentrated below the 4,200 m level, which could be the result of vertically restricted boiling and flashing. Structures such as the Cortaderas Fault and the hinge of a N-S trending antiform appear to have focused mineralization between them and may also have acted

as conduits for mineralizing fluids. As a general trend, Ag, Zn and Sn all increase in concentration with depth suggesting that mineralization continues below the currently tested depths. The Ag-Zn-rich mineralization in the CZ may give way to Ag-Sn-rich mineralization at greater depths than those tested.

5.8 Ore Zone Classification

The mineral assemblages in hydrothermal ore deposits reflect the prevailing sulfidation state, itself a function of sulfur fugacity and temperature (e.g., Barton and Skinner, 1967; Einaudi et al., 2003). The CZ is the product of a cycling hydrothermal system involving both magmatic and meteoric fluids, whereby the physicochemical characteristics, including sulfidation state, were fluctuating. For the purposes of classifying the ore zone, the temperature of stage II as determined by microthermometry is used in conjunction with mineralogy (Fig. 16). The exclusive appearance of Ag in sulfosalts shows that sulfur fugacity and temperature were sufficiently high as to inhibit the formation of native Ag. Furthermore, the presence of tetrahedrite and absence of enargite and famatinite shows that sulfidation state was below this reaction boundary. These constraints combined with the temperature estimate show that the ore zone formed by an intermediate-sulfidation system.

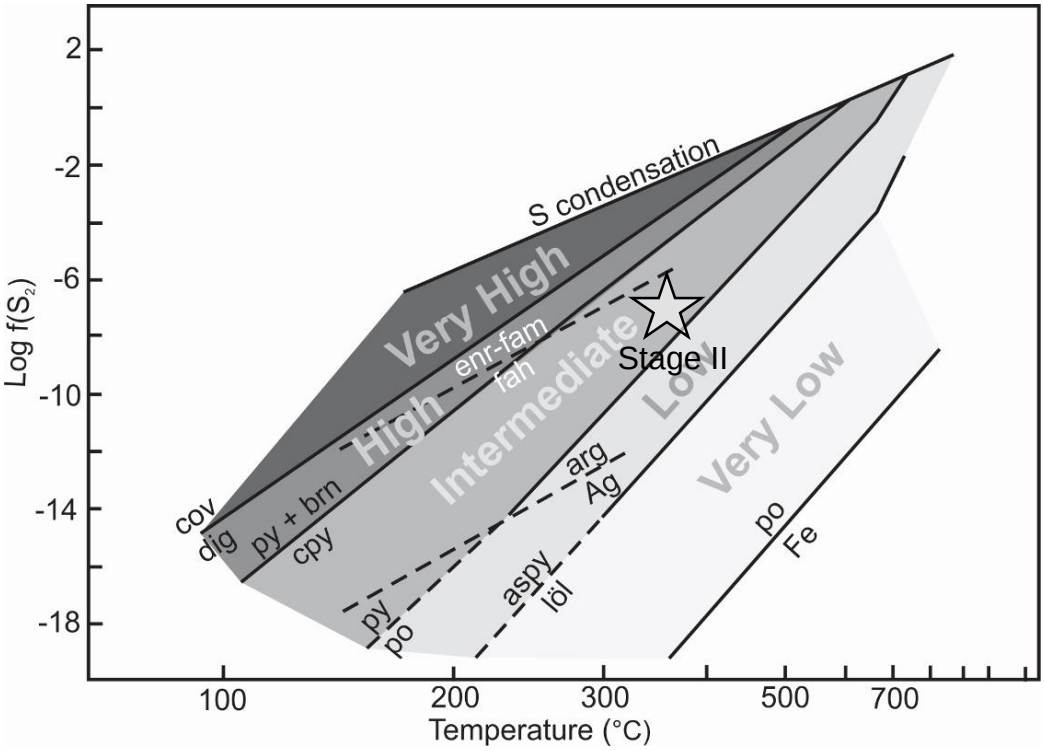

Figure 17: Epithermal classification diagram based on sulfidation state. Here temperature is plotted against sulfur fugacity and the stability fields of some relevant minerals are shown. (modified from Einaudi et al., 2003). The mineralogy and temperature estimated for stages II, the main Zn stage, is used to constrain the sulfidation state. py – pyrite, brn – bournite, cpy – chalcopyrite, cov – covellite, dig – digenite, brn – bornite, löl – löllingite, arg – argentite, fah – fahlore, enr-fam – enargite-famatinite.

5.9 Genetic Model

The mineralization in the CZ resulted from the episodic flashing and boiling of a dominantly magmatic fluid during transient fluctuations in confining pressure. This model is schematically illustrated in Figure 18 for the first two stages of the paragenesis. The origin of Ag and other elements is proposed to have been the magmatic fluids themselves, an interpretation commonly accepted for deposits in the ATB (Kelly & Turneaure, 1970).

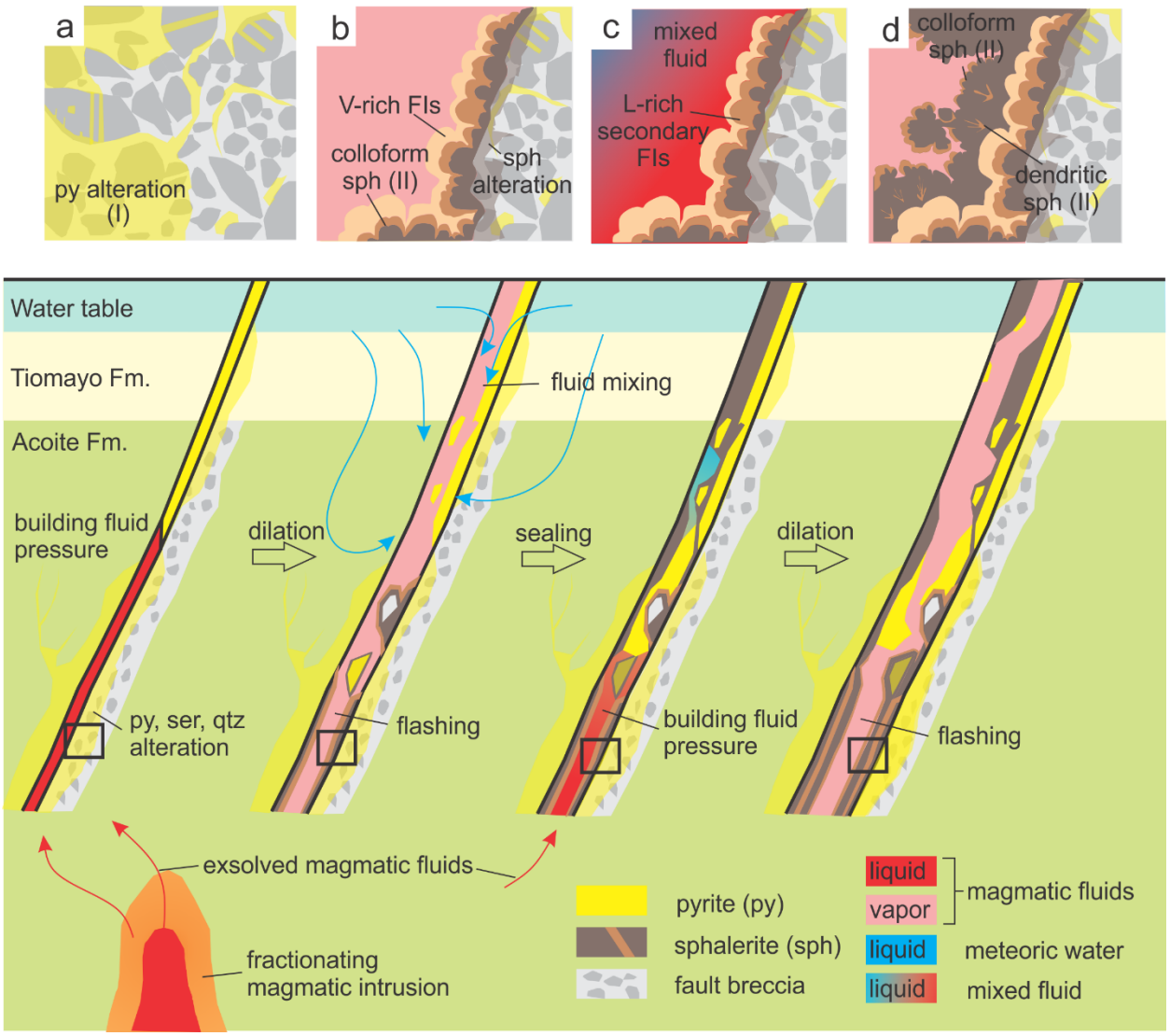

Figure 18: Schematic model illustrating the early stages of mineralization in the CZ. (a) A pre-existing fault breccia is reactivated due to the build-up of magmatic fluid pressure derived from an inferred intrusion at dept. The released reduced and acidic fluids penetrate the wall rocks and locally replace them with pyrite, sericite and quartz. Early mineralization creates a seal allowing for fluid pressure to rise. (b) The system dilates and brecciates causing the magmatic fluids to flash to steam. In a vertically restricted zone, undercooling causes the precipitation of colloform and dendritic sphalerite. Low-density primary FIs are trapped in the sphalerite. The dilated structure acts as a conduit for descending meteoric water. The meteoric water mixes with magmatic fluids resulting in some mineralization that seals the structure. (c) Fluid pressure rises in a sealed system. Secondary/pseudosecondary FIs with moderate density are trapped in the sphalerite. (d) Again, the system dilates and brecciates causing the mixed dominantly magmatic fluid to flash to steam. In a vertically restricted zone, undercooling causes the precipitation of dendritic and colloform sphalerite.

Initially, a pre-existing, possibly Cretaceous ESE-striking fault below what is now the Cortaderas Valley was reactivated by strike-slip movement having been aided by fluid pressure generated by an intrusion. The rupture of the fault led to instantaneous depressurization causing the magmatic fluid to flash to steam or boil depending on the amount of confining pressure. The resulting undercooling gave rise to colloform and dendritic textures. Dilation along the structure also allowed the downward flow of meteoric waters which were passively heated and then mixed with magmatic fluids. The formation of sulfide-rich mineralization as the result of flashing, boiling and later mixing sealed the system allowing temperatures and pressures to rise. The fluid pressure would have eventually exceeded the tensile strength of the sulfide seal and resulted in more dilation, brecciation and mineralization. This cycle of dilation and sealing occurred many times during the protracted paragenesis in a similar manner to the "fault valve" model of Sibson et al. (1988). During a prolonged state of quiescence with a sealed system, temperature gradients were allowed to rise which overprinted the system with Ag-Sn-sulfosalt mineralization, interpreted to have formed at relatively high temperatures.

6.0 Conclusions

The CZ was the product of an intermediate sulfidation epithermal system that developed over eight paragenetic stages including an initial rock preparation stage (I), several ore stages (II-VII) with intermineral brecciation and a waning stage (VIII). The system episodically depressurized following dilation and brecciation that resulted in flashing and boiling. Fluid inclusions provide evidence that flashing and boiling produced undercooling and the deposition colloform and dendritic sulfide mineralization as well as bonanza grade Ag mineralization. Stage VII mineralization, characterized by Ag-Sn-bearing sulfosalts formed during a quiescent period while the system was sealed and temperature gradients were higher. The alteration is hypogene in

origin and occurred during the late stages of mineralization during the waning of the hydrothermal system. The magmatic fluids, heat and metals are all likely derived from an inferred magmatic intrusion at depth with several breccia bodies at the mine being rooted in this inferred intrusion. The magmatic fluids mixed with heated meteoric waters while the system was open that may have contributed to some mineralization and alteration. The zoned distribution of metals indicates that the CZ is the distal lower temperature expression of the larger hydrothermal system that formed ores at the Pirquitas mine. A summary of the ore zone characteristics and evidence for them is provided in Table 4.

Table 4. Summary of the characteristics ore zone characteristics. The evidence used to make the interpretations are indicated.

Ore Zone Characteristics		Evidence
hydrothermal fluids	magmatic (4.5 to 7.0 wt. % NaCl equivalent)	fluid inclusions
	meteoric (No salinity)	fluid inclusions
temperature	rock preparation and pyritization: > 400 °C	fluid inclusions
	principal Zn stage: >320 °C	fluid inclusions
	waning stages: 200 °C to 250 °C	mineralogy (dickite and marcasite)
		fluid inclusions (secondary)
ore-forming processes	flashing, boiling, fluid mixing	fluid inclusions, textures
post-ore erosion	~250 m (assuming hydrostatic gradient)	fluid inclusions
mineralization	pyrite, marcasite, sphalerite, arsenopyrite, cassiterite, quartz, clays (dickite), galena, siderite, sulfosalts	petrography, SEM-EDS, EMPA, powder XRD
alteration	silica, clay (dickite ± kaolinite), sericite, chlorite, goyazite, REE-bearing hydrous phosphates	petrography, SEM-EDS, powder XRD
textures	massive, colloform, dendritic, cockade	petrography
breccias	fault, crackle, phreatic, pebble-dykes	petrography

intrusion	unidentified. Potosi Breccia North may grade downwards into an intrusion	porphyritic clasts
age	< 15.7 ± 0.6 Ma possibly < 12 ± 2 Ma	cross-cutting relationship stratigraphic reconstruction

References

Allmendinger, R. W., Jordan, T. E., Kay, S. M., Isacks, B. L., 1997, The evolution of the Altiplano-Puna plateau of the central Andes: Annual Review of Earth and Planetary Sciences, v. 25, p. 139-174.

Bahlburg, H., 1990, The Ordovician Puna basin in the Puna in the NW Argentina and N Chile: Geodynamic evolution from back-arc to foreland basin: Geotektonische Forschungen, v. 75, p. 1-107.

Barrie, C. D., Boyce, A. J., Boyle, A. P., Williams, P. J., Blake, K., Wilkinson, J. J., Lowther, M., McDermott, P., and Prior, D. J., 2009, On the growth of colloform textures: a case study of sphalerite from the Galmoy ore body, Ireland: Journal of the Geological Society, v. 166, p. 563-582.

Barton Jr., P. B., and Skinner, B. J., 1967, Sulfide mineral stabilities, in H. L. Barnes ed.: Geochemistry of hydrothermal ore deposits, p. 236-333.

Board, W. S., Kennedy, R. B., Yeomans, T. J., 2011, NI 43-101 Technical Report on the Pirquitasmine, Jujuy, Argentina. p. 1-220.

Bodnar, R. J., and Vityk, M. O., 1994, Interpretation of microthermometric data for H_2O-NaCl fluid inclusions, in De Vivo B., and Frezzotti, M. L., eds., Fluid Inclusions in Minerals, Methods and Applications, Blacksburg, Virginia Tech, p. 117-130.

Bodnar, R. J., 2003, Introduction to fluid inclusions, in Samson, I., Anderson, A., and Marshall, D. eds, fluid inclusions – analysis and interpretation: Mineralogical Association of Canada Short Course Series, v. 32, p. 1-8.

Brodtkorb, M. K., 2009, Precious metal tellurides and other Te-bearing minerals in different paragenesis of Argentina. A review: Revista de la Asociación Argentina, v. 64, p. 365-372.

Caffe, P. J., Soler, M. M., Coira, B. L., Onoe, A. T., and Cordani, U. G., 2008, The Granada ignimbrite: A compound pyroclastic unit and its relationship with Upper Miocene caldera volcanism in the northern Puna: Journal of South American Earth Sciences, v. 25, p. 464-484.

Chutas, N. I., and Sack, R. O., 2004, Ore genesis at la Colorado Ag-Zn-Pb deposit in Zacatecas, Mexico: Mineralogical Magazine, v. 68, p. 923-937.

Cladouhos, T. T., Allmendinger, R. W., Coira, B., and Farrar, E., 1994, Late Cenezoic deformation in the Central Andes: Fault kinematics from the northern Puna, northwestern Argentina and southwestern Bolivia: Journal of South American Earth Sciences, v. 7, p. 209-228.

Clark, A. H., Farrar, E., Caelles, J. C., Haynes, S. J., Lortie, R. B., McBride, S. L., Quirt, G. S., Robertson, R., C., R., and Zentilli, M., 1976, Longitudinal variations in the metallogenic evolution of the central Andes: A progress report: Geological Association of Canada Special Paper, v. 14, p. 23-58.

Coira, B., 1979, Descripción geológica de la hoja 3c Abra Pampa, provincia de Jujuy: Boletín del Servicio Geológico Nacional, v. 170, p. 1-90.

Coira, B., Caffe, P., Ramírez, A., Chayle, W., Díaz, A., Rosas, S., Pérez, A., Pérez, B., Orozco, O., and Martínez, M., 2004, Programa nacional de cartas geológicas de la República Argentina: Hojas Geológica 2366-I/2166-III: Institutue de Geológía y Recursos Minerales, p. 1-125.

Cunningham, C. G., Zartman, R. E., McKee, E. H., Rye, R. O., Naeser, C. W., Sanjinés O. V., Erickson, G. E., and Tavera, V. F., 1996, The age and thermal history of Cerro Rico de Potosi, Bolivia: Mineralium Deposita, v. 3, p. 374-385.

Einaudi, M. T., Hedenquist, J. W., and Inan, E. E., 2003, Sulfidation state of fluids in active and extinct hydrothermal systems: transitions from porphyry to epithermal environments: Society of Economic Geologists Special Publication, v. 10, p. 285-313.

Faure, F., Arndt, N., and Libourel, G., Formation of spinifex texture in Komatiites: an experimental study: Journal of Petrology, v. 47, p. 1591-1610.

Franchini, M., McFarlane, C., Maydagán, L., Reich, M., Lentz, D. R., Meinert, L., Bouhier, V., 2015, Trace metals in pyrite and marcasite from the Agua Rica porphyry-high sulfidation epithermal deposit, Catamarca, Argentina: Textural features and metal zoning at the porphyry to epithermal transition: Ore Geology Reviews, v. 66, p. 366-387.

Gagnevin, D., Menuge, J. F., Kronz, A., Barrie, C., and Boyce, A. J., 2014, Minor elements in layered sphalerite as a record of fluid origin, mixing, and crystallization in the Navan Zn-Pb ore deposit, Ireland: Economic Geology, v. 109, p. 1513-1528.

Gamarra-Urrunaga, J. E., Castroviejo, R., and Bernhardt, H.J., 2013, Preliminary mineralogy and ore petrology of the intermediate-sulfidation Pallancata deposit, Ayacucho, Peru: Canadian Mineralogist, v. 51, p. 67-91.

Goldstein, R. H., and Reynolds, T. J., 1994, Systematics of fluid inclusions in diagenetic minerals: Society for Sedimentary Geology Short Course 31, p. 1-199.

Hannington, M. D., 2014, Volcanogenic Massive Sulfide Deposits: Treatise on Geochemistry 2nd ed., p. 463-487.

Harrington, H. J., 1957, Ordovician formations of Argentina, in Harrington, H. J., and Leanza, A. F., eds., Ordovician trilobites of Argentina, Kansas: University of Kansas Paleontological Contributions: Special Publication 1, University of Kansas Press, p. 1-59.

Hawkins, C., Angheluta, L., Hammer, Ø., and Jamtveit, B., 2013, Precipitation dendrites in channel flow: EPL, v. 102, p. 6.

Hedenquist, J. W., Arribas, A. J., and Gonzales-Urien, E., 2000, Exploration for epithermal gold deposits: Reviews in Economic Geology, v. 13, p. 245-277.

Heinrich, C. A., 1990, The chemistry of hydrothermal tin(-tungsten) ore deposition. Economic Geology, v. 85, p. 457-481.

Idoyaga, M. G., 1995, Caracterización tectónica y metalogénica de los depósitos estanníferos argentinos: Unpublished Ph.D. thesis, Buenos Aires, Argentina, Universidad de Buenos Aires, p. 1-170.

Ishihara, S., 1981, The granitoid series and mineralization. Economic Geology, 75th Anniversary, p. 458-484.

Johan, Z., and Picot, P., 1982, La Pirquitasite, Ag_2ZnSnS_4, un nouveau membre du groupe de la stannite: Bull. Minéral, v. 105, p. 229-235.

Kay, S. M., and Mpodozis, C., 2001, Central Andean ore deposits linked to evolving shallow subduction systems and thickening crust: GSA Today, v. 11, p. 4-9.

Kelly, W. C., and Turneaure, F. S., 1970, Mineralogy, paragenesis and geothermometry of the tin and tungsten deposits of the easter Andes, Bolivia: Economic Geology, v. 65, p. 609-680.

Kittl, E., 1972, Yacimientos minerales y su formación: Revista Minera. Geología y Mineralogía, v. 31, p. 1-241.

Kontak, D. J., and Clark, A. H., 2002, Genesis of the giant, bonanza San Rafael lode tin deposit, Peru: Origin and significance of pervasive alteration: Economic Geology, v. 97, p. 1741-1777.

Lehmann, B., Ishihara, S., Michel, H., Miller, J., Rapela, C. W., Sanchez, A., Tiltl, M., and Winkelmann, L., 1990, The Bolivian Tin Province and Regional Tin Distribution in the central Andes: A reassessment. Economic Geology, v. 85, p. 1044-1058.

Malvicini, L., 1978, Las vetas de estaño y plata de Mina Pirquitas (Pircas) provencia de Jujuy, República Argentina: Revista de la Asociación Argentina de Mineralogía, Petrología y Sedimentología, v. 9, p. 1-25.

Marrett, R. A., Allmendinger, R. W., Alonso, R. N., and Drake, R. E., 1994, Late Cenozoic tectonic evolution of the Puna Plateau and adjacent foreland, northwestern Argentine Andes: Journal of South American Earth Sciences, v. 7, p. 179-207.

Marshall, D. D., Diamond, L. W., and Skippen, G. B., 1993, Silver transport and deposition at Cobalt, Ontario, Canada: Fluid inclusion evidence. Economic Geology, v. 88, p. 837-854.

Mlynarczyk, M. S., and William-Jones, A. E., 2005, The role of collisional tectonics in the metallogeny of the Central Andean Tin Belt; Earth and planetary science letters,v. 240, p. 656-667.

Moncada, D., Mutchler, S., Nieto, A., Reynold, T. J., Rimstidt, J. D., and Bodnar, R. J., 2012, Mineral textures and fluid inclusion petrography of the epithermal Ag-Au deposits at

Guanajuato, Mexico: Application to exploration; Journal of Geochemical Exploration, v. 114, p. 20-35.

Caffe, P. J., Trumbull, R. B., Coira, B. L., Rolf, L. Romer, 2002, Petrogenesis of early Neogene magmatism I the northern Puna; Implications for magma genesis and crustal processes in the central Andean Plateau: Journal of Petrography, v. 43, p. 907-942.

Paradis, S., Jonasson, I. R., Le Cheminant, G. M., and Watkinson, D. H., 1988, Two zinc-rich chimneys from the plume site, southern Juan de Fuca Ridge: Canadian Mineralogist, v. 26, p. 637-654.

Paar, W. H., Brodtkorb, M. K., Sureda, R. J., Topa. D, 2001, Mineralogía, y quimismo de sulfuros y sulfosales de estaño y plomo en las vetas de Mina Pirquitas, Jujuy, Argentina (22°41'S66°28'W): Revista geológica de Chile, v. 28, p. 259-268.

Petersen, U., 1970, Metallogenic provinces in South America: Geologische Rundschau, v. 59, p. 834-897.

Reed, M. H., and Palandri, J., 2006, Sulfide mineral precipitation from hydrothermal fluids: Reviews in Mineralogy and Geochemistry, v. 61, p. 609-631.

Rosas, L. V., and Avila, J. C., 2013, Desarrollo minero de Pirquitas, provincia de Jujuy: Serie Correlación Geológica, v. 29, p. 51-62.

Sack, R. O., 2005, Internally consistent database for sulfides and sulfosalts in the system Ag_2S-Cu_2S-ZnS-FeS-Sb_2S_3-As_2S_3: Update: Geochimica et Cosmochimica Acta, v. 69, p. 1157-1164.

Sack, R. O., and Ebel, D. S., 2006, Thermochemistry of sulfide mineral solutions: Reviews in Mineralogy & Geochemistry, v. 61, p. 265-364.

Sack, R. O., and Lichtner, P. C., 2009, Constraining compositions of hydrothermal fluids in equilibrium with polymetallic ore-forming sulfide assemblages: Economic Geology, v. 104, p. 1249-1264.

Sack, R. O., Lynch, J. V., and Foit, Jr., F., 2003, Fahlore as a petrogenetic indicator: Keno Hill Ag-Pb-Sn district, Yukon, Canada. Mineralogical Magazine, v. 67, p. 1023-1038.

Schneider, H. J., and Lehmann, B., 1977, Contribution to a new genetic concept on the Bolivian tin province, in Klemm, D. D., and Schneider, H. J., eds, Time- and strata-bound ore deposits, 1st ed.: Springer-Verlag, Berlin, p. 153-168.

Schuiling, R. D., 1967, Tin belts on the continents around the Atlantic Ocean: Economic Geology, v. 62. p. 540-550.

Schumer, B. N., Downs, R. T., Domanik, K. J., Andrade, M. B., and Origlieri, M. J., 2013, Pirquitasite, Ag_2ZnSnS_4: Acta Crystallographica Section E, v. 69, i8-i9.

Sibson, R. H., Robert, F., and Poulsen, K. H., 1988, High-angle reverse faults, fluid-pressure cycling, and mesothermal gold-quartz deposits: Geology, v. 16, p. 551-555.

Sillitoe, R. H., 1972, Relation of metal provinces in western America to subduction of oceanic lithosphere: Geological Society of America, v. 83, p. 813-818.

Sillitoe, R. H., 1985, Ore-related Breccias in volcanoplutonic arcs: Economic Geology, v. 80, p. 1467-1514.

Sillitoe, R. H., 2003, Iron oxide-copper-gold deposits: an Andean view: Mineralium Deposita, v. 38, p. 787-812.

Sillitoe, R. H., 2010, Porphyry Copper Systems: Economic Geology, v. 105, p. 3-41.

Sillitoe, R. H., Halls, C., and Grant, J. N., 1975, Porphyry tin deposits in Bolivia: Economic Geology, v. 70, p. 913-927.

Sillitoe, R. H., and Perello, J., 2005, Andean copper province; tectonomagmatic settings, deposit types, metallogeny, exploration and discovery: Economic Geology, 100th anniversary volume, p. 845-890.

Simmons, S. F., White, N. C., and John, D. A., 2005, Geological characteristics of epithermal precious and base metal deposits: Economic Geology, 100th Aniversary volume, p. 485-522.

Slater, E.T., 2016, The origin of Ag-Zn-Sn mineralization in the Cortaderas Deposit, Pirquitas Mine, NW Argentina: Unpublished M.Sc. thesis, Sudbury, Canada, Laurentian University

Soler, M. M., Caffe, P. J., Coira, B. L., Onoe, A. T., and Kay, M. S., 2007, Geology of the Vilma caldera: A new interpretation of a large-scale explosive event in the Central Andean Plateau during the Upper Miocene: Journal of Volcanology and Geothermal Research, v. 164, p. 27-53.

Taylor, R. G., 1979, Geology of tin deposits: Developments in Economic Geology, v. 11, p. 543.

Tămas, C. G., and Milesi, J.-P., 2002, Hydrovolcanic breccia pipe structures - general features and genetic criteria: Studia Universitatis Babes-Bolyai, Geologia, v. XLVII, p. 127-147.

Turneaure, F. S., 1960a, A comparative study of major ore deposits of central Bolivia. Part I: Economic Geology, v. 55, p. 217-254.

Turneaure, F. S., 1960b, A comparative study of major ore deposits of central Bolivia. Part II: Economic Geology, v. 55, p. 574-606.

Turneaure, F. S., 1971, The Bolivian tin-silver province: Economic Geology, v. 55, p. 215-225.

Turner, J. C., 1964a, Descripción geológia de la hoja 2b la Quiaca (provincia de Jujuy): Boletín del Instituto Nacional de Geología y Minería, Boletín 104, p. 1-83.

Turner, J. C., 1964b, Descripción geológica de la Hoja 2c Santa Victoria (provincias de Salta y Jujuy): Boletín del instituto Nacional de Geología y Minería, Boletín 104, p. 1-109.

Turner, J. C., 1978, Descripción geológica de las hojas 1a y b, Santa Catalina y 2a, San Juan de Oro (provincia de Jujuy): Buletín del Servicio Geológico Nacional, Boletín 156-157, p. 1-56.

Turner, J. C. ,1982, Descripción geológica de la hoja 3b, Mina Pirquitas, Jujuy. Servicio Geológico Nacional. Secretaría de Industria y Minería, Boletín 187, p. 1-56.

Turner, J. C., and Mendez, V., 1979, Puna: Segundo simposio de geologia regional argentina, Córdoba, Academia Nacional de Ciencias, p. 13-56.

Wagner, T., Mlynarczyk, M. S., William-Jones, A. E., and Boyce, A. J., 2009, Stable isotope constraints on ore formation at the San Rafael tin-copper deposit, Southeast Peru: Economic Geology, v. 104, p. 223-248.

Zentilli, M., Pasava, J., and Graves, M. C., 1995, Possible roles of organic carbon in the control and genesis of tin deposits, in Pašava, J., Køíbek, B. and Žák, K. eds., Mineral deposits: from their origin to their environmental impact, Extended Abstracts. Third Biennial SGA Meeting, Prague, A.A. Balkema/Rotterdam, p. 825-828.

Chapter 2:

Ore Textures and Sulfide-Mineral Chemistry of the Cortaderas Zone, Pirquitas Mine, NW Argentina: An Example of Miocene-Age Epithermal Mineralization in the Andean Tin Belt

E.T. Slater, A.M. McDonald, D.J. Kontak

Laurentian University, Department of Earth Sciences and Mineral Exploration Research Centre,

Sudbury ON.

Abstract

Ore samples from the Cortaderas Zone (CZ) at the Pirquitas mine, Jujuy, Argentina were studied using optical petrographic techniques, SEM-EDS, LA-ICP-MS and EMPA in order to: (1) characterize the major-, minor- and trace-element compositions of colour-banded sphalerite and concentrically zoned pyrite; (2) interpret the significance of sulfosalt textures and assemblages; and (3) estimate the temperature of Ag mineralization by sulfosalt geothermometry.

Sphalerite of various paragenetic stages occurs with colloform, banded and massive textures and has broad compositional variations between and within stages. Colloform sphalerite from stages II and IV has rhythmic colour-banding whereby each layer progresses from dark brown to tan sphalerite. The dark brown sphalerite, interpreted to have formed from metal-rich magmatic-dominated hydrothermal fluids in an open system, has elevated levels of Ag, As, Cu, Fe, Ge and Mn. The tan sphalerite, which may have formed in a sealed system, has elevated Cd and In. Due to the incompatibility of Cd and In in sphalerite, the elements may have become enriched in the ore fluid due to fractionation. Sphalerite from stage III, the most Ag-rich stage, has no colour-banding but is enriched in Ag, As, Cd, Cu, Fe, In and Sn relative to other stages. In all of the sphalerites, Ag, As, Cu and Sn likely occur principally as micro-inclusions of sulfosalts and sulfides whereas the Fe, Cd and In have likely substituted for Zn in the sphalerite structure. Pyrite grains from stage V are compositionally zoned with near endmember subhedral cores that are overgrown by at least four concentric overgrowths, the analyses for three of which showed elevated levels of Ag, As, Au, Cu, Co, Ni, Sb, Pb and Bi. Three sets of elements appear spatially related in the pyrite: (1) As-Cu; (2) Ag-Sb-Pb; and (3) Au-Co-Ni(-Bi). Arsenic is likely bound in the structure of pyrite by substitution for S. Copper may also be structurally bound in pyrite, however, some is likely hosted in mineral inclusions. Silver, Sb and Pb likely occur as sulfosalt ±

galena inclusions based on erratic LA-ICP-MS count rates. Likewise, Au, Co, Ni and possibly Bi likely occur as mineral inclusions. Cubic near endmember growth zones in the pyrite grains are interpreted to represent periods of quiescence with slow crystal growth, likely in a closed system. Rounded pyrite growth zones, which contain elevated levels of minor and trace elements, likely represent periods of boiling or fluid mixing which facilitated rapid crystal growth, likely in an open system.

The following sulfosalt assemblages have been documented: (1) pavonite + galena; (2) proustite + galena; (3) boulangerite + jordanite + galena; (4) Ag-bearing tetrahedrite + miargyrite + pyrargyrite + sphalerite ± kesterite ± Ag-Sb-Pb-S phase; (5) pirquitasite + stannite; and (Te-bearing) canfieldite + galena. Some sulfosalt textures, including blebby inclusions and intergrowths are interpreted as having formed by their unmixing from precursor minerals during progressive cooling. High-temperature galena was likely an important precursor mineral to some of the observed sulfosalts. The composition of Ag-bearing tetrahedrite from stages III and VII suggests that they equilibrated at 245 °C ± 15 °C and 270 °C ± 10 °C, respectively. These temperatures may provide minimum temperatures constraints for Ag mineralization.

Introduction

The Pirquitas mine located in Jujuy, Argentina contains significant hydrothermal Ag-Zn-Sn-Pb mineralization representing the southern limit of the metallogenic province known as the Andean Tin Belt (ATB). The area has had a long history of mining activity following its discovery in 1930 (Rosas & Avila 2013). Despite being a long-standing mining camp and being the most southern large primary Sn occurrence in the Andes, little published work exists on its geology and mineralization (e.g., Malvicini 1978, Idoyaga 1992) with much of the research having been focused on documenting the various rare mineral species found there (e.g., Johan & Picot 1982, Paar et al. 2000, Paar et al., 2001). Commencing in 2009 and continuing presently, Ag and Zn are being mined by open-pit methods by Silver Standard Resources Inc. Approximately 500 m north of the currently active open pit is the Cortaderas Zone (CZ) that contains a new, recently discovered (2010) sulfide-rich breccia vein known as the Cortaderas Breccia. As part of a broader study characterizing the CZ (Slater *et al.* in prep.), this contribution documents the sulfide chemistry, sulfosalt assemblages and ore textures.

The mineral paragenesis and a formational model for the CZ were proposed by Slater et al. (in prep), but that study generated many questions regarding the significance of certain ore textures and compositional variations in sulfides. They argue that the CZ developed in a dynamic hydrothermal system with fluctuating P-T-X fluid conditions. Data from fluid-inclusions analyses are used to suggest that processes including flashing (conversion of liquid water to vapour: Moncada *et al.* 2012) and boiling (coexisting low and high density fluids) were responsible for the observed mineralization (Slater *et al.* in prep). The dynamic nature of the ore system may be recorded on the small-scale in the rhythmic colour-banding within colloform sphalerite and the occurrence of concentric growth zones in pyrite. Through LA-ICP-MS studies, the compositional

variations in these sulfides were quantified and used to develop a record of fluid conditions on a scale much finer than that determined by Slater *et al.* (in prep.). The new record of fluid conditions is integrated into the previously developed formational model to create a more complete understanding of the formation of the CZ.

In several of the interpreted ore-forming paragenetic stages at CZ, various sulfosalts, galena and sphalerite occur as blebby inclusions within one another or as convoluted intergrowths. These textures may represent primary intergrowths of minerals in assemblages or they may have formed by the breakdown or unmixing of precursor minerals. Through petrographic and SEM-EDS studies as well as exploratory heating experiments, the origin these textures are discussed, these having implications to the primary mineralogy and their subsequent modification. New EMPA data are presented, these being used to generate sulfosalt chemistry and thermometric data that constrain the temperature of either the emplacement or breakdown/umixing of the primary Ag minerals. Based on this research, insights into the fundamental processes which control ore deposition and modification in epithermal deposits are provided which may then be applied to the entire ATB and other mineral belts.

Geological Setting

The ATB is an ~900 km-long, trench-parallel, metallogenic province containing Sn-bearing polymetallic, epi-mesothermal ore-deposits that span from southern Peru to northwestern Argentina. It represents one of the world's most important Sn resources, as well as being an important source of many other metals such as Ag, Zn, W, Bi, Pb and Sb (Kelly & Turner 1970, Sillitoe 1975). The Sn mineralization at the Pirquitas mine, wherein the CZ is located, defines the southern extent of this richly mineralized metallogenic province.

The Pirquitas mine is located in the physiographic region known as the Puna plateau in Jujuy province, northwestern Argentina. The geology of the Puna plateau has been well-summarized in previous studies (*cf.* Coira *et al*., 2004) and a more thorough summary of the geological setting of the Pirqutias mine is provided in Slater *et al*. (in prep.). The oldest rock exposures in the area are Ordovician metaturbidites of the Acoite Formation that were tightly folded and metamorphosed during a late-Ordovician orogeny (e.g., Bahlburg, 1990). Younger foreland basins that developed were infilled by sedimentary and volcanic deposits, now being represented by units such as the mid-Miocene Tiomayo Formation (Coira et al., 2004). The eruption of the Cerro Grenada II ignimbrite at 9.8 Ma marked the onset of caldera-type volcanism in the region (Caffe et al., 2008). This magmatic flare-up may coincide with the emplacement of the inferred progenitor intrusion which gave rise to mineralization at the Pirquitas mine.

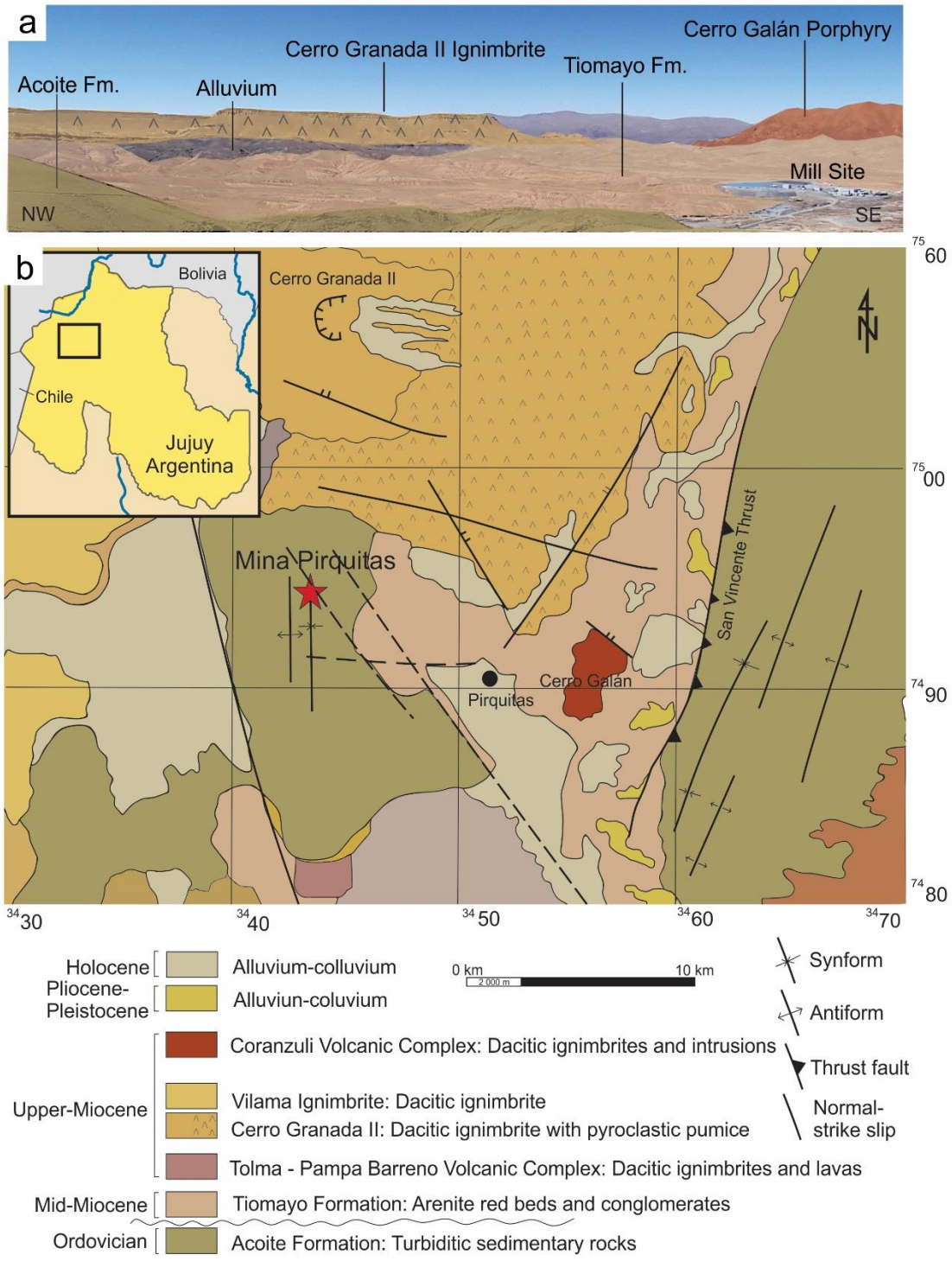

Figure 1: The geological setting of the Pirquitas mine. (a) Photograph taken from the eastern edge of the uplifted block of the Acoite Formation looking ENE. (b) Geological map of the area modified from Coira et al. (2004). The inset image shows the location in the province of Jujuy in NW Argentina. The location of the Pirquitas mine ('Mina Pirquitas') is indicated with the red star.

Mine Geology and Mineralization

The Ag-Zn-Sn-Pb mineralization at the Pirquitas mine occurs in several zones that contain veins and breccia bodies in an uplifted block of the Acoite Formation (Fig. 1). Locally, the mineralization is also found in the basal remnants of the Tiomayo Formation. The Cortaderas Breccia, a steeply dipping vein that is locally over 20 m wide and surrounded by subordinate veins and crackle breccias, is an important host to the Ag-Zn-Sn-Pb mineralization (Fig. 2). The mineralized breccia may have been accommodated by episodic dilation along a fault-jog structure. Movement along the fault is interpreted to have been facilitated by the interplay of hydrothermal fluid pressure and regional tectonic forces (Slater *et al.* in prep.).

Mineralization developed during a protracted paragenesis consisting of at least eight stages including a rock-preparation stage, six ore stages with syn- and inter-mineral brecciation and a waning stage (Fig. 3: Slater *et al*. in prep.). As the paragenesis of the mineralization is a focus of this study, the characteristics of each stage are described in some detail. The mineralization is considered to reflect a telescoped system with the late ingress of a higher-T fluid which was responsible for Sn-Ag mineralization. Stage I represents the initiation of the hydrothermal system and is characterized by pyritization of the wall rocks accompanied by disseminated and stockwork-hosted quartz and sericite alteration. Stage II, the principal stage of Zn mineralization, is accompanied by limited Ag-mineralization, mainly as proustite. It consists of mostly banded, colloform and massive sphalerite, along with minor amounts of arsenopyrite and galena, the latter with inclusions of proustite. Stage III, the principal stage of Ag mineralization, is characterized by dark-grey banding, the bands containing abundant sulfosalts including Ag-bearing tetrahedrite, pyrargyrite, miargyrite, minor amounts of kesterite and various unidentified Ag-Bi-Sb-Pb-S minerals. Stage IV is recognized as being composed of over 95 modal percent banded to colloform

sphalerite that encrusts mineralization of stage III. Stage V consists of massive sulfide mineralization composed of pyrite, marcasite, sphalerite, quartz, cassiterite and clay minerals. Stage VI mineralization is characterized by the development of mineralization in fine veinlets (<1 mm wide) with mineralogy similar to stage III but with higher modal abundances of kesterite (~ 50 %). Stage VII is characterized by the occurrence of Sn-Ag-bearing sulfosalts and sulfides in the pore spaces developed within sulfide mineralization of previous stages. Sphalerite, pyrite, arsenopyrite, canfieldite and galena formed first in this stage. These minerals were then overgrown by minerals of the pirquitasite-hocartite series, canfieldite and stannite. Galena was overgrown by fibrous frankeite. Stage VIII is characterized by abundant clays, marcasite and hydrous phosphates such as goyazite. This final stage reflects the waning of the hydrothermal system and deposition of lower-temperature minerals. All of the ore stages with the exception of stage VII and possibly stage IV, were initiated following brecciation events given that the later-forming stages occur coating clasts of previously formed mineralization.

Fluid-inclusion data from Slater *et al.* (in prep.) suggest that some mineralization, including the colloform ores of stages II and IV, resulted from the intermittent flashing and boiling of a mixed predominantly magmatic fluid. The fluid inclusion data also suggest that mixing between magmatic and meteoric fluids likely occurred and this may have also contributed to mineral deposition.

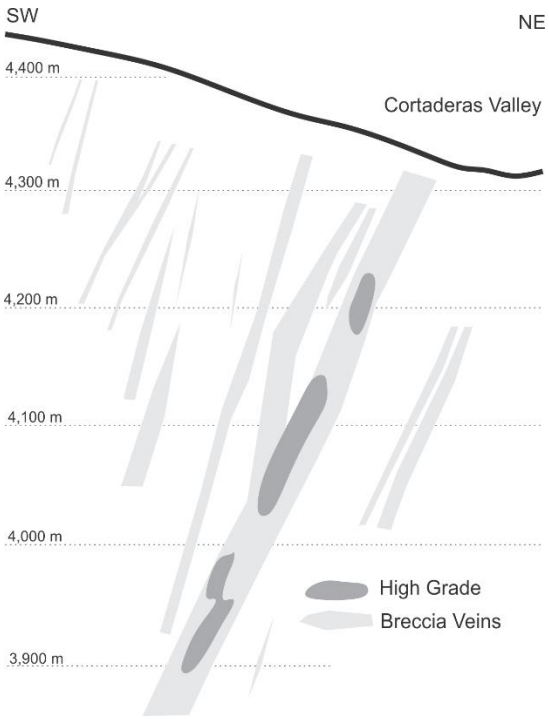

Figure 2: Schematic cross-section for the CZ interpreted from drill core intercepts showing the high-grade zone and other breccia veins.

Sphalerite is the principal host for Zn mineralization in the CZ. It locally exhibits colloform textures with rhythmic banding of dark brown and tan layers (e.g., stage II). Other occurrences of sphalerite formed during (stage III) and after (stages IV, V, VI, and VII) the main stage of Ag-mineralization. Pyrite is also a major component of mineralization in the CZ and occurs in every paragenetic stage. In stage V it occurs as aggregates of grains with concentric growth zones and local colloform textures.

The CZ contains a variety of sulfosalts in several paragenetic stages which generally occur as blebby inclusions in galena or as convoluted intergrowths with galena and other sulfosalts. The origins of these textures are not straightforward to interpret and could have formed by intergrowths of cogenetic minerals, replacement or unmixing. A dominant sulfosalt is Ag-bearing tetrahedrite

occurring with pyrargyrite, miargyrite and sphalerite which may prove useful for sulfosalt thermometry.

This study aims to describe and interpret the following:

1. The compositional variations in colour-banded colloform sphalerite (stage II) as well as other stages of sphalerite (stages III, and IV) as determined by LA-ICP-MS.
2. The compositional variations in concentrically zoned pyrite (stage V) as determined by LA-ICP-MS.
3. The textural relationship between various sulfosalt inclusions and galena by petrographic studies, SEM-EDS, EMPA and heating experiments.
4. The nature of convoluted sulfosalt intergrowths by petrographic studies, SEM-EDS, EMPA and heating experiments.
5. The compositions of Ag-bearing tetrahedrite (stages III and IV) and their applicability as a geothermometer by EMPA.

		Pyritization (I)	Sph (II)	Ag (III)	Sph (IV)	Massive Sulfide (V)	Ag (VI)	Ag-Sn (VII)	Waning (VIII)
Gangue	Quartz	X	X	X		XX			X
	Sericite	X							X
	Clays					X			XXX
	Goyazite					X			X
	Siderite					X			X
Sulfides	Pyrite	XXX	X	XX	X	XXX	X	X	X
	Sphalerite		XXX	XX	XX	XX	X	X	
	Marcasite					XX			X
	Arsenopyrite		XX	XX			X	X	
	Galena		XX	XX				XX	
	Cassiterite			X		X		X	
Sulfosalts	Proustite-Pyrargyrite		X	X			X		
	Jordanite			X					
	Kesterite-Stannite			X		X	XXX	X	
	Smithite-Miargyrite			X			X		
	Ag-bearing Tetrahedrite			XX			X		
	Boulangerite			X					
	Frankeite							X	
	Canfieldite							XX	
	Pirquitasite-Hocartite							XX	

– – – – – – – – Brecciation **XXX** - Very Abundant **XX** - Abundant **X** - Present

Figure 3: Paragenetic sequence for the CZ from Slater *et al*. (in prep). The timing of brecciation is indicated by the dashed lines. The relative abundances of minerals in each stage are included with "very abundant" representing > 50 modal %, "abundant" representing > 10 modal %, and "present" representing < 10 modal %.

Sampling Methodology and Analytical Techniques

The samples used in this study were obtained from drill core. Both thick (100 μm) and standard polished thin sections were made from samples for reflected light ore petrography and mineral chemistry studies. Exploratory heating experiments were performed on 100 μm thick-section chips at 250 °C, 300 °C and 350 °C for various run times. Three polished thick sections made from two samples of sphalerite (samples DDH-230I and DDH-230C) and were analysed by LA-ICP-MS traverses and spots. One polished thick section with pyrite (DDH-230F) was studied by LA-ICP-MS maps and spots.

Ore petrography using reflected and transmitted light was carried out using an Olympus BX51 microscope. Ore textures were assessed and representative samples were examined further by SEM-EDS methods.

The major- and minor-element compositions of some of the sulfides and sulfosalts observed in this study were analyzed using a JEOL JSM-6400 SEM equipped with an Oxford Instruments INCA EDS system in the Central Analytical Facility of Laurentian University, Sudbury. The analyses were performed using a beam current of ~1 nA, accelerating voltage of 20 kV and live times of 5 to 30 s. The K-series X-ray lines were analyzed for S, Fe, Cu and Zn, the L-series X-ray lines were analyzed for As, Ag, Cd, In and Sn and the M-series X-ray lines were analyzed for Pb and Bi.

Sulfosalts were identified on the basis of their composition, morphology and optical properties. Owing to peak-overlap issues associated with SEM-EDS analyses, the major and minor-element compositions of these minerals were determined quantitatively with a SX-50 Cameca electron microprobe (EMP) in the Central Analytical Facility of Laurentian University, Sudbury. Operating conditions were 20 kV and 20 nA with 10 s on the peak and 5 s on the background. The beam diameter was 5 μm. The standards were chalcopyrite (Fe, Cu, S), sphalerite (Zn), PtAs (As), Ag metal (Ag), Sn metal (Sn), RhSb (Sb) and PbTe (Pb). For sulfosalt geothermometry, twenty-five spot analyses were performed on two stages of Ag-bearing tetrahedrite that were in apparent equilibrium with pyrargyrite, miargyrite and sphalerite.

The minor- and trace-element compositions of sphalerite and pyrite were determined using LA-ICP-MS at the Geochemical Fingerprinting Laboratory of Laurentian University, Sudbury. The instrument had a Resonetics Resolution M-50 laser ablation instrument coupled to a Thermo X-Series II quadropole detector. The analytes included Mg, S, Mn, Fe, Co, Ni, Cu, Zn, Ge, As, Se, Nb, Mo, Ag, Cd, In, Sn, Sb, Te, La, Au, Pb and Bi. Traverses using a 66 μm beam diameter and a repetition rate of 6 Hz were performed on three polished thin sections made from two samples (DDH-230I and DDH-230C) that contained sphalerite from stages II, III and IV. Maps from LA-

ICP-MS analyses were created for concentrically zoned stage V pyrite grains in sample DDH-230F using a 10 μm beam diameter and a repetition rate of 6 Hz. Single spot analyses on each of these stages of sphalerite were performed with a 124 μm beam diameter and a repetition rate of 10 Hz. The relatively large beam size was chosen to smooth out the local variations in sphalerite composition caused by the narrow width of colloform layers. Single spots for the core and second growth zone of the pyrite grain were analyzed using a 36 μm beam diameter and a repetition rate of 10 Hz. Internal standards (NIST 612, BHVO2g, and MASS) were analysed before and after each single spot and traverse or map segment. Data reduction was undertaken using S as the internal standard for both sphalerite and pyrite.

Dry heating experiments using a calibrated Linkam FTIR 600 heating-cooling stage were performed on samples with emulsion-like textures. Polished thin section chips were heated to 250 °C, 300 °C and, in some cases, 350 °C for times varying between 2 and 9 hours. Parameters such as fO_2 and fS_2 were not controlled for these experiments.

Results

Texture and Composition of Ore Minerals

The dominant minerals are sphalerite, pyrite, marcastite, arsenopyrite, cassiterite, galena and numerous sulfosalts. The sulfosalts observed in this study include Ag-bearing tetrahedrite, boulangerite, jordanite, pyrargyrite-prousite, miargyrite-smithite, canfieldite (including a Te-bearing variety), kesterite-stannite, frankeite, pirquitasite-hocartite and possibly pavonite. Several unidentified Ag-Pb-Sb-Bi-S minerals have also been observed through SEM-EDS studies. The textures of some sulfosalts and their assemblages are described below. Sulfosalt compositional data as determined by EMP are presented in Table 1.

Table 1: Electron microprobe analyses of sulfosalts from the CZ. The paragenetic stage to which sulfosalts belong, are indicated by roman numerals.

Mineral	Te-Canfieldite	Pavonite(?) + Galena(?)	Prousite	Miargyrite	Pyrargyrite	Boulangerite	Kesterite	Tetrahedrite	Jordanite	Hocartite
Stage	?	?	II	III	III	III	III	III	III	VII
n =	3	4	1	3	1	1	2	19	4	1
Wt. % (avg.)										
Ag	62.31	10.96	65.32	35.70	59.45	0.09	0.79	24.22	0.09	41.12
Cu	0.00	0.00	0.01	0.01	0.00	0.00	28.92	19.16	0.00	0.05
Fe	0.01	0.37	0.02	0.00	0.02	0.00	3.50	2.91	0.00	9.27
Sb	0.00	0.66	0.73	40.52	20.69	24.75	0.00	24.45	4.73	0.00
Sn	8.73	0.34	0.05	0.22	0.08	0.12	27.23	0.21	0.12	23.15
As	0.00	0.00	13.54	1.03	1.68	1.07	0.00	1.81	7.93	0.00
Zn	0.00	0.01	0.00	0.00	0.00	0.00	10.66	3.20	0.03	1.31
Pb	1.17	6.54	0.00	0.00	0.00	55.21	0.00	n.a.	68.95	0.00
Te	18.14	0.33	0.00	0.00	0.00	0.00	0.00	n.a.	0.00	0.00
Se	0.09	0.01	0.00	0.02	0.16	0.00	0.00	n.a.	0.00	0.08
Bi	0.00	62.85	0.00	0.74	0.00	0.00	0.00	n.a.	0.00	0.00
S	9.34	17.44	18.90	20.91	17.68	18.25	29.14	23.60	17.94	24.11
Total	99.79	99.51	98.58	99.16	99.76	99.48	100.25	99.56	99.78	99.10
APFU calculated to S =	6.00	5.00	3.00	2.00	3.00	11.00	4.00	13.00	23.00	4.00
Notes:	(+ Te + Se)	(PbS removed)								
Ag	7.59	0.99	3.08	1.02	3.00	0.02	0.03	3.97	0.03	2.03
Cu	0.00	0.00	0.00	0.00	0.00	0.00	2.00	5.33	0.00	0.00
Fe	0.00	0.06	0.00	0.00	0.00	0.00	0.28	0.92	0.00	0.88
Sb	0.00	0.05	0.03	1.02	0.92	3.93	0.00	3.55	1.60	0.00
Sn	0.97	0.03	0.00	0.01	0.00	0.02	1.01	0.03	0.04	1.04
As	0.00	0.00	0.92	0.04	0.12	0.28	0.00	0.43	4.35	0.00
Zn	0.00	0.00	0.00	0.00	0.00	0.00	0.72	0.87	0.02	0.11
Pb	0.07	0.00	0.00	0.00	0.00	5.15	0.00	0.00	13.68	0.00
Te	1.87	0.03	0.00	0.00	0.00	0.00	0.00	0.00	n.a.	0.00
Se	0.02	0.00	0.00	0.00	0.01	0.00	0.00	0.00	n.a.	0.01
Bi	0.00	2.94	0.00	0.01	0.00	0.00	0.00	0.00	n.a.	0.00
S	3.83	5.00	3.00	2.00	3.00	11.00	4.00	13.00	23.00	4.00

Sphalerite

Sphalerite occurs in all but the first and last stages of mineralization. It commonly develops with a colloform texture, this being best developed in stage II. Located below an elevation of ~4,150 m, the sphalerite of this stage occurs as botryoidal layers with local plumose textures whereas at higher elevations, the sphalerite still develops with a colloform texture but with local coarse-grained patches (gains up to 2 mm across). Layers of sphalerite are typically dark-red to purple-brown in colour, grading to tan (e.g., Fig. 4). In stage III, the sphalerite is dark brown, lacks discernible colour banding and occurs intergrown with various sulfosalts, quartz, pyrite, arsenopyrite and cassiterite. In stage IV, the sphalerite occurs as a band with colloform to crustiform texture whose colour ranges from orange to dark brown. In stage VI the sphalerite

occurs as intergrowths with various sulfosalts in a manner similar to stage III. In stage VII it occurs as coatings on vug walls which formed prior to the sulfosalt mineralization of the same stage.

Figure 4: Example of the colloform texture and rhythmic colour banding present in sphalerite that has overgrown pyritized wall rock.

The tan and dark brown bands within stage II colloform sphalerite (samples DDH-230I and DDH-230C) were analyzed by LA-ICP-MS. Results show that the tan bands are enriched in Cd, In and Sb, but depleted in Fe, Ag, As and Mn relative to the dark brown bands (Table 2). The most notable compositional difference between the two sphalerites of the same stage is that the tan bands have low Fe contents (0.65-0.84 wt. %, 0.72 wt. % avg.), but high Cd contents (4,743-6,840 ppm, 6,176 ppm avg.) relative to the dark brown bands (3.84 wt. % Fe avg. and 821 ppm Cd avg.). For sample DDH-230C, only one spot analysis was taken from each of the dark and light bands of colloform sphalerite. The dark brown sphalerite in sample DDH-230C contains elevated levels of Cu (2,300 ppm) and Se (2,333 ppm) relative to the same sphalerite in sample DDH-230I (avg.: 638 ppm Cu and 2.85 ppm Se).

Table 2: Single spot analyses by LA-ICP-MS for sphalerite and pyrite. All values are recorded in ppm except for Fe.

Sample	Mineral (Stage)	Spot	Ag	As	Bi	Cd	Co	Cu	Fe (wt%)	Ge	In	Mn	Mo	Sb	Se	Sn
DDH-230I	Tan Sphalerite (stage II)	1	211	466	0.01	6420	0.06	169	0.84	11.40	1.89	8	0.04	288	3.03	17
		2	180	338	0.02	6840	0.05	130	0.83	18.40	1.47	6	0.05	264	3.11	20
		3	431	489	0.01	6450	<dl	262	0.67	3.25	4.57	10	0.04	388	2.84	80
		4	331	385	0.00	6400	0.05	180	0.66	2.87	2.74	8	0.03	371	2.99	25
		5	381	357	0.00	6200	0.05	187	0.66	4.39	2.30	7	0.11	357	3.30	19
		6	311	735	0.01	4743	0.06	434	0.65	4.75	2.20	20	0.07	392	2.77	130
		Mean	**308**	**462**	**0.01**	**6176**	**0.05**	**227**	**0.72**	**7.51**	**2.53**	**10**	**0.06**	**343**	**3.01**	**48**
		STD	88	134	0.01	668	0.00	100	0.08	5.64	0.99	5	0.03	49	0.17	42
	Dark Brown Sphalerite (stage II)	1	2238	3240	0.09	1018	0.24	652	3.33	68.20	0.23	129	0.04	119	3.24	59
		2	1925	3111	0.01	442	0.31	546	4.19	64.30	0.13	134	0.10	84	2.78	10
		3	3224	3238	0.00	1132	0.21	860	3.01	68.50	0.04	122	0.05	182	2.70	11
		4	3905	3416	0.01	1039	0.23	991	2.95	73.90	0.08	123	0.06	177	2.73	20
		5	1034	1640	0.04	577	0.42	338	5.02	45.00	0.04	99	0.05	27	2.68	9
		6	1462	2368	0.02	718	0.34	441	4.53	55.30	0.09	106	0.05	58	2.96	9
		Mean	**2298**	**2836**	**0.03**	**821**	**0.29**	**638**	**3.84**	**62.53**	**0.10**	**119**	**0.06**	**108**	**2.85**	**20**
		STD	990	631	0.03	257	0.07	228	0.79	9.66	0.07	13	0.02	58	0.20	18
	Dark Brown Sphalerite (stage III)	1	2383	31500	11.64	5650	0.39	3230	7.00	0.64	2025	17	0.05	372	6.56	1810
		2	2060	42300	11.35	5672	0.31	3560	7.96	1.03	2440	17	0.05	496	7.53	2035
		3	2290	21500	7.81	5870	0.18	3281	5.47	0.85	2308	19	0.17	331	6.82	1701
		Mean	**2244**	**31767**	**10.27**	**5731**	**0.29**	**3357**	**6.81**	**0.84**	**2258**	**18**	**0.09**	**400**	**6.97**	**1849**
		STD	166	10403	2.13	121	0.11	178	1.26	0.20	212	1	0.07	86	0.50	170
	Dark Brown Sphalerite (stage IV)	1	100	16	0.00	93	3.81	91	3.16	0.81	0.864	40	0.06	82	2.80	246
		2	2350	1407	0.21	1083	0.05	2298	3.34	37.75	16.95	50	0.06	1589	2.82	4460
		3	1140	1201	0.02	674	0.04	2511	3.50	36.70	17.57	33	0.04	1409	3.20	4650
		4	744	13	0.00	3154	1.27	53	0.90	0.49	0.275	14	0.04	103	2.82	59
		5	148	13	0.00	276	2.67	181	2.42	0.90	1.324	41	0.03	202	2.84	409
		6	434	13	0.00	857	1.68	21	1.80	0.57	0.24	31	0.06	164	2.74	71
		Mean	**819**	**444**	**0.04**	**1023**	**1.59**	**859**	**2.52**	**12.87**	**6.20**	**35**	**0.05**	**592**	**2.87**	**1649**
		STD	845	670	0.08	1106	1.48	1200	1.02	18.87	9	12	0.01	706	0.17	2255
DDH-230C	Light Orange Sphalerite (stage II)	1	**2**	**7**	**0.00**	**2933**	**35.08**	**49**	**2.25**	**2.03**	**0**	**15**	**0.04**	**2**	**34.20**	**0.03**
	Dark Brown Sphalerite (stage II)	1	**776**	**10**	**0.00**	**3803**	**11.24**	**2300**	**8.88**	**8.69**	**0**	**95**	**0.05**	**2**	**2333**	**0.02**
									Zn (wt%)				**Au**			
DDH-230F	Pyrite Core (stage V)	1	**221**	**4160**	**0.35**	**241**	**0.28**	**174**	**3.44**	**0.63**	**22**	**4**	**0.18**	**70**	**2.3**	**205**
	Pyrite Growth Zone 2 (stage V)	1	**318**	**24490**	**2.60**	**18.2**	**2.11**	**541**	**1.79**	**1.09**	**12.2**	**<dl**	**0.35**	**288**	**0.7**	**167**

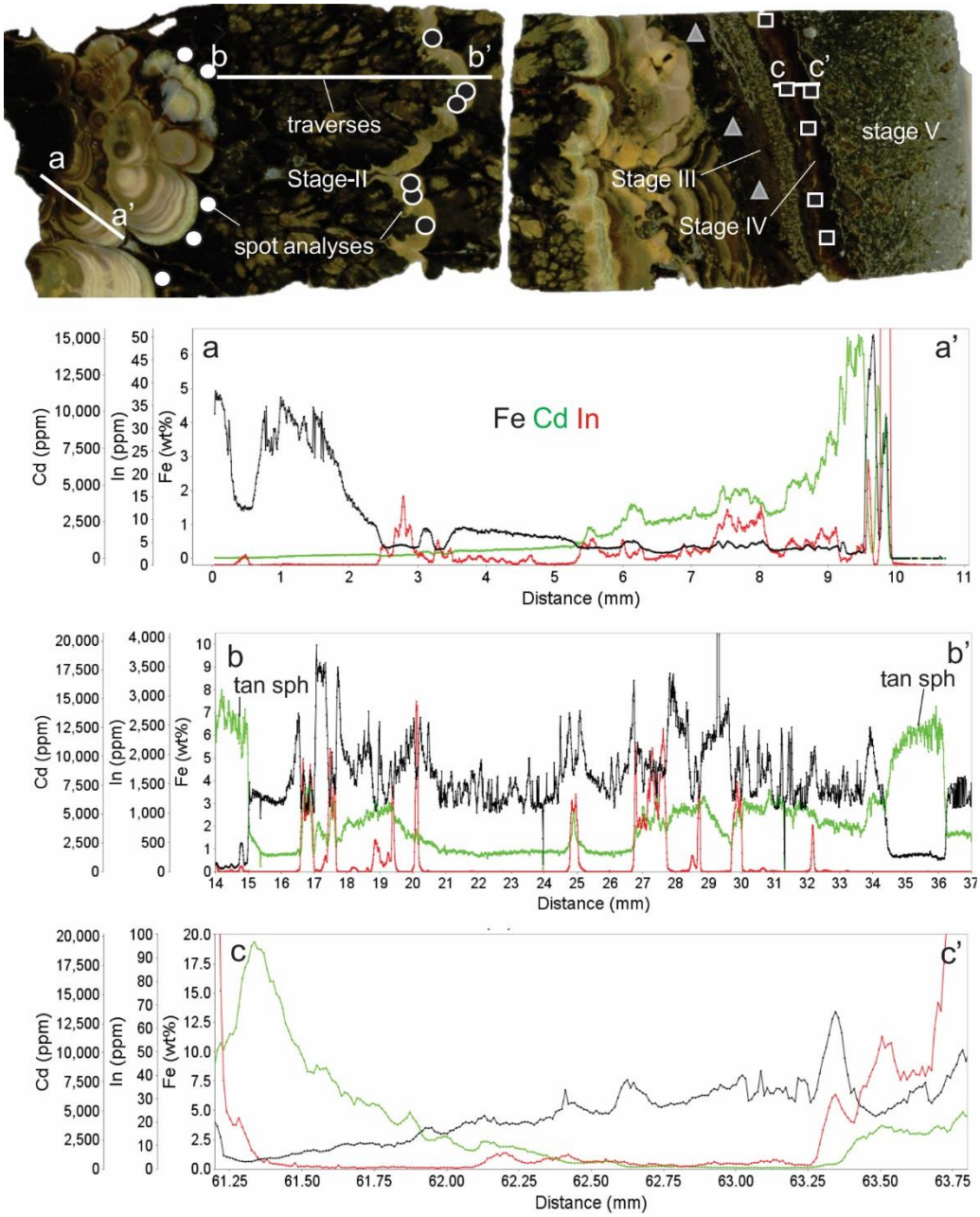

Figure 5: Laser ablation-ICPMS traverses and spot analyses made on polished thick sections of colloform sphalerite from sample DDH-230I. Traverse "a" is through the first sequence of dark brown to tan colloform sphalerite of stage II. Traverse "b" is through the second sequence of colloform sphalerite in stage II. Traverse "c" is through colloform to banded sphalerite of stage IV. Plots of Cd, In and Fe for these three traverses are included below the image.

The sphalerite of stage III is dark reddish-brown and lacks discernable colour banding under transmitted light. It is enriched in minor- and trace-elements relative to other stages including: Ag, As, Bi, Cd, Cu, Fe, In and Sn. The sphalerite of stage IV is medium reddish-brown

and variably enriched in minor and trace-elements including the elements Ag, As, Cd, Cu, Fe, Ge, Sb and Sn. Some analyses (e.g., 2 and 3 from Table 2) show enrichments in Ag (2,350 and 1,140 ppm), As (1,407 and 1,201 ppm), Cu (2,298 and 2,511 ppm), Ge (37.75 and 36.70 ppm), Sb (1,589 and 1,409 ppm), and Sn (4,460 and 4,650 ppm). Analysis "1" has 3.16 wt. % Fe which is similar to the Fe contents obtained in analyses "2" and "3" (3.34 wt. % and 3.35 wt. % respectively) but does not show enrichments in the previously mentioned elements. Analysis "4" is depleted in Fe (0.90 wt. %) but is enriched in Cd (3,154 ppm).

Time-series profiles for elements of interest (Zn, Fe, As, Cu, Ag, Sb, Pb, In, Ge, Bi, Sn and Cd) were created from the raw LA-ICP-MS count data for single spot analyses (Fig. 6). That for the tan sphalerite of stage II is relatively flat, with smooth count rates for all elements, suggesting that they may be structurally bound in the sphalerite. That for dark brown sphalerite of stage II shows flat count rates for Zn, Cd, Sb, Ag, In and possibly Cu; however, the count rates for Pb, Bi, and As are ragged, suggesting that Pb, Bi, and As may in fact be hosted in mineral inclusions within the sphalerite. The coincident small spike in Ag and Sb may have resulted from an inclusion of a Ag-Sb-bearing sulfosalt. The time-series profile for dark brown sphalerite of stage III has relatively flat count rates for Zn, In Cu, Cd, Sb and Ge, whereas, As, Ag, Sn, Pb, and Bi count rates are irregular. This suggests that As, Ag, Sn, Pb and Bi are also hosted in mineral inclusions. The time-series profile for red/brown sphalerite of stage IV shows relatively flat count rates for all elements of interest with the exception of a few small peaks suggesting that the elements might be bound in the structure of sphalerite as opposed to hosted in inclusions. It should be noted that the large beam diameter used in this study would tend to mask the presence of homogeneously distributed micro-inclusions of minerals and thus, their presence cannot be ruled out.

Laser ablation-ICPMS traverses were performed on sphalerite from two stages in sample DDH-230I, each showing colour banding. Preliminary assessment of the data indicates that Cd is negatively correlated with Fe and therefore, these elements are plotted for each traverse (Fig. 5). Indium, being an important and potentially valuable ore metal is included in the plots as well. The data for the traverse through the first sequence of stage II colloform sphalerite where the color progresses from dark brown to tan, shows that the Fe content is well correlated with its colour with dark bands being enriched in Fe (up to ~5 wt. %) and the tan bands being depleted in Fe (~0.3 wt. % avg.). The concentrations of both Cd and In negatively correlate with Fe in this traverse segment.

The second traverse is through the second sequence of colloform sphalerite of the same stage. The dark brown portion (up until ~36 mm) has a composition which is variable with respect to Fe (range of ~3-9 wt. %, average of 4.4 wt %), Cd (range of 2,000-6,000 ppm, average of 1,200 ppm avg.) and In (range of below detection up to 1,500 ppm, average of 200 ppm). The sphalerite from ~34.5 to ~36 mm is tan and relatively homogeneous with respect to Fe (range of ~0.5-1.0 wt. %, 0.7 wt. % avg.), Cd (range of ~7,800-14,00 ppm, 11,000 ppm avg.) and In (range of ~1-10 ppm, 2 ppm avg.). The negative correlation between Fe and Cd is also strong in this traverse, with In concentrations being variable and locally elevated (range of ~500-3,000 ppm, ~1,500 ppm avg.) irrespective of Fe-content.

In the traverse through colloform to banded reddish-brown sphalerite of stage IV, Fe content generally increases throughout the traverse as the colour of the sphalerite changes from red (~1.0 wt % Fe) to brown (~7.5 wt. % Fe). There is a negative correlation between Cd and Fe and In does not appear to be strongly correlated with Fe.

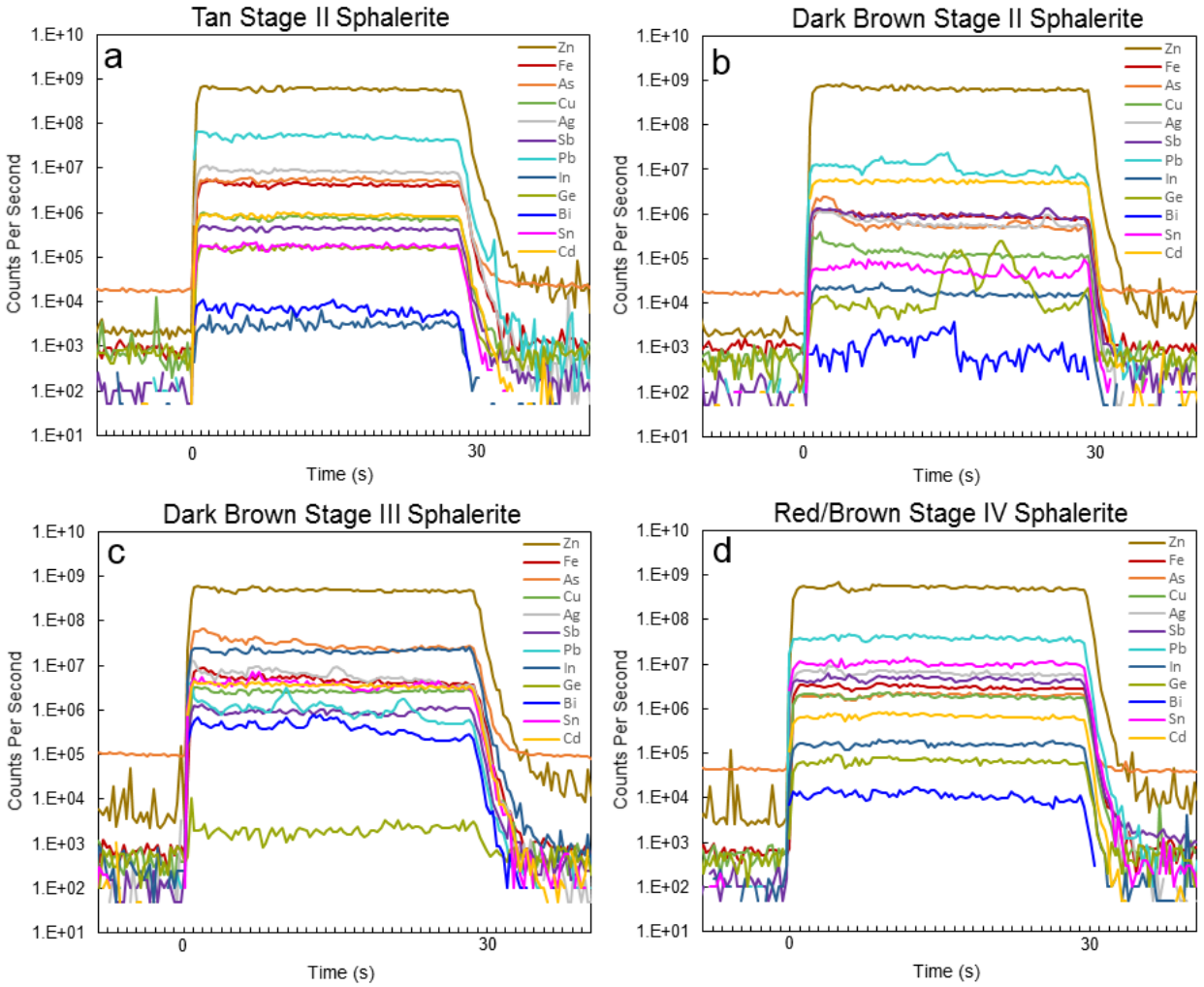

Figure 6: Raw LA-ICP-MS count data (counts per second) for spot analyses with a 124 µm beam diameter in sphalerites from sample DDH-230I. (a) Data from a spot analysis of the tan bands in stage II sphalerite. (b) Data from a spot analysis of the dark brown portion of stage II sphalerite. (c) Data from a spot analysis of the dark brown stage III sphalerite. Data from a spot analysis of the red/brown sphalerite from stage IV.

Pyrite

Pyrite is a significant component of the mineralization and ubiquitous throughout all of the paragenetic stages. Pyrite from stage V is unique in that it locally occurs with concentric growth zones visible under reflected light and back-scattered electron images, these being particularly well-developed in the Ag-rich sample DDH-230F. Here, pyrite occurs as aggregates of grains (~20 to 300 µm across) but, in other samples it has colloform textures where it is interlayered with

marcasite. The concentric growth zones observed in sample DDH-230F may have formed contemporaneously with the colloform pyrite and marcasite.

In order to better understand the mechanism(s) behind the observed concentric zonations in pyrite, maps were derived from Laser ablation-ICPMS analyses of zoned grains in sample DDH-230F accompanied by single spot analyses (Fig. 7). Results indicate that there is a subhedral core which contains low concentrations of trace-elements and appears to be relatively inclusion-free. The core is overgrown by at least three subsequent growth zones, followed by a final rim. The first growth zone is rounded and enriched in several trace-element including Ag, As, Cu, Co, Ni, Sb and Pb. The second growth zone is rounded and enriched with As, Cu and Sb. The third growth zone is cubic and appears to be relatively depleted in trace-elements (i.e., similar to the values given for the core) with the exception of a discrete band with elevated Ag, Sb and Pb. The outer rim is rounded and appears to have approximately the same enrichments as the first growth zone but is also enriched with up to 4 ppm Au and 800 ppm Bi. Based on the distribution of elements in the map, it is apparent that at least three sets of elements are spatially coupled: As-Cu, Ag-Sb-Pb and Au-Ni-Co(-Bi).

Time-series profiles for elements of interest (Fe, As, Cu, Ag, Sb, Pb, Au, Ni, Co, Zn, Sn and Cd) were created from the raw LA-ICP-MS count-data for single spot analyses of the pyrite core and second growth zone (Fig. 8). The core shows flat count rates for Fe and As, but erratic patterns for all other elements, the latter suggesting that these elements likely reflect the presence of mineral inclusions. The second growth zone shows flat count rates for Fe and As, along with that for Sb being relatively flat. This may suggest that elements other than these indicate the presence of mineral inclusions (the nature of which are speculated upon in the Discussion section).

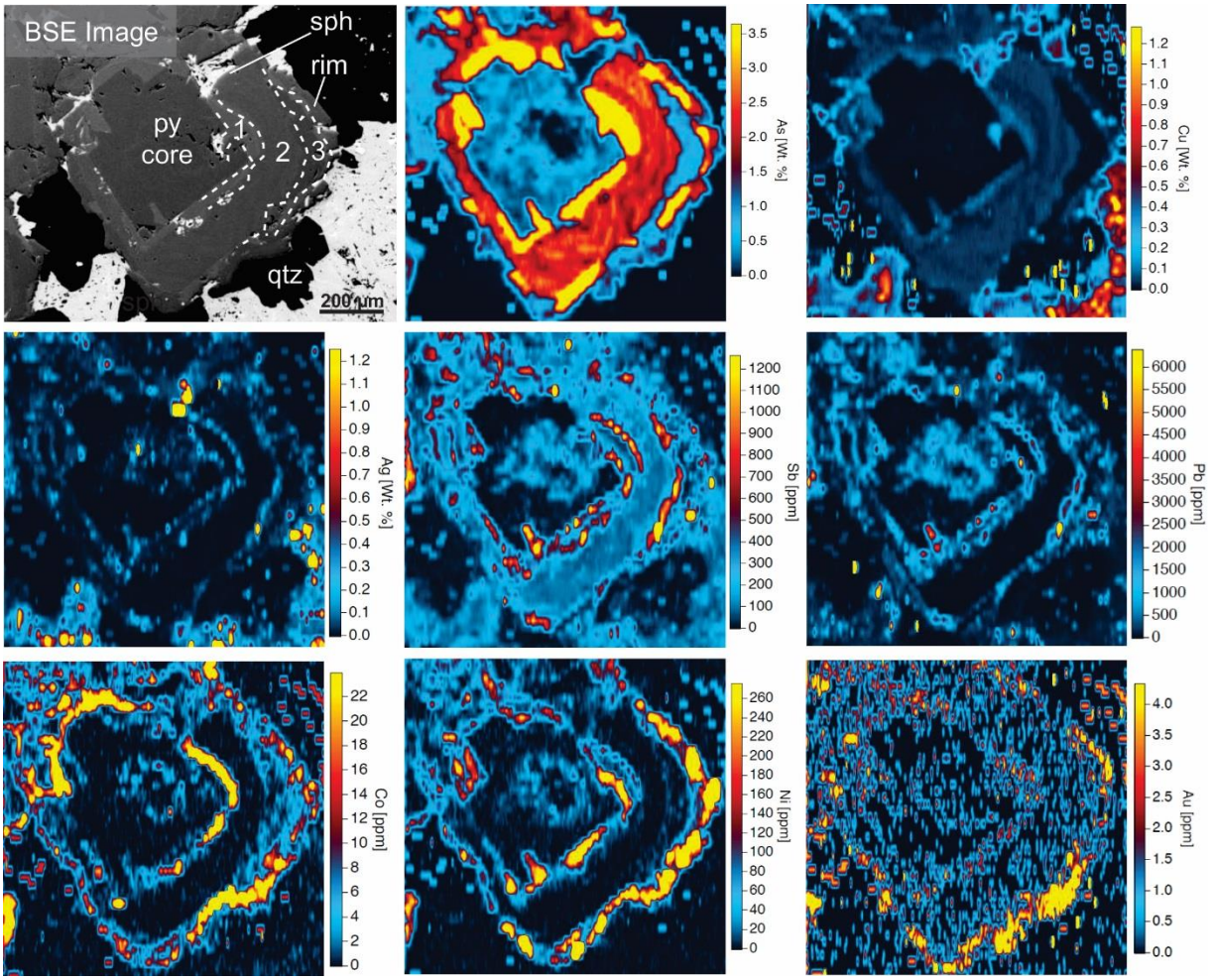

Figure 7: The backscattered-electron (BSE) image and compositional maps (based on LA-ICP-MS data) of a concentrically zoned stage V pyrite grain. The core, growth zones ("1", "2" and "3") and rim are outlined with dashed white lines on the BSE image. The compositional maps have linear scaling.

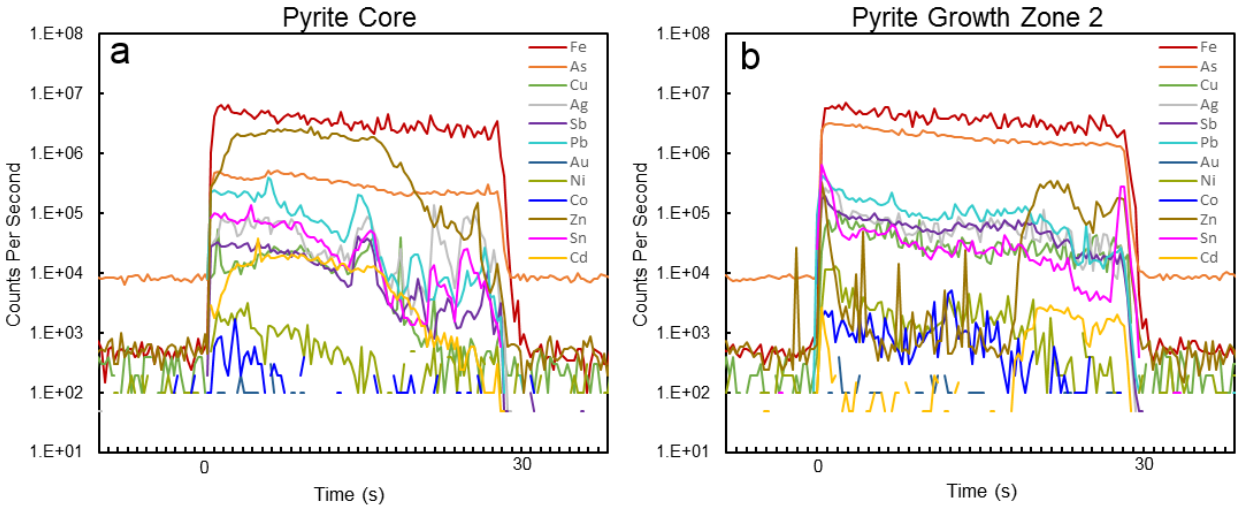

Figure 8: Raw LA-ICP-MS data for spot analyses of stage V pyrite in sample DDH-230F. (a) Data for the core. (b) Data for the second concentric growth zone.

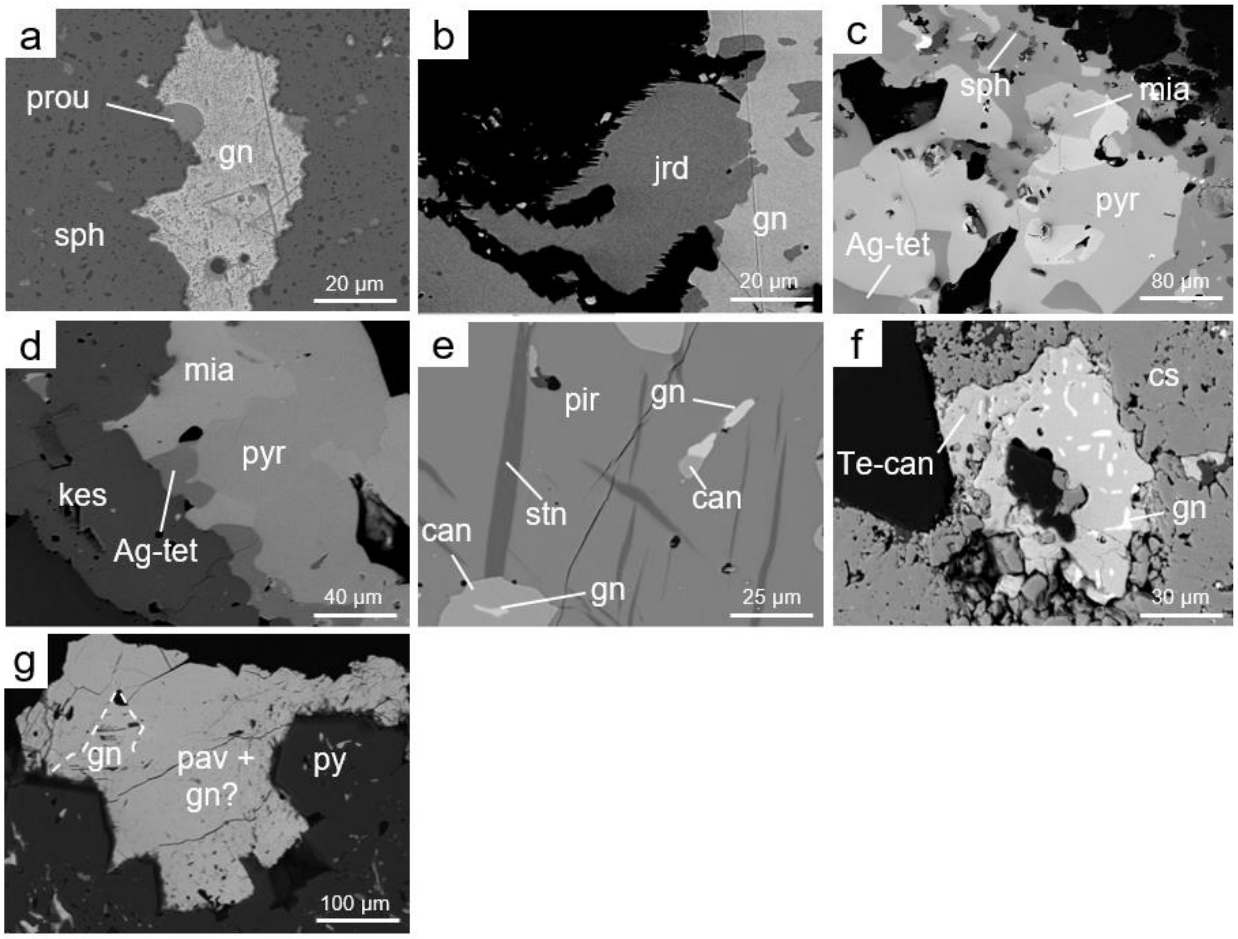

Figure 9: Backscattered-electron images of sulfosalt assemblages in the CZ. (a) Blebby inclusions and globules of proustite (prou) in galena (gn) that is intergrown with sphalerite (sph) of stage II. (b) Intergrowth of jordanite (jrd) with galena of stage III. (c) Intergrowth of Ag-bearing tetrahedrite (Ag-tet), sphalerite, miargyrite (mia) and pyrargyrite (pyr) of stage III. (d) Intergrowth of Ag-bearing tetrahedrite, miargyrite and pyrargyrite surrounded by kesterite (kes) of stage VI. (e) Pirquitasite (pir) containing exsolution lamellae of stannite (stn) and also inclusions of canfieldite (can) with galena of stage VII. (f) Te-bearing canfieldite (Te-can) with blebby inclusions of galena surrounded by colloform cassiterite (cs) of an unknown stage hosted in the clasts of a post- to syn-mineral breccia. (g) Intergrowth of galena and a mineral whose composition resembles that of a mixture of pavonite (pav) and galena which have overgrown inclusion-rich pyrite. This mineralization is of an unclassified stage due to its occurrence in clasts of a post-mineral breccia.

Proustite and Galena

The colloform sphalerite of stage II is intergrown with grains of galena that are tens of microns to several millimeters across, these being generally elongated parallel to the direction of sphalerite layering (Fig. 9a). The grains of galena contain blebby inclusions and globules of proustite (5 to 60 μm in diameter) disseminated throughout. It may be noteworthy that the inclusions of proustite are only present in samples collected from deeper levels of the CZ. To evaluate temperatures of homogenization for grains of galena and proustite, a sample was heated was heated to 250 ºC and 300 °C using a thermometric stage. When heated to 250 °C for 8 hours no changes were observed, however when this grain was heated to 300 °C for eight hours, proustite changed colour, going from dark grey to a white under reflected light. Importantly, a new dark grey phase formed at the boundaries between proustite and galena occupying the space previously held by galena. Homogenization did not occur over the 8 hours period.

Jordanite, Galena and Boulangerite

In the upper levels of the deposit, there are rare veins that contain galena, jordanite and locally boulangerite (Fig. 9b). Jordanite occurs as blebby inclusions and globules in galena as well as intergrowths with galena. In one sample, the galena portion of a galena-jordanite intergrowth has been partially dissolved and replaced by sphalerite (Fig. 10). The nature of the intergrowth locally resembles a sympletcitc texture with worm-like zones of jordanite within galena. In another sample, jordanite only occurs as rare globules in galena that is associated with abundant fibrous boulangerite.

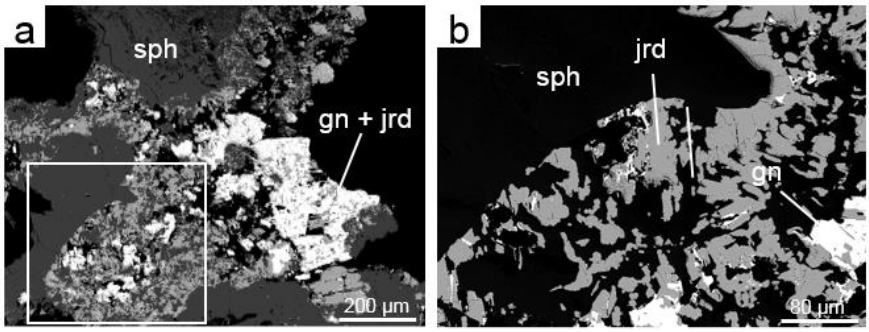

Figure 10: Backscattered-electron images of galena-jordanite veins from stage III mineralization. (a) Symplectic intergrowth of galena (gn) and jordanite (jrd) (b) Magnified view of (a) showing the galena-jordanite symplectic intergrowth and the worm-like morphology of jordanite grains.

Silver-Bearing Tetrahedrite, Miargyrite, Pyrargyrite and Kesterite

In deep levels of the CZ (e.g., below 4,100 m ASL) dark sulfosalt-rich bands belonging to stage III encrust clasts and breccia margins. The mineralogy of these bands consists of Ag-bearing tetrahedrite, miargyrite, pyrargyrite, sphalerite, kesterite, quartz, cassiterite, pyrite, arsenopyrite, an unidentified Ag-Sb-Pb-S mineral as well as various unidentified Bi-Pb-Ag(-Mo)-bearing minerals. Euhedral quartz and sphalerite + cassiterite intergrowths are both surrounded by paragenetically late sulfosalts. The minerals including Ag-bearing tetrahedrite, pyrargyrite, miargyrite, sphalerite and locally kesterite, occur as intergrowths with smooth mutual grain boundaries (Fig. 9c). The grain boundaries between pyrargyrite and miargyrite terminate against the Ag-bearing tetrahedrite in a manner that suggests that the boundaries of Ag-bearing tetrahedrite were present prior to the formation, or separation, of miargyrite and pyrargyrite. When a chip containing this mineralization was heated at 300 °C for five hours, the boundary between miargyrite and pyrargyrite began to become less discernible when viewed under reflected light; this could possibly represent the initial stages of homogenization of these two phases.

Occurring with the dark sulfosalt-rich bands of stage III are narrow (<1 mm) stage VI veinlets that cross-cut the mineralization of stage III and other previously formed stages. The veinlets have the same mineralogy as stage III; however, kesterite is found as the dominant

sulfosalt (>50 modal %) rather than Ag-bearing tetrahedrite, which is only present as a minor component (Fig. 9d). Kesterite is typically found surrounding subhedral pyrite grains and contains patches of miargyrite, pyrargyrite, Ag-bearing tetrahedrite and sphalerite. The miargyrite grains contain rare rounded inclusions and patches of an unidentified Pb-Ag-Sb-S-bearing mineral similar to that observed in stage III.

Pirquitasite-Hocartite and Stannite

Late in the paragenesis, polymetallic mineralization of stage VII developed within pores and vugs. The mineralization is composed of pirquitasite-hocartite, stannite, arsenopyrite, pyrite, galena, canfieldite, cassiterite, sphalerite and frankeite (Fig. 9e). The Zn-rich grains of pirquitasite-hocartite contain lamellae of stannite (<20 µm across) which are discontinuous and occur in two principal orientations that vary from roughly 60 º to 90 ° apart. The more Fe-rich grains (i.e. hocartite) do not contain lamellae of stannite.

Canfieldite and Te-bearing Canfieldite

Canfieldite occurs with galena of stage VII mineralization either as inclusions in grains of pirquitasite-hocartite solid solution, or as rounded grains on fragment margins. Canfieldite sometimes occurs as rounded inclusions or globules in galena (Fig. 9e). A Te-bearing variety of canfieldite occurs in rounded clasts in a late-stage breccia and is from an undetermined paragentic stage. The Te-bearing canfieldite occurs as patches containing blebby inclusions of galena. The two minerals are encased by colloform cassiterite (Fig. 9f). The blebs of galena have an average diameter of about 5 µm and tend to have elongated shapes with several preferred orientations.

Pavonite

Mineralization of an undetermined paragenetic stage hosted within clasts of a late-stage breccia contains pyrite, sphalerite, colloform cassiterite (i.e., *var*. wood tin), kesterite, several Bi-

Ag-Pb-S minerals, Te-bearing canfieldite and galena. The composition of the dominant Bi-Ag-Pb-S mineral determined by EMPA could not be conclusively matched to a known mineral. It is commonly associated with galena (Fig. 9g). To test the possibility that the mineral contained fine-grained inclusions of galena, PbS was subtracted and the composition was recalculated. The recalculated composition very closely matches that of pavonite (average: $Ag_{0.99}Bi_{2.94}S_{5,}$ $n = 4$).

Sulfosalt Geothermometry

The compositions of Ag-bearing tetrahedrite ("fahlore") from mineralization of stages III and VI occurring in the same thin section were determined by EMPA. The Ag/(Ag+Cu) and Zn/(Zn+Fe) ratios were then calculated in order to estimate the temperature at which the two stages of Ag-bearing tetrahedrite equilibrated with an assemblage of miargyrite, pyrargyrite, and sphalerite following the methodology of Sack and Lichtner (2009; Table 3). The Ag-bearing tetrahedrite from stage III has Ag/(Ag+Cu) ratios averaging 0.43 (n = 19) with a range of 0.40 to 0.56 ($1\sigma = 0.03$) and Zn/(Zn+Fe) ratios averaging 0.49 with a range of 0.44 to 0.59 ($1\sigma = 0.10$). Stage VI Ag-bearing tetrahedrite has Ag/(Ag+Cu) ratios averaging of 0.45 (n = 6) with a range of 0.44 to 0.48 ($1\sigma = 0.01$) and Zn/(Zn+Fe) ratios averaging 0.51 with a range of 0.46 to 0.53 ($1\sigma = 0.03$). These data are plotted on isotherms from Sack and Lichtner (2009) (Fig. 11). The average composition of stage III Ag-bearing tetrahedrite plots at approximately 245 °C ± 15 °C whereas the average composition of stage VI Ag-bearing tetrahedrite plots at approximately 270 °C ± 10 °C.

Table 3: Analyses for Ag-bearing tetrahedrite by EMPA.

Mineral Analysis	Stage	Ag (wt. %)	Cu (wt. %)	Fe (wt. %)	Sb (wt. %)	As (wt. %)	Zn (wt. %)	Sn (wt. %)	S (wt. %)	Total (wt. %)	Ag/ (Ag+Cu)	Zn/ (Zn+Fe)
1	III	25.1	18.7	3.04	24.7	1.48	2.96	n.a.	24.8	100.7	0.44	0.45
2	III	24.4	19.2	3.10	24.5	1.51	2.79	n.a.	24.5	100.0	0.43	0.44
3	III	24.2	18.1	2.29	25.3	1.09	3.50	n.a.	24.4	98.9	0.44	0.57
4	III	23.5	18.3	3.18	24.2	1.69	2.71	n.a.	24.7	98.3	0.43	0.42
5	III	29.8	14.1	5.34	24.7	1.13	0.72	n.a.	23.1	98.8	0.56	0.10
6	III	24.2	19.3	2.64	24.2	1.89	2.98	n.a.	24.9	100.1	0.43	0.49
7	III	24.4	19.0	2.69	23.8	1.94	3.21	n.a.	24.8	99.9	0.43	0.50
8	III	23.7	19.8	2.61	25.3	1.15	3.34	n.a.	24.8	100.7	0.41	0.52
9	III	23.6	18.5	2.64	24.8	1.27	3.38	n.a.	24.4	98.6	0.43	0.52
10	III	24.5	19.3	2.93	24.1	1.84	3.23	n.a.	24.9	100.8	0.43	0.49
11	III	23.4	20.2	2.42	25.3	1.24	4.09	0.14	21.9	98.8	0.41	0.59
12	III	23.9	20.2	2.82	23.8	2.52	3.45	0.17	22.7	99.5	0.41	0.51
13	III	23.5	20.4	2.87	23.1	2.76	3.83	0.88	23.0	100.5	0.40	0.53
14	III	24.2	19.4	2.64	25.8	1.31	3.44	0.12	22.3	99.1	0.42	0.53
15	III	23.6	19.6	2.75	25.2	1.37	3.38	0.15	22.6	98.7	0.41	0.51
16	III	24.1	19.3	2.77	25.0	1.84	3.36	0.15	22.5	99.2	0.42	0.51
17	III	23.1	20.1	2.86	23.3	3.05	3.56	0.09	22.8	98.8	0.40	0.52
18	III	23.7	20.4	2.65	23.8	2.49	3.63	0.11	22.5	99.3	0.41	0.54
19	III	23.3	20.2	3.05	23.5	2.87	3.28	0.07	22.7	99.0	0.40	0.48
1	VI	25.6	18.4	2.84	25.8	0.98	3.55	0.18	22.0	99.4	0.45	0.52
2	VI	26.3	18.3	2.82	25.7	1.00	3.49	0.21	21.7	99.5	0.46	0.51
3	VI	26.8	17.2	3.03	24.4	2.06	3.01	0.15	22.1	98.7	0.48	0.46
4	VI	25.1	18.7	2.82	25.8	0.95	3.67	0.20	21.4	98.6	0.44	0.53
5	VI	25.1	18.7	2.84	26.1	0.95	3.67	0.20	21.4	99.1	0.44	0.52
6	VI	26.5	18.4	2.86	25.3	0.84	3.50	0.16	21.5	99.1	0.46	0.51

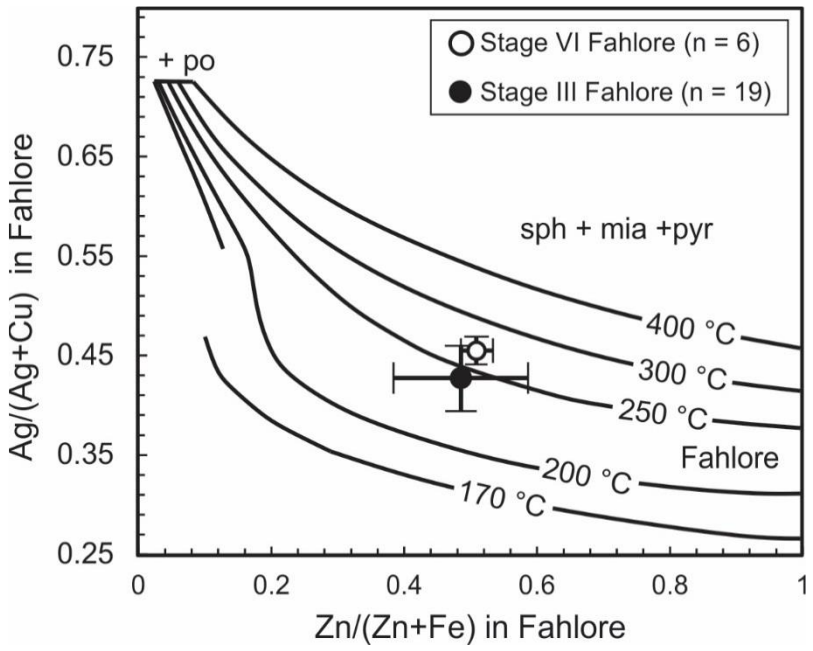

Figure 11: Composition of Ag-bearing tetrahedrite in equilibrium with miargyrite (mia), pyrargyrite (pyr) and sphalerite (sph) from stages III and VI. The range of 1σ is represented with error bars. The isotherms are from Sack and Lichtner (2009).

Discussion

Sulfide-Mineral Chemistry

Sphalerite

Sphalerite is the most common of the three polymorphs of ZnS. It contains tetravalently coordinated Zn and S ions that are arranged in a cubic lattice. Cation substitutions into sphalerite are limited by the relative size of other ions to that of tetrahedrally co-ordinated Zn^{2+} ions. Anions such as Se^{2-}, Te^{2-} and As^{-} can substitute for S^{2-} ions (Cook *et al.* 2009). Johan (1988) proposed a mechanism whereby R^{3+} and R^{4+} cations are incorporated into sphalerite *via* coupled substitutions. This occurs due to the formation of electron-accepting pairs with monovalent ions (Johan 1988). Several subsequent studies have aimed to characterize the substitution mechanisms that have allowed minor and trace elements to incorporate into sphalerite. Several of these studies, based on data from LA-ICP-MS analyses, have focused on sphalerite from hydrothermal ore systems (e.g., Cook *et al.* 2009, Murakami & Ishihara 2013). These demonstrate correlations between cation concentrations that are presented as evidence for coupled substitutions such as $Cu^{+} + In^{3+} \leftrightarrow 2Zn^{2+}$, $Ag^{+} + Sn^{3+} \leftrightarrow 2Zn^{2+}$, $Ag^{+} + Cu^{+} + Sn^{4+} \leftrightarrow 3Zn^{2+}$ and $2Cu^{+} + Sn^{4+} \leftrightarrow 3Zn^{2+}$.

The composition of sphalerite can be a useful discriminant for formation environment and may provide a record of the prevailing conditions during ore formation. For example, Qian (1987) used elemental ratios in sphalerite from Pb-Zn deposits to classify these as being either related to magmatic processes or not. Gottesmann & Kampe (2007) and Gottesmann *et al.* (2009) demonstrated that the Cd/Zn ratios in sphalerite from a Fe-Mn-Zn skarn deposit in Mongolia can track the source of metals in hydrothermal deposits. Barrie *et al.* (2009a) demonstrated that Cd and Cl are enriched in sphalerite layers derived from hydrothermal fluids whereas Fe is enriched in layers derived from a source with a light S isotope signature ($\delta^{34}S$ values of -25 ‰ interpreted to

be bacteriogenic in origin) in their study of a Pb-Zn orebody in Ireland. Gagnevin *et al.* (2014) produced similar results for another Pb-Zn orebody in Ireland by correlating trace-element compositions in layered sphalerites with Fe, Zn and S isotopic data.

The Fe content of sphalerite is widely accepted to effect its colour (e.g., Awadh 2009) although the incorporation of Fe does not appear to significantly distort the sphalerite lattice (Pring *et al.* 2008). The amount of FeS that is soluble in sphalerite is a function of, temperature, pressure and Fe activity (Sack & Ebel 2006). At temperatures above 300 °C, where the activity of Fe is buffered by pyrite and pyrrhotite, the FeS solubility in sphalerite is largely pressure dependant and may be useful as a geobarometer (Scott 1983). Several studies have questioned the validity of using the Fe concentration in sphalerite as a geobarometer (e.g., Banno 1988, Toulmin III *et al*. 1991). Given that the ionic radius of Fe (IV) (0.63 pm: Shannon 1976) is similar to that of Zn (IV) (0.60 pm: Shannon 1976), Fe should easily substitute directly for Zn in sphalerite when it is available ($Fe^{2+} \leftrightarrow Zn^{2+}$).

It is of particular interest to this study to relate the rhythmic colour-banding and associated compositional changes in colloform sphalerite to changes in the ore-forming system. The preliminary work on the CZ by Slater et al. (in prep) used data from fluid-inclusions and petrographic analyses to suggest that colour-banded colloform sphalerite formed in a system that was episodically opening and closing. The composition of sphalerites in the CZ are discussed below in the context of this formational model to evaluate if this process might be recorded in the composition of the sphalerite.

The colour of sphalerite in the CZ correlates well with its Fe content as determined by LA-ICP-MS, for both the colloform and non-colloform stages of sphalerite. For example, the dark brown sphalerite of stage II has an average concentration of 3.84 wt. % Fe whereas the tan

sphalerite of the same stage has an average of only 0.72 wt. %. The dark brown sphalerite of stage III, for which no colloform textures were observed, has an average Fe content of 6.81 wt. %. Stage IV sphalerite has highly variable Fe concentrations (0.90-3.5 wt. %), consistent with its highly variable colour.

The dark brown Fe-rich layers from stage II are interpreted to have formed at the beginning of each cycle of colloform sphalerite growth that following dilation and flashing of the magmatic-dominated fluid to steam. The magmatic-dominated hydrothermal fluid may have been rich in Fe and other metals resulting in dark brown sphalerite that is enriched in trace-elements. The tan layers are interpreted to have formed towards the end of the depositional cycle as the system sealed itself by the deposition of ore and gangue minerals. Stage III sphalerite, which is enriched in Fe could likewise be explained by its formation from metal-rich magmatic-dominated hydrothermal fluids following a brecciation/dilation event. The variability of Fe contents in stage IV sphalerite can be explained by a system with variable magmatic-to-meteoric fluid ratios.

Murakami & Ishihara (2013) reported that Cd is positively correlated with Fe in sphalerite from the Huari Huari and Cerro Rico de Potosi deposits which have average Cd concentrations of 2,840 ppm and 1,500 ppm Cd, respectively. They argued that this was the result the coupled substitution of Cd and Fe for Zn ($Fe^{2+} + Cd^{2+} \leftrightarrow 2Zn^{2+}$). Cook *et al.* (2009), in their study on the composition of sphalerite in various deposit types, instead found that Cd was negatively correlated with Fe and argued that it had substituted directly for Zn ($Cd^{2+} \leftrightarrow Zn^{2+}$). Consistent with the findings of Cook *et al.* (2009), Fe and Cd are negatively correlated in the CZ suggesting that Cd may have directly substituted for Zn (Fig. 5).

The Cd enrichments observed in the tan layers may be related to fractionation of the ore fluid. The ionic radius of Cd (IV) (0.78 pm: Shannon 1976) is much larger than that of Zn and thus

Cd should be incompatible in sphalerite. Due to its incompatibility, the activity of Cd in the ore fluid could have been characterized by an enrichment relative to Zn and Fe towards the end of each depositional cycle. Tan layers with high Cd concentration may thus indicate formation in a closed system with a fractionating hydrothermal fluid.

The concentration of In in sphalerite from deposits in the Andean Tin Belt is highly variable. Murakami & Ishihara (2013) reported that sphalerite from the Cerro Rico de Potosi and Huari Huari deposits have average In concentrations of 430 ppm and 3,450 ppm, respectively. Within these deposits, In in sphalerite is generally positively correlated with Fe. High-Fe sphalerites from the Huari Huari deposit have approximately 1:1 In:Cu ratios and Murakami & Ishihara (2013) argue this indicates that In and Cu substitute for Zn *via* a coupled substitution (i.e., $Cu^{+} + In^{3+} \leftrightarrow 2Zn^{2+}$). The ionic radius of In (IV) is 0.62 pm (Shannon 1976), similar to that of Zn (0.60 pm: Shannon 1976), but its higher ionic charge may make it incompatible in sphalerite by direct ion exchange for Zn.

The data for In show that it behaves differently than both Fe and Cd. In stage II sphalerite, In is generally more enriched in the tan sphalerite (average: 2.53 ppm) than the dark brown sphalerite (average: 0.10 ppm) suggesting a possible negative correlation with Fe. The LA-ICP-MS traverses in Figure 5 show that In is locally negatively correlated with Fe, however, the correlation is not wholly consistent. The correlation, where present, may be explained by its incompatibility in sphalerite in a manner similar to that for Cd. Where the correlation is not present, the activity of In in the fluid may have been affected by its sequestration in some other mineral. The sphalerite from stage III shows the highest enrichments in In amongst all the sphalerites examined, with an average on 2,258 ppm. This value is consistent with the In concentrations observed in the Huari Huari deposit by Murakami & Ishihara (2013). Murakami & Ishihara (2013)

demonstrate that the Cu:In ratios are ~1:1, providing evidence for the coupled substitution of Cu and In for Zn. No strong correlation between In and Cu has been documented for sphalerite from the CZ. The elevated In levels in stage III sphalerite could be related to dilution effects since sphalerite is present in only minor amounts.

The data for the dark-brown sphalerite from all stages show elevated concentrations of Ag, Cu and Sn. This is similar to the findings of Murakami & Ishihara (2013) in the dark (Fe-enriched) patches within low-Fe sphalerite from the Toyoha and Potosi deposits; these authors attributed the elevated values to inclusions of stannite. In other studies, Cu is frequently observed in high quantities and has been attributed to sub-micron inclusions of chalcopyrite in the form of chalcopyrite disease (chalcopyrite disease: Bortnikov *et al.* 1991) (Cook *et al*. 2009). Within dark brown sphalerite of stage II, Ag and Cu are correlated positively (Fig. 12a, b: $R^2 = 0.97$). The line of best-fit for this data approximates a 2:1 Ag:Cu ratio. These elements could reflect the presence of micro-inclusions of minerals such as the pirquitasite-stannite solid solution.

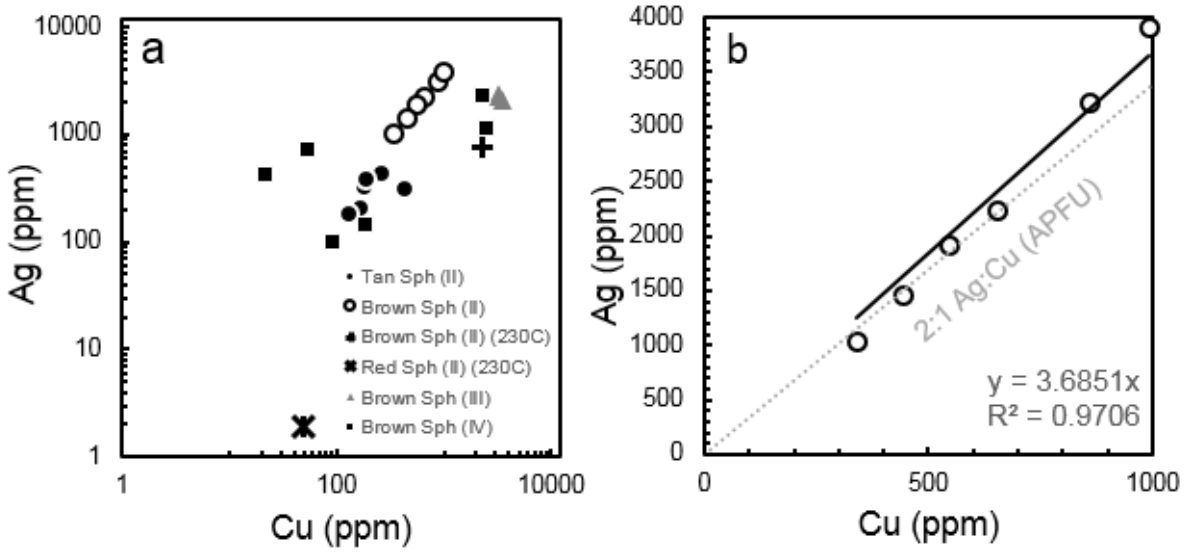

Figure 12: Bivariate plots of Ag *vs.* Cu from LA-ICP-MS spot analyses. (a) All data. Note that analyses from brown sphalerite of stage II [brown sph (II)] plot approximately along a linear trend. (b) Ag *vs*. Cu showing only the data for brown sphalerite of stage II. Here Ag and Cu show a good correlation ($R^2 = 0.97$). The slope of the line of best fit is very close to a 2:1 Ag:Cu ratio.

Evidence for As-bearing sphalerite is rare in the literature. Cook *et al.* (2009), in their study sphalerite compositions by LA-ICP-MS indicate As values in the hundreds of ppm for samples from a strata-bound deposit in Mexico. Clark (1970) gave an example of sphalerite with 1.7 ± 0.2 wt. % As from Chile as determined by EMPA and attributed the enrichment to solid solution. The data show that the sphalerite in the CZ is variably enriched in As including stage III sphalerite with an average of 3.2 wt. % As but, these high concentrations can most likely be attributed to the presence of mineral inclusions. For example, in sphalerite from stages II and III, inclusions of fine- to coarse-grained arsenopyrite are abundant. Furthermore, in stage II sphalerite, the mineral proustite occurs with galena (Fig. 9a). Although not distinguished in data from the LA-ICP-MS time series, there is evidence to suggest that most of the As occurs as micro-inclusions of proustite and arsenopyrite. A plot of Ag *vs.* As for stage II sphalerite shows a positive correlation with two trends (Fig. 13a). The more shallow trend is very similar to the Ag:As ratio in proustite suggesting that Ag and As are hosted in proustite inclusions. The steeper trend could be the result of some other mineral inclusion such as arsenopyrite. A plot of Pb *vs*. Ag for sphalerite from stage II shows a similar positive correlation; this may indicate that galena is present with the Ag and As minerals (Fig. 13b).

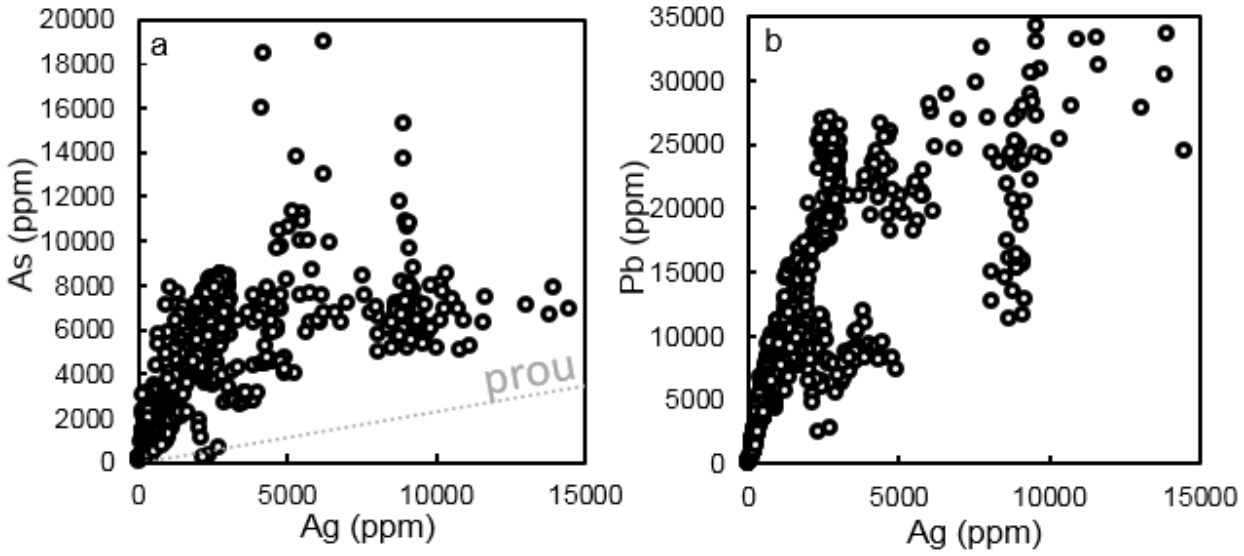

Figure 13: Biavariate plots for LA-ICP-MS data corresponding to traverse "a-a'" in Figure 5. (a) Ag versus As. The data shows a positive correlation with two trends. The more shallow trend has the same As:Ag ratio as proustite (prou) which is plotted as a grey dotted line. (b) Ag versus Pb. The data show a positive correlation.

Pyrite

The composition of pyrite, often in conjunction with S isotopic studies, has been used to investigate changes in fluid conditions in hydrothermal systems (e.g., Barrie *et al.* 2009b, Large *et al.* 2009, Agangi *et al.* 2013, Maydagán *et al.* 2013, Reich *et al.* 2013, Genna & Gaboury 2015). The mechanisms by which minor- and trace-elements are incorporated into pyrite are not fully understood. Various studies use correlations between elements to argue that they most likely were incorporated *via* coupled substitutions. For example, Chouinard *et al.* (2005), using data from EMPA and secondary-ion mass spectrometry (SIMS), interpreted such correlations in pyrite from the Pascua epithermal deposit, Chile-Argentina. They showed that Ag, As and Cu were most likely incorporated *via* coupled substitutions for Fe ($Ag^{+} + As^{3+} \leftrightarrow 2Fe^{2+}$ and $Cu^{+} + Au^{3+} \leftrightarrow 2Fe^{2+}$) and argued that it would have been local REDOX conditions that dictated which substitutions may have occurred. Simon *et al.* (1999), using XANES measurements on Au-bearing pyrite from the Twins Creek Carlin-type Au deposit, Nevada, United States of America showed that As is present

as As^- and is probably concentrated in angstrom-scale layers with a marcasite or arsenopyrite structure.

The spatial-coupling of elements in pyrite is clear from the compositional maps (Fig. 7). These couplings, when combined with LA-ICP-MS time-series plots (Fig. 8) and observations on morphology and thickness of the growth zones, provide a record of the evolving conditions of the ore-forming system. For example, both As and Cu are spatially related in the pyrite grains. The LA-ICP-MS time series show smooth counts for As, suggesting it is structurally bound in pyrite; if accurate, this implies that As existed in a reduced state (As^-) where it has substituted for S^{2-}. The time-series plots for Cu are irregular in the pyrite core, but less so in the second growth zone suggesting that the Cu may occur both within mineral inclusions and the within structure of the pyrite. One could speculate that the incorporation of As could have facilitated the incorporation of some Cu. There is an apparent correlation between the counts for Cu, Zn and Cd in the pyrite core, suggesting that most of the Cu could occur with or in inclusions of sphalerite.

Silver, Sb and Pb are spatially related and occur together in discrete layers that are < 20 µm thick. The LA-ICP-MS time-series plots for these elements are irregular (Fig. 8) and correlate well with one another, suggesting they predominantly occur in inclusions of Ag-Sb-Pb-bearing minerals such as sulfosalts and/or galena. From the time-series data, it is apparent that Sn roughly correlates with these elements and may occur with the sulfosalts or galena. The counts for Sb are smoother than those for Ag and Pb suggesting that some Sb is incorporated into the pyrite structure. The narrow discrete layers with patchy Ag-Sb-Pb enrichments occur at the onset of growth zones 1, 2 and 3 indicating that these growth cycle began with the deposition of Ag-Sb-Pb minerals.

Gold, Ni, Co and to some extent Bi are spatially related and occur together in discrete layers which do not always correlate with those of Ag, Sb and Pb. The LA-ICP-MS time-series

plots for these elements are irregular, suggesting they occur in mineral inclusions. The enrichments in Au of up to ~4 ppm in the rim does not correlate with As or Cu, limiting the likelihood that Au is structurally bound in pyrite *via* a coupled substitution with these elements.

The concentric-growth zones as well as the rim are not of constant widths around the entire grain. This observation, in conjunction with the rounded morphology of some growth zones, suggests that they may have formed either as colloform-textured layers or as cubic layers which have been partially resorbed. In stage V mineralization, colloform pyrite and marcasite are common. Slater *et al.* (in prep.) interpreted this texture to have formed by undercooling during either boiling or fluid mixing. Rapid crystal growth can enable pyrite to sequester greater amounts of minor- and trace-elements (Chouinard *et al.* 2005). In light of this, the elevated As abundances, interpreted as being held within the structure of pyrite, could be explained by rapid crystal growth during undercooling. The near end-member euhedral pyrite core and possibly the cubic growth zone 3 may have thus formed during periods of quiescence during which slower rates of crystal growth would be expected. Conversely, the growth zones 1 and 2 and the rim may have formed during periods of boiling or fluid mixing which facilitated rapid pyrite growth and the deposition of precious- and base metals. The periods of quiescence and boiling/mixing are consistent with the proposed formation model whereby the system was episodically opening and closing.

Sulfosalt Textures and P-T-X Considerations

The conditions of ore formation are recorded in the primary mineral assemblages and their textures. However, the recognition that some of the observed mineral assemblages are unlikely to be primary makes inferring the ore forming conditions more challenging. For example, some of the textures described in this study resemble emulsion as described by Ramdohr (1969). One common example of an emulsion-like texture consists of blebby inclusions of a “guest” phase

occurring in a more abundant "host" phase (Fig. 14a). In cases where the guest is in approximately equal proportions to the host, the guest and host appear intergrown (Fig. 14b). Keigh & Honea (1969) in their experimental work on the Ag-Sb-S system produced emulsion-like sulfosalt intergrowths similar to those shown in Figure 14b. This was done by progressively cooling sulfide glass having compositions intermediate between pyrargyrite and miargyrite and thus suggests that these type of textures could be the result of unmixing during cooling.

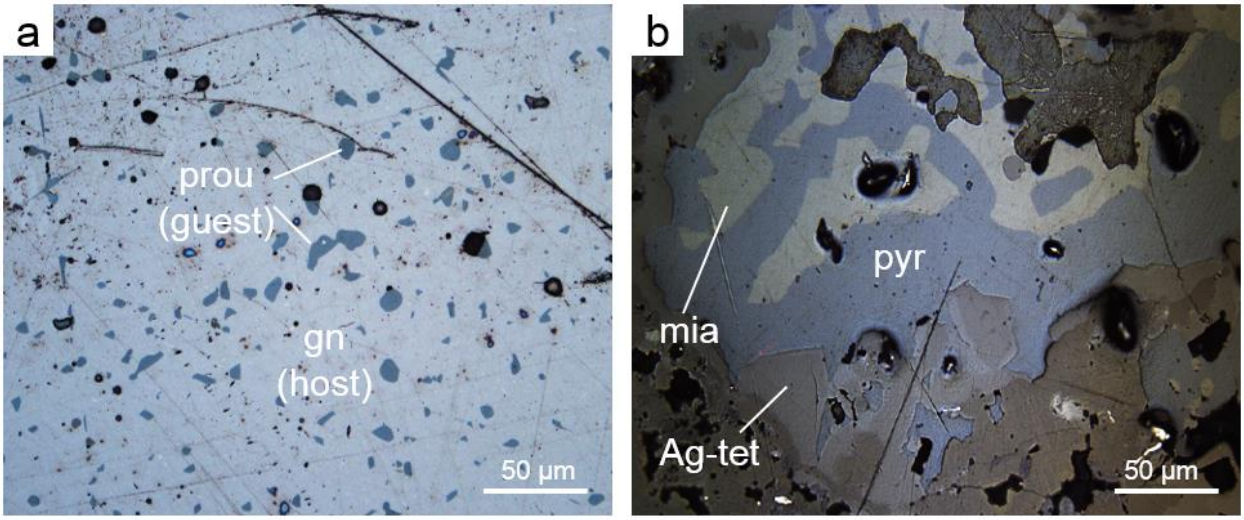

Figure 14: Reflected-light images of emulsion-like textures. (a) Galena (gn) grain that contains blebby inclusions of proustite (prou). Here galena is acting as the host and proustite is acting as the guest. (b) Convoluted intergrowth of miargyrite and pyrargyrite encased by Ag-bearing tetrahedrite.

The observed pavonite (?) + galena assemblage (Fig. 9g), coupled with the presence of micro-inclusions of galena in pavonite interpreted from the EMPA data, could be explained by unmixing from a galena solid solution (Gn_{ss}). High-temperature galena has been shown to incorporate significant quantities (i.e., tens of mole %) of Ag and Bi (Wernick 1960, Vanhook 1960, Hoda & Chang 1975), possibly by solid solution with the high-temperature cubic form of $AgBiS_2$ (*i.e.*, schapbachite: Staude *et al.* 2010). In the PbS-$AgBiS_2$ system, the Gn_{ss} unmixes below 220 ºC to form stoichiometric galena and the trigonal form of $AgBiS_2$ (matildite) (Van Hook 1960).

The exsolved matildite may have been then converted to pavonite by removal of Ag_2S. Retrograde equilibration of a high-temperature Gn_{ss} during cooling is a possible mechanism that could have led to the observed pavonite + galena assemblage.

The blebby inclusions of proustite in stage II galena (Figs. 9a, 14a) could be explained by emulsion from a Gn_{ss}, but also by co-precipitation. Little published work has addressed the extent to which As can be incorporated into Gn_{ss} which thus limits our assessment of the former interpretation. Goodell (1975) summarizes what is known of the ternary Ag_2S-PbS-As_2S_3 system based on reported assemblages from other studies. No solid solution and few assemblages have been reported for this system (Goodell 1975). Smithite ($AgAsS_2$) is the As analogue of miargyrite ($AgSbS_2$) (Razmara & Pattrick 2011). Hall (1966) reported a cubic form of $AgAsS_2$ that crystallizes between 415 °C to 421 °C in the Ag-As-S system, although subsequent studies failed to confirm the presence of cubic $AgAsS_2$ (Roland 1970, Bryndzia & Kleppa 1989, Razmara & Pattrick 2011). Arsenic might be able to incorporate into galena through substitution when coupled and charge-balanced with Ag in a manner similar to that of Sb ($As^{3+} + Ag^{+} \leftrightarrow 2Pb^{2+}$), resulting in Ag-As-bearing galena. Furthermore, if the cubic $AgAsS_2$ exists, as suggested by Hall (1966), then $AgAsS_2$ may be able to incorporate into a high-temperature Gn_{ss}. Regardless of whether Ag and As entered the structure of galena as a solid solution or substitution, a precursor high-temperature Ag-As-bearing galena could have broken down to release the Ag and As and that these could have then diffused and recombined to form the observed proustite inclusions. This interpretation is favoured over that of co-precipitation of proustite and galena in colloform sphalerite. If proustite formed as a primary mineral, then it should have been observed forming some inclusions in sphalerite with no galena; however this was not observed. The exploratory heating experiments performed in this study produced a third, unidentified phase between the proustite inclusions and

the galena at 300 °C, which is below the T interpreted for the system (>320 °C: Slater *et al.* in prep). The result of this heating experiment is treated with caution due to the potential for metastable reactions and the sluggish behaviour of solid-state reactions.

The veins containing the assemblage galena + jordanite ± boulangerite formed as part of stage III mineralization. The experimental work on the binary and ternary systems with Pb-Sb-As-S provide useful information for interpreting these mineral assemblages and their textures. Craig et al. (1973), in their investigation into the Pb-Sb-S system, synthesized a Gn_{ss} in equilibrium with boulangerite and another Pb-Sb-S phase, demonstrating that galena and boulangerite can co-exist in the simple binary system. Jordanite is the As-dominant end-member of the jordanite-geocronite solid solution series ($Pb_{14}(As,Sb)_6S_{23}$: Biagioni et al. 2016). Roland (1968) performed experiments on the Pb-As-S system to determine the stability of jordanite at relatively high-temperature (>500 °C), but also at lower temperature (300 °C to 250 °C) to determine where jordanite undergoes a structural change to form the low-temperature trigonal dimorph, gratonite. Roland (1968) determined that the dimorphic transformation occurs at some temperature below 250 °C. Ramdohr (1955) noted the assemblages galena + gratonite and galena + jordanite (possibly containing some Sb) and proposed that the low-temperature alteration of geocronite could have produced a mixture of boulangerite + galena. The observed assemblages of jordanite + galena and jordanite + galena + boulangerite in the CZ (Figs. 9b, 10) are consistent with the alteration of jordanite to form boulangerite + galena, leaving some residual jordanite. Walia & Chang (1973) in their experimental studies of the PbS-Sb_2S_3-As_2S_3 system, observed that boulangerite was only stable when As_2S_3 contents were low. Therefore, an increase in the Sb:As ratio in the system could have destabilized jordanite and led to the formation of boulangerite.

The main stage of Ag mineralization (stage III) as well as a later subordinate stage (stage VI) are dominated by the mineral assemblage Ag-bearing tetrahedrite, miargyrite, pyrargyrite, (± kesterite) and sphalerite. Locally, a Ag-Sb-Pb-S phase may be present exclusively as an intergrowth with miargyrite. The intergrowth of pyrargyrite + miargyrite appears to be separate from the intergrowth of Ag-bearing tetrahedrite and sphalerite (Fig. 9c, d and Fig. 14b). This suggests that the four minerals unmixed from two precursor minerals. Heating of a sample of this assemblage to 250 ºC produced no noticeable changes; however, heating to 300 °C for 8 hrs caused the boundary between miargyrite and pyrargyrite to become diffuse which may represent the onset of homogenization between the phases. At the same time, no apparent homogenization between the Ag-bearing tetrahedrite and the Ag-Sb-sulfosalts was observed. Figure 15 illustrates the proposed formational model for this mineral assemblage. Here, an inferred primary ore assemblage consisting of predominantly of an Ag-Zn-Sb-Sn-Cu-bearing and an Ag-Sb-Pb-S-bearing phase was deposited. Subsequent changes to the P-T-X conditions, such as cooling to below 300 °C, could have caused the Ag-Sb-Pb-S phase to unmix into pyrargyrite + Pb-bearing miargyrite. Further cooling could have caused the unidentified Ag-Sb-Pb-S phase to separate from the miargyrite. At some point, sphalerite and possibly kesterite may have unmixed from the Ag-Zn-Sb-Sn-Cu-bearing phase.

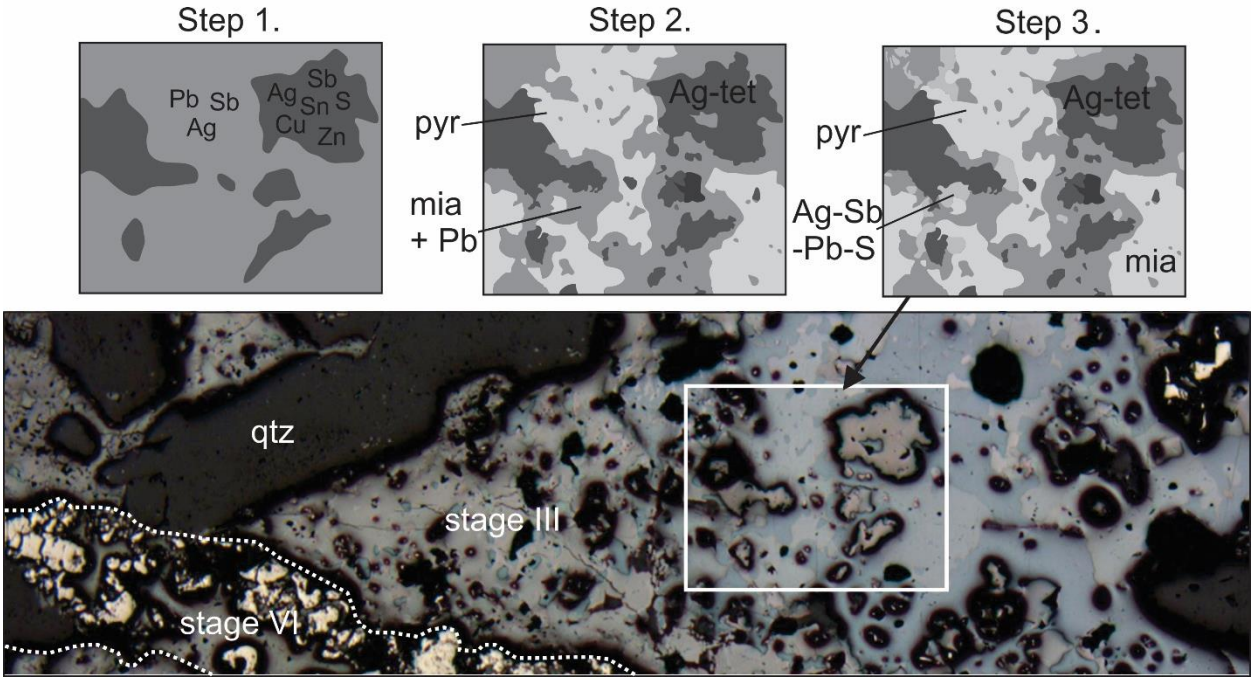

Figure 15: Schematic diagram illustrating the stepwise unmixing of miargyrite (mia), pyrargyrite (pyr), an unidentified As-Sb-Pb-S phase (Ag-Sb-Pb-S) and Ag-bearing tetrahedrite (Ag-tet) from a precursor mineral assemblage. The lower image is a photomicrograph of stage III Ag-rich mineralization under plane polarized reflected light.

The occurrence of Ag-bearing tetrahedrite in the samples analyzed in this study allows for the integration of a vast amount of literature on the mineral and the conditions at which it forms. For example, Ag-bearing varieties of the tennantite-tetrahedrite series, collectively referred to as "fahlore", are common within Ag-deposits and are major components of Ag-ores globally (Sack *et al.* 2003). The *fahlore* geothermometer, recently improved upon by Sack & Lichtner (2009), has been refined and applied as a petrogenetic indicator for polymetallic Ag-bearing meso-epithermal systems (Sack 2000, Sack & Goodell 2002, Sack et al. 2003, Sack 2005, Sack & Ebel 2006, Sack & Lichtner, 2009). It relies on the stoichiometric ratios of Ag/(Ag+Cu) and Zn/(Zn+Fe) in Ag-bearing *fahlore* which define isotherms between 170 °C and 400 °C. The isotherms have been calculated based on the maximum solubility of Ag in *fahlore* (fah) in the Ag_2S-Cu_2S-ZnS-Sb_2S_3 system that is controlled by its reaction with pyrargyrite (pyr), sphalerite (sph) and miargyrite (mia) (Sack & Lichtner 2009):

$$Ag_{10}Zn_2Sb_4S_{13}\ (fah) = 3Ag_3SbS_3\ (pyr) + 2ZnS\ (sph) + AgSbS_2\ (mia)$$

The phase relations for the Ag_2S-Cu_2S-ZnS-Sb_2S_3 system in equilibrium with sphalerite predict a stable assemblage of Ag-bearing tetrahedrite, miargyrite and pyrargyrite at 300 °C (Fig. 16). In order for this geothermometer to be valid, it must be demonstrated petrographically that Ag-bearing tetrahedrite, miargyrite, pyrargyrite, and sphalerite were quenched while in equilibrium with each other.

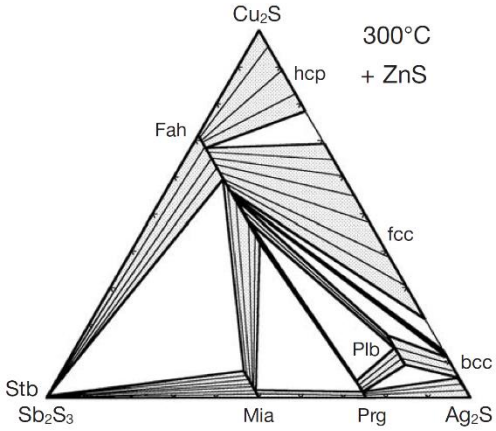

Figure 16: Equilibrium assemblages in the Ag_2S-Cu_2S-Sb_2S_3 system that is saturated with sphalerite from Sack (2005). Stb – stibnite, Mia – miargyrite, Fah – fahlore, Prg – pyrargyrite, hcp, fcc, and bcc – closed packed, face-centered cubic, and body-centered cubic $(Ag,Cu)_2S$ solid solutions, plb – polybasite.

Application of this geothermometer suggests that stage III mineralization equilibrated at 245 °C ± 15 °C whereas stage VI mineralization equilibrated at 270 °C ± 10 °C. These temperatures are consistent with the result of the heating experiment on stage III mineralization that suggested the miargyrite and pyrargyrite unmixed at temperatures between 250 °C and 300 °C. The temperatures determined by sulfosalt thermometry are interpreted here as representing the temperature at which the minerals were quenched and not the temperature of Ag deposition. Therefore, the temperatures of 245 °C ± 15 °C and 270 °C ± 10 °C are interpreted as minimum temperatures of formation for the Ag-rich stages III and VI respectively. The somewhat refractory

nature of *fahlore* allows it to preserve a record its formation temperature when other phases may have undergone significant re-equilibration (Sack & Ebel, 2006). The increase in temperature from 245 °C ± 15 °C in stage III to 270 °C ± 10 °C in stage VI may be real and represent a heating trend.

A common feature of pirquitasite in stage VII mineralization is that it contains exsolution lamellae of stannite (Fig. 9e). This exsolution has not been reported on extensively in the literature but was documented by Johan & Picot (1982) in samples from the Pirquitas Mine. There have been several studies on kesterite-stannite exsolution that may provide a useful analogue in terms of understanding the texture that is observed here (Harris & Owens 1972, Springer 1972, Petruk 1973, Hall *et al.* 1978). At the Snowflake mine, British Columbia, Canada, examples of stannite (Cu_2FeSnS_4) lamellae in kesterite (Cu_2ZnSnS_4), considered to be the products of exsolution, have been observed. Springer (1972) showed this was the result of a structural change in the Fe-rich end-member stannite which undergoes a polymorphic transformation from α-Cu_2FeSnS_4 to β-Cu_2FeSnS_4 below 680 °C and developed a geothermometer based on the transformation. Petruk (1973) applied and improved upon the geothermometer to study Sn-minerals from the Mount Pleasant W-Mo-Bi-Sn mine, New Brunswick, Canada with some success. The exsolution of stannite from pirquitasite could have occurred in a similar manner by the temperature-dependant polymorphic transformation of α-Cu_2FeSnS_4 to β-Cu_2FeSnS_4 which may have made it immiscible in pirquitasite. The absence of observed stannite exsolution lamellae in the Fe-rich member hocartite is consistent with this interpretation as it too may have undergone a similar transformation. Heating of a sample with apparent pirquitasite-stannite exsolution to 300 °C did not produce homogenization of the minerals. This null result under dry conditions and without a flux was most probably due to slow reaction rates. Similar heating experiments performed by

Springer (1973) showed that homogenization took longer than three months at 300 °C without the addition of a flux.

Canfieldite and a Te-bearing variety of canfieldite are observed in close association with galena in stage VII and in mineralization of an unknown stage. The occurrence of galena intergrown with canfieldite, often occurring encased in pirquitasite (Fig. 9e, f), may represent a mineral assemblage which unmixed from a precursor phase. Likewise, the Te-bearing canfieldite with blebby inclusions of galena, often encased in cassiterite, may have formed by unmixing. The precursor to these minerals may have been Pb-bearing (telluro-)canfieldite. Lead may have incorporated into in canfieldite at relatively high temperatures and unmixed following some P-T-X change. Alternatively, a different precursor mineral, possibly with Ag, Pb and Te, may have destabilized by the introduction of Sn. Evidence for this is in the presence of cassiterite and pirquitasite which have overgrown the canfieldite and galena intergrowths, suggesting an increase in the activity of Sn.

Implications for the Formation of Ores

The dynamic nature of the hydrothermal system that formed the rich mineralization at the CZ is reflected in the chemistry and textures of ore samples. A record of the ore-forming processes, particularity the episodic opening and closing of the hydrothermal system, may remain within the Fe and Cd contents of sphalerite layers. Furthermore, using the colour of sphalerite as a proxy for Fe content enables one to see this record by a simple visual observation of ore samples. Although, the examined pyrite was from a paragenetic stage not associated with high-grade Ag or Zn mineralization, the same ore-forming processes are apparently recorded in the concentric growth zones. The presence of micro-inclusions of sulfosalts observed in the LA-ICP-MS maps and time-

series plots reveal that the system was episodically saturated with respect to elements such as Ag, Pb and Sb even though large amounts of these elements were not deposited.

The sulfosalt assemblages and their textures record possibly drastic changes in the P-T-X conditions of the hydrothermal system. Of particular relevance to the study of ore deposits is the interpretation that most of the sulfosalts that constitute the ore-bearing samples are not part of the primary ore assemblages, but rather, are products of unmixing caused by changes in P-T-X conditions. The re-equilibration can most simply be explained by overprinting of the primary mineral assemblages by lower-temperature assemblages during cooling.

Studies on the chemistry of galena show that some Ag, Sb, Bi and Cu in hydrothermal ore deposits originated in high-temperature galena (Hall & Czamanskem 1972, Foord *et al.* 1988, Foord & Shawe 1989, Sack *et al.* 2002, Sack & Goodall 2002, Chutas & Sack 2004, Gamarra-Urrunaga *et al.* 2013). Taking this hypothesis further, experimental work has shown that potentially all of the Ag in some Ag deposits could have originated in galena (Chutas et al. 2008). The relationships between sulfosalts and galena in some paragenetic stages of the CZ suggest that at least some of the Ag did originate in galena which unmixed to form various sulfosalts upon retrograde cooling. It may also be relevant to note that the elements which have been shown to incorporate readily into galena such as Ag, Sb, Bi and Cu are the dominant constituents of the high-grade Ag mineralization observed in this study. The retrograde breakdown of a reservoir of high-temperature Ag-Sb-Bi-(Cu-)bearing galena at depth could be invoked to explain some of the observed sulfosalt assemblages where the documented textures are inconsistent with *in situ* unmixing from galena. The hypothetical precursor galena could have formed during stage II, the most galena rich-stage of the paragenesis. In a similar fashion, Gamarra-Urrunaga *et al.* (2013) argued for the probable existence of a precursor Ag-bearing galena at the intermediate-sulfidation

Pallancata deposit in Peru. They inferred that there could be an additional resource of Ag at depth below the Pallancata deposit, an interpretation which could also be applied to the CZ.

Conclusions

In all of the paragenetic stages studied here (II, III, IV, V, VI and VII) the dynamic nature of the ore-forming system is evident. Here, the key conclusions regarding sphalerite and pyrite textures and chemistry are presented first, followed by those for sulfosalt textures and assemblages.

1. The genetic model for the CZ developed by Slater et al. (in prep.) in which ores formed during episodic opening and closing of the system may be recorded in the compositions and textures of sphalerite.
    a. The Fe and Cd contents in colloform sphalerite of paragenetic stages II and IV are negatively correlated. The Fe-rich dark brown sphalerite layers are interpreted to have formed from a magmatic-dominated fluid that had flashed to steam. The Cd-rich tan sphalerite layers may have formed from a fractionating fluid as the system became sealed by ore and gangue minerals. Cadmium, having a larger ionic radius than Zn and Fe, may have been relatively incompatible in sphalerite.
    b. Indium concentrations in the sphalerite are generally low (several ppm) except for sphalerite of stage III which has an average of 2,258 ppm. In the colloform sphalerite of stage II, In is slightly enriched in the tan Cd-rich layers (avg.: of 2.53 ppm In) and depleted in the dark brown Fe-rich layers (avg.: 0.10 ppm In). Although In and Zn have similar ionic radii, its higher charge may have made it incompatible in sphalerite. Thus, In may have been enriched in the tan sphalerite layers due to fluid fractionation as the system became sealed. Although other studies have found a positive correlation between Cu and In, suggesting a coupled

substitution for Zn (Cu^{+} + In^{3+} ↔ Zn^{2+}: Cook *et al.* 2009, Murakami & Ishihara 2013), no such correlation was found here. The variability of In concentrations between genetic stages could be explained by dilution effects or its sequestration in other minerals.

2. The evolution of the ore system is recorded in the composition and morphology of concentric growth zones in pyrite from stage V. Euhedral near-endmember cores and cubic growth zones in the pyrite grains are interpreted to represent periods of quiescence, slow crystal growth and a closed system. Rounded growth zones which contain elevated levels of minor- and trace-elements are interpreted to represent periods of boiling or fluid mixing, rapid crystal growth and an open system. Maps derived from LA-ICP-MS analyses of concentrically zoned pyrite grains show the spatial coupling of:
    a. As-Cu: Arsenic appears to be structurally bound in the pyrite having substituted for S. Cu appears to occur principally as mineral inclusions such as chalcopyrite but some may be structurally bound in the pyrite. The spatial relationship between As and Cu suggest that the two elements may have entered the pyrite together but, the exact mechanism is unclear.
    b. Ag-Sb-Pb: These elements are bound in micro-sulfosalt inclusions, possibly along with galena. The relatively smooth time-series plots created from the raw LA-ICP-MS count data for Sb suggests that some Sb may be structurally bound in the pyrite as well.
    c. Au-Ni-Co(-Bi): These elements likely occur in discrete layers with mineral inclusions. The LA-ICP-MS maps show no spatial correlation between Au and As

or Cu suggesting that it did not enter the structure of pyrite by coupled substitutions with these elements.

3. The modal distribution, species type and textures of sulfosalts and their assemblages provides insight into the formation and modification of Ag-rich ores. Many of the observed assemblages are interpreted to be secondary, having unmixed from the primary assemblages during retrograde re-equilibration with a cooling hydrothermal system.
    a. pavonite + galena (undetermined stage): These minerals are interpreted to have unmixed from a high-temperature PbS-$AgBiS_2$ solid solution upon cooling.
    b. galena + proustite (stage II): These minerals are interpreted to have unmixed from a high-temperature Ag-As-bearing galena upon cooling.
    c. galena + jordanite ± boulangerite (stage III): The assemblage consisting of the intergrowth of galena + jordanite may have become destabilized by an increase in the activity of Sb relative to that of As. This change may have resulted in formation of boulangerite + galena. The change in fluid chemistry could possibly have arisen by the breakdown of high-temperature PbS-$AgSbS_2$ solid solutions at depth.
    d. Ag-bearing tetrahedrite + miargyrite + pyrargyrite + sphalerite ± kesterite ± Ag-Sb-Pb sulfosalt (stages III and VI): The polymetallic mineral assemblage is the principal host for high-grade Ag mineralization. The assemblage is thought to have formed by the stepwise unmixing of two intergrown precursor phases: a Ag-Sb-Pb-S-bearing phase and a Ag-Zn-Sb-Sn-Cu-bearing phase. The Ag-Sb-Pb-S-bearing phase unmixed to form pyrargyrite and Pb-bearing miargyrite which is thought to have occurred between 250 ºC and 300 ºC based on heating experiments. The Pb-bearing miargyrite subsequently unmixed further to form stoichiometric miargyrite

and an unidentified Ag-Sb-Pb-S-bearing phase. The Ag-Zn-Sb-Sn-Cu-bearing phase may have unmixed to form Ag-bearing tetrahedrite, kesterite and sphalerite. Fahlore geothermometry indicates that stage III mineralization equilibrated at 245 °C ± 15 °C whereas stage VI mineralization equilibrated at 270 °C ± 10 °C. These temperatures are interpreted as the minimum temperatures for the primary Ag mineralization.

e. pirquitasite + stannite (stage VII): Lamellae of stannite in pirquitasite are interpreted as an exsolution product. The temperature dependent polymorphic transformation of α-Cu_2FeSnS_4 to β-Cu_2FeSnS_4 documented by Harris & Owens (1972), Springer (1972), Petruk (1973) and Hall *et al.* (1978) may have produced immiscibility of the two minerals. This is interpreted to have occurred during retrograde re-equilibration during cooling.

f. (Te-bearing) canfieldite + galena: This mineral assemblage is interpreted as having unmixed from a precursor phase. The precursor may have been an Ag-Pb-S-(Te)-bearing phase which destabilized by the introduction of Sn to form (Te-bearing) canfieldite and galena but may also have been a Pb-(Te-)bearing canfieldite.

References

Agangi, A., Hofmann, A., & Wohlgemuth-Uuberwasser, C.C. (2013) Pyrite zoning as a record of mineralization in the Ventersdorp contact reed, Witwatersrand Basin, South Africa. *Economic Geology* **108**, 1243-1272.

Awadh, S.M. (2009) Iron content variations in sphalerite and their effects on reflectance and internal reflections under reflected light. *Arab Journal of Geoscience* **2**, 139-142.

Banno, S. (1988) On the sphalerite geobarometer. *Geochemical Journal* **22**, 1-129.

Bahlburg, H. (1990) The Ordovician Puna basin in the Puna in the NW Argentina and N Chile: Geodynamic evolution from back-arc to foreland basin. *Geotektonische Forschungen* **75**, 1-107.

Barrie, C.D., Boyce, A.D., Boyle, A.P., Williams, P.J., Blake, K., Wilkinson, J.J., Lowther, M, McDermott, P., & Prior, D.J. (2009a) On the growth of colloform textures: a case study of sphalerite from the Galmoy ore body, Ireland. *Journal of the Geological Society* **166**, 563-582.

Barrie, C.D., Boyce, A.D., Boyle, A.P., Williams, P.J., Blake, K., Ogawara, T., Akai, J., & Prior, D.J. (2009b) Growth controls in colloform pyrite. *American Mineralogist*, **94**, 415-429.

Biagioni, C., Dini, A., Orlandi, P., Moële, Y,. Pasero, M., & Zaccarini, F. (2016) Lead-antimony sulfosalts from Tuscany (Italy). XX. Members of the jordanite–geocronite series from the Pollone mine, Valdicastello Carducci: Occurrence and Crystal Structure. Minerals 6, 1-15.

Bortnikov, N.S., Genkin, A.D., Dobrovol'skaya, M.G., Muravitskaya, G.N., & Filimonova, A.A. (1991) The nature of chalcopyrite inclusions in sphalerite: Exsolution, coprecipitation, or "disease"? *Economic Geology* **86**, 1070-1082.

Bryndzia, L.T., & Kleppa, O.J. (1989) Standard molar enthalpies of formation of sulfosalts in the Ag-As-S system and thermochemistry of the sulfosalts of Ag with As, Sb and Bi. *American Mineralogist* **74**, 243-249.

Caffe, P.J., Soler, M.M., Coira, B.L., Onoe, A.T., & Cordani, U.G. (2008) The Granada ignimbrite: A compound pyroclastic unit and its relationship with Upper Miocene caldera volcanism in the northern Puna. *Journal of South American Earth Sciences* **25**, 464-484.

Chouinard, A., Paquette, J., & William-Jones, A.E. (2005) Crystallographic controls on trace-element incorporation in auriferous pyrite from the Pascua epithermal high-sulfidation deposit, Chile-Argentina. *The Canadian Mineralogist* **43**, 951-963.

Chutas, N.I., & Sack, R.O. (2004) Ore genesis at la Colorado Ag-Zn-Pb deposit in Zacatecas, Mexico. *Mineralogical Magazine* **68**, 923-937.

Chutas, N.I., Kress, V.C., Ghiorso, M.S., & Sack, R.O. (2008) A solution model for high-temperature PbS-$AgSbS_2$-$AgBiS_2$ galena. *American Mineralogist* **93**, 1630-1640.

Clark, A.H., (1970) Arsenian sphalerite from Mina Alacrán, Pampa Larga, Copiapó, Chile. *American Mineralogist* **55**, 1794-1794.

Coira, B., Caffe, P., Ramírez, A., Chayle, W., Díaz, A., Rosas, S., Pérez, A., Pérez, B., Orozco, O., & Martínez, M. (2004) Programa nacional de cartas geológicas de la República Argentina: Hojas Geológica 2366-I/2166-III. *Instituto de Geológía y Recursos Minerales, Servicio Geológico Minero Argentino* **Boletín 269,** 1-125.

Cook, N.J., Ciobanu, C.L., Pring, A., Skinner, W., Shimizu, M., Danyushevsky, L., Saini-Eidukat, B., & Melcher, F. (2009) Trace and minor elements in sphalerite: A LA-ICP-MS study. *Geochemica et Cosmochimica,* **73**, 4761-4791.

Craig, J.R., Chang, L.L.Y., & Lees, W.R. (1973) Investigations in the Pb-Sb-S system. *Canadian Mineralogist* **12**, 199-206.

Foord E.E., Shawe, D.R., Conklin, N.M., (1988) Coexisting galena, PbS_{ss} and sulfosalts: Evidence for multiple episodes of mineralization in the Round Mountain and Manhattan Gold districts, Nevada. *Canadian Mineralogist* **26**. 355-376.

Foord, E.E., & Shawe D.R. (1989) The Pb-Bi-Ag-Cu-(Hg) chemistry of galena and some associated sulfosalts: A review and some new data from Colorado California and Pennsylvania. *Canadian Mineralogist* **27**, 363-382.

Gamarra-Urrunaga, J.E. Castroviejo, R., & Bernhardt, H.J. (2013) Preliminary mineralogy and ore petrology of the intermediate-sulfidation Pallancata deposit, Ayacucho, Peru. *Canadian Mineralogist* **51**, 67-91.

Gagnevin, D. Menuge, J.F., Kronz, A., Barrie, C., & Boyce, A.J. (2014) Minor elements in layered sphalerite as a record of fluid origin, mixing, and crystallization in the Navan Zn-Pb ore deposit, Ireland. *Economic Geology* **109**, 1513-1528.

Genna, D. & Gaboury, D. (2015) Deciphering the hydrothermal evolution of a VMS system by LA-ICP-MS using trace elements in pyrite: An example from the Bracemac-McLeod deposits. *Economic Geology* **110**, 2087-2108.

Goodell, P.C. (1975) Binary and ternary sulphosalt assemblages in the Cu_2S-Ag_2S-PbS-Ag_2S_3-Sb_2S_3-Bi_2S_3. *Canadian Mineralogist* **13**, 27-42.

Gottesmann, W. & Kampe, A. (2007) Zn/Cd ratios in calcsilicate-hosted sphalerite ores at Tumurtijn-ovoo, *Mongolia. Chemie der Erde – Geochemistr*y **67**, 323-328.

Gottesmann, W., Gottesman, B., & Seifert, W. (2009) Sphalerite composition and ore genesis at the Tumurtjin-ovoo Fe-Mn-Zn skarn deposit, Mongolia. *Neues Jahrbuch für Mineralogie - Abhandlungen* **185**, 249-280.

Hall, S.R., & Czamanske, G.K. (1972) Mineralogy and trace element content of the Wood River lead-silver deposits, Blaine County, Idaho. *Economic Geology* **67**, 350-361.

Harris, D.C., & Owens, D.R. (1972) A stannite-kesterite exsolution from British Columbia. *Canadian Mineralogist* **11**, 531-534.

Hall, S.R., Szymański, J.T., & Stewart, J.M. (1978) Kesterite, Cu2(Zn,Fe)SnS4, and stannite, $Cu_2(Fe,Zn)SnS_4$, structurally similar but distinct minerals. *Canadian Mineralogist* **16**, 131-137.

Hall, H.T., 1996. The systems Ag-Sb-S, Ag-As-S and Ag-Bi-S: phase relations and mineralogical significance. Unpublished Ph.D. thesis, Brown University, 1-172.

Hoda, S.N., & Chang, L.L.Y. (1975) Phase relations in the systems PbS-Ag_2S-Sb_2S_3 and PbS-Ag_2S-Bi_2S_3. *American Mineralogist* **60**, 621-633.

Johan, Z., & Picot, P. (1982) La Pirquitasite, Ag_2ZnSnS_4, un nouveau membre du groupe de la stannite. *Bull. Minéral* **105**, 229-235.

Johan, Z. (1988) Indium and germanium in the structure of sphalerite: An example of coupled substitution with copper. *Mineral and Petrology* **39**, 211-229.

Kelly, W.C., & Turneaure, F.S. (1970) Mineralogy, paragenesis and geothermometry of the tin and tungsten deposits of the eastern Andes, Bolivia. *Economic Geology* **65**, 609-680.

Keighin, C.W., & Honea, R.M. (1969) The system Ag-Sb-S from 600 °C to 200 °C: *Mineralium Deposita* **4**, 153-171.

Large, R.R., Danyushevsky, L., Hollit, C., Maslennikov, V., Meffre, S., Gilbert, S., Bull, S., Scott, R., Emsbo, P., Thomas, H., Singh, B., & Foster, J. (2009) Gold and trace-element zonation in pyrite using a laser imaging technique: Implications for the timing of gold in orogenic and Carlin-style sediment-hosted deposits. *Economic Geology* **104,** 635-668.

Maydagán, L., Franchini, M., Lentz, D., Pons, J., & McFarlane, C., (2013) Sulfide composition and isotopic signature of the Altar Cu-Au deposit, Argentina: Constraints on the evolution of the porphyry-epithermal system. *The Canadian Mineralogist* **51**, 813-840.

Moncada, D., Mutchler, S., Nieto, A., Reynolds, T.J., Rimstidt, J.D., Bodnar, R.J. (2012) Mineral textures and fluid inclusion petrography of the epithermal Ag–Au deposits at Guanajuato, Mexico: Application to exploration. *Journal of Geochemical Exploration* **114**, 20-35.

Murakami, H., and Ishihara, S. (2013) Trace elements of Indium-bearing sphalerite from tin-polymetallic deposits in, China and Japan: a femtosecond LA-ICP-MS study. *Ore Geology Reviews* **53**, 223-243.

Paar, W.H., Miletich, R., Topa, D., Criddle, A.J., De Brodtkorb, M.K., Amthauer, G., & Tippelt, G. (2000) Suredaite, $PbSnS_3$, a new minerals species, from the Pirquitasite Ag-Sn deposit, NW-Argentina: mineralogy and crystal structure. *American Mineralogist* **85**, 1066-1075.

Paar, W.H., Brodtkorb, M.K., Sureda, R.J., Topa. D. (2001) Mineralogía, y quimismo de sulfuros y sulfosales de estaño y plomo en las vetas de Mina Pirquitas, Jujuy, Argentina (22°41'S66°28'W). *Revista geológica de Chile* **28**, 259-268.

Petruk, W. (1973) Tin sulphides from the deposit of Brunswick Tin Mines Limited. *Canadian Mineralogist* **12**, 46-54.

Pring, A., Tarantino, S.C., Tenailleau C., Etchmann B., Carpenter, M.A., Zhang, M., Liu, Y., & Withers, R.L. (2008) The crystal chemistry of Fe-bearing sphalerites: An infrared spectroscopy study. *American Mineralogist* **93**, 591-597.

Qian, Z. (1987) Trace elements in galena and sphalerite and their geochemical significance in distinguishing genetic types of Pb-Zn ore deposits. *Geochemistry* **6**, 177-190.

Ramdohr, P. (1955) Die erzmineralian und ihre verwachsungen. *Akademie-Verlag*, 1-875.

Ramdohr, P. (1969) The ore minerals and their intergrowths (3rd ed.) Pergamon Press, New York, United States of America, 1-1174.

Ramara, M., & Pattrick, R. (2011) Synthesis, characterization, stability and structure of solid solutions between α-miargyrite (AgSbS2) – smithite (AgAsS2) and β-miargyrite-smithite. *Journal Geopseria* **1**, 55-66.

Roland, G.W. (1968) The system Pb-As-S; composition and stability of jordanite. *Mineralium Deposita* **3**, 249-260.

Roland, G.W. (1970) Phase relations below 575 °C in the system Ag-As-S. *Economic Geology* **65**, 241-252.

Reich, M., Deditius, A., Chryssoulis, S., Li, J., Ma, C., Parada, A.P., Barra, F., & Mittermayer, F. (2013) Pyrite as a record of hydrothermal fluid evolution in a porphyry copper system: A SIMS/EMPA trace element study. *Geochimica et Cosmochimica Acta* **104**, 42-62.

Rosas, L.V., & Avila, J.C. (2013) Desarrollo minero de Pirquitas, provincia de Jujuy. *Serie Correlación Geológica* **29**, 51-62.

Sack, R.O. (2000) Internally consistent database for sulfides and sulfosalts in the system Ag_2S-Cu_2S-ZnS-FeS-Sb_2S_3-As_2S_3. *Geochimica et Cosmochimica Acta* **64**, 3803-3812.

Sack, R.O. (2005) Internally consistent database for sulfides and sulfosalts in the system Ag_2S-Cu_2S-ZnS-FeS-Sb_2S_3-As_2S_3: Update. *Geochimica et Cosmochimica Acta* **69**, 1157-1164.

Sack, R.O., & Ebel, D.S. (2006) Thermochemistry of sulfide mineral solutions. *Reviews in Mineralogy & Geochemistry* **61**, 265-364.

Sack, R.O., & Goodell, P.C. (2002) Retrograde reactions involving galena and Ag-sulfosalts in a zoned ore deposit, Julcani, Peru. *Mineralogical Magazine* **66**, 1043-1062.

Sack, R.O., Lynch, J.V., & Foit, Jr.,F. (2003) Fahlore as a petrogenetic indicator: Keno Hill Ag-Pb-Sn district, Yukon, Canada. *Mineralogical Magazine* **67**, 1023-1038.

Sack, R.O., & Lichtner, P.C. (2009) Constraining compositions of hydrothermal fluids in equilibrium with polymetallic ore-forming sulfide assemblages. *Economic Geology* **104**, 1249-1264.

Scott, S.D. (1983) Chemical behaviour of sphalerite and arsenopyrite in hydrothermal and metamorphic environments. *Mineralogical Magazine* **47**, 427-435.

Springer, G. (1972) The pseudobinary system Cu_2FeSnS_4-Cu_2ZnSnS_4 and its mineralogical significance. *Canadian Mineralogist* **11**, 535-541.

Shannon, R.D., 1976. Revised effective ionic radii and systematic studies of interatomic distances in halides and chalcogenedies. *Acta Crystallographica* **A32**, 571-767.

Sillitoe, R.H., Halls, C., & Grant, J.N. (1975) Porphyry tin deposits in Bolivia. *Economic Geology* **70**, 913-927.

Simon, G., Huang, H., Penner-Hahn, J.E., Kesler, S.E., & Kao, L. (1999) Oxidation state of gold and arsenic in gold-bearing arsenian pyrite. *American Mineralogist* **84**, 1071-1079.

Slater, E.T., Kontak, D.J., McDonald, A.M., (in prep.) The geology and origin of the Cortaderas Zone, Pirquitas Mine, NW Argentina.

Staude S., Dorn, A., Pfaff, K. & Markl, G. (2010) Assemblages of Ag-Bi sulfosalts and conditions of their formation: the type locality of schapbachite ($Ag_{0.4}Pb_{0.2}Bi_{0.4}S$) and

neighboring mines in the Schwarzwald ore district, southern Germany. *The Canadian Mineralogist* **48**, 441-466.

Toulmin III, P., Barton, P.B., & Wiggins Jr., L.B. (1991) Commentary on the sphalerite geobarometer. *American Mineralogist* **76**, 1038-1051.

Van Hook, H.J. (1960) The ternary system Ag_2S-Bi_2S_3-PbS. *Economic Geology* ***55***, 759–788.

Walia, D.S., & Chang, L.L.Y. (1973) Investigations in the system PbS-Sb_2S_3-As_2S_3 and PbS-Bi_2S_3-As_2S_3. *Canadian Mineralogist* **12**, 113-119.

Wernick, J.H. (1960) Constitution of the $AgSbS_2$-PbS, $AgBiS_2$-PbS, and $AgBiS_2$-$AgBiSe_2$ systems. *American Mineralogist* **45**, 591–598.